Electrochemical and Spectroelectrochemical Studies of 2,2´-Bipyridine Derivatives as Coordination Ligands with Transition Metals.

Salma Khamis Al-Musharafi

Ph.D Thesis

University of Edinburgh

2006

To My Mum, Dad, Brothers and Sisters.

Declaration

Except where specific reference is made to other sources, the work contained in this thesis is the original work of the author. It has not been submitted, in whole or in part, for any other degree.

Salma Al-Musharafy

Acknowledgements

First of all, I would like to thank my supervisor, Prof. Lesley J. Yellowlees, for her advice, encouragement, enthusiasm, patience and support throughout my studies. She is also due huge thanks for the help she gave with my writing up and for giving me the opportunity to pursue my PhD.

I'm grateful to Dr. Jack for her help in the first few months of my first year.

Dr. McInnes my many thanks for providing me with the simulation of the frozen spectra. I owe Dr. Murray thanks for his kind help in the lab especially with purifying and providing dry solvents, for his understanding, for being very welcoming especially when I first arrived and for being such an excellent teacher. He was also very helpful in the final stages of my thesis. I'm also grateful to Dr. Geary not only for taking part in the correction team, but for her encouragement and for the friendly spirit she always surrounded me with. Lucy Moorcraft for kind help correcting the English in the first two chapters of my thesis. My thanks go to Ed. Nind for all the nice conversations which helped me gain new and complicated vocabulary.

I wish to acknowledge Dr.Jose Hernandez, Dr. Emiliano Savalgni and Dr. Hatem Halouani for their patient answering of synthetic questions and for giving me lots of suggestions. Thanks go to those in the inorganic corridor (Laurent, Meki, Iria, Dr.Raffa, Pilar, Alex, Daniela, etc) for nice lunch breaks in K.B.House and for exchanging lots of cultural experiences. And to all the groups in lab N2.6 for a nice working atmosphere.

The work carried out in this thesis was supported by a grant from the government of the Sultanate of Oman and thanks must go to the Ministry of Higher Education for their support. Last but not least, I would like to thank my family and my friends for brightening my days and for always believing in me.

complex [Pt(5,5′–Ph_2–bpy)Cl_2] undergoes two reversible one electron reductions and the Pt(II) atom was found to force the ligand to be planar, thus the unpaired electron is delocalised over the bpy and the LUMO is ligand based. 5,5′–Br_2–bpy revealed one irreversible reduction. In contrast, [Pt(5,5′–Br_2–bpy)Cl_2] showed one reversible reduction. *In situ* UV/Vis/nir and EPR spectroelectrochemical results, in line with related complexes such as [Pt$(Me)_2$–bpy)Cl_2], showed that the contribution of the Pt to the SOMO is in the range 8–13 % and confirm that the added electron enters a ligand based orbital.

In their mono-reduced forms 4–NO_2–4′–Cl–bpy, 4,4′–$(NO_2)_2$–bpy and 4,4′–$(NO_2)_2$–6,6′–Cl_2–bpy, the unpaired electron is localised on the substituted py moiety. A triplet spectrum was observed in the EPR spectrum of a frozen solution of the di–reduced species of 4,4′–$(NO_2)_2$–bpy. In [Pt(4–NO_2–4′–Cl–bpy)Cl_2] the contribution of the ^{195}Pt to the SOMO orbital is *ca.* 3 %. This indicates that the reduction electron is ligand based, that is, the unpaired electron is localised on the ligand part of the complex.

The nature of the solvent was found to have no effect on the electrochemical and spectroelectrochemical results obtained from 5,5′–$(CO_2R)_2$–bpy (where R is Et or Me). This is may due to the electron being localised over the whole bpy pro–ligand, hence there will only be a minimal solvent effect. However, a solvent dependence was observed for the redox potential of 4,4′–$(NO_2)_2$–bpy and 4–NO_2–4′–Cl–bpy. The potential is shifted in the positive direction with increasing solvent acceptor number. This was

attributed to solvation which leads to stabilisation of the charged regions of the mono– and di–reduced species by acidic solvents.

Contents

List of Figures

List of Tables

Abbreviations

A	hyperfine coupling between an unpaired electron and a nucleus.
a	superhyperfine coupling between an unpaired electron and the ligand nucleus.
B	magnetic field
bpy	2,2,'–bipyridine
CE	counter electrode
CV	cyclic voltammogram
DCM	dichloromethane
DMF	dimethylformamide
DMSO	dimethylsulfoxide
E	potential
$E_{½}$	half–wave potential
e^-	an electron
E_{pa}	potential peak for an oxidation process
E_{pc}	potential peak for an reduction process
EPR	Electron Paramagnetic Resonance
g	EPR proportionality factor
G	Gauss
HOMO	highest occupied molecular orbital
i	current
i_p	peak current

IR	infra red
LUMO	lowest unoccupied molecular orbital
MLCT	metal–to–ligand charge transfer
py	pyridine
Q	charge
R	resistance
R.E.	reference electrode
T	time
[TBA]Cl	tetrabutylammonium chloride
[TBA][BF_4]	tetrabutylammonium tetrafluoroborate
THF	tetrahydrofuran
UV	ultraviolet
V	potential, Volts.
Vis	visible
W.E.	working electrode

1. Introduction

1.1. 2,2′–Bipyridine.

Pyridine has perhaps the greatest importance of all the known heterocyclic systems whether judged by the variety and interest in its derivatives and their reactions or simply by the volume of literature devoted to them. The chemical properties of the pyridine system can be grouped into three categories:

1) Properties that roughly parallel those of the benzene system, modified in some degree by the presence of the ring nitrogen. These include the typical electrophilic substitution reactions such as sulfonation and halogenation.

2) Properties unusual for the benzene system. In this group are the various reactions in which the key step involves interaction of the pyridine ring system with a base or nucleophilic reagent.

3) Properties associated with the unshared electron pair on the ring nitrogen. [1]

2,2′–Bipyridine which has two pyridine rings joined together, was first synthesized more than 110 years ago by Firtz Blau,[2] who simply dry–distilled the copper salt of picolinic acid. Since then, the preparation of this bidentate ligand has been improved dramatically using different synthetic strategies. In the area of analytical chemistry, bipyridines have been used as building blocks in supramolecular and macromolecular chemistry as well as

in nanoscience. 2,2′–Bipyridines can also be found in natural products like caerulomycins or collismycins.[2] 2,2′–Bipyridine is known as an iron reagent and is used as an inhibitor in non–toxic concentrations. The un–substituted molecule 2,2′–bipyridine (bpy) was developed as an analytical reagent for iron many years ago.[3] Since that time a large number of complexes has been prepared which contain bpy as a ligand bound to a variety of transition metals in different formal oxidation states.[4]

Studies on the X–ray crystal structure of bpy indicate that the two pyridine rings are coplanar. However, the radical anion of 2,2′–bpy may display various possible forms characterized by the torsion angle θ between the two constitutive moieties. The extreme conformers are the *cis* and *trans* where $\theta = 0°$ and $\theta = 180°$ respectively.

Previous studies[5-7] showed that the *trans* arrangement is significantly more stable than the *cis*. The *trans* arrangement of $(bpy)^{1-}$ is stabilized by the conjugative effect (π- electron delocalization between the two pyridyl rings) and also by the electrostatic effect (attractive N...H interactions between the *ortho* hydrogen of one ring and the nitrogen of the other ring). At equilibrium in solution and as a crystal, bipyridine adopts the *trans* arrangement, however, on coordination to a transition metal, its conformation becomes the *cis* arrangement as shown in Figure 1.1.

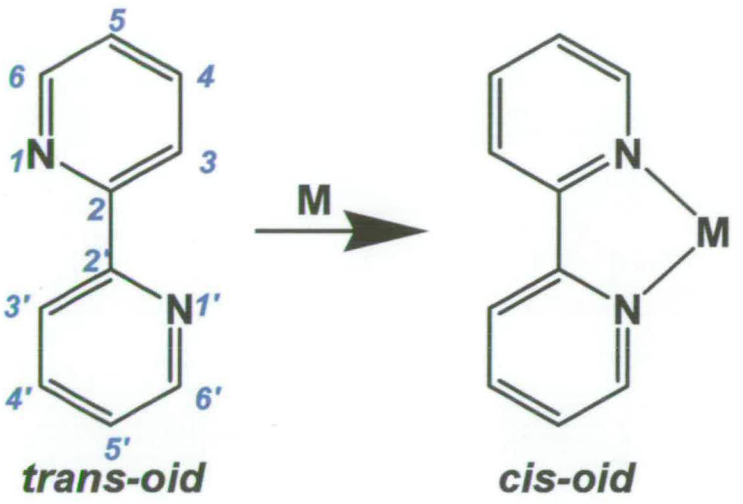

Figure 1.1 ***Cis/Trans*** **configurations and numbering system of bpy.**

Conformational studies were performed on 2,2′–bipyridinium salts by Campa *et al.*, [8] who found that non H–bridged 2,2′–bipyridinium ions can attain an orthogonal conformation and show a twist angle of θ = 90 ° (Figure 1.2).[10] Similar results were obtained by K. Szabo *et al.* [9] for calculations of protonated 2,2′–bipyridine.

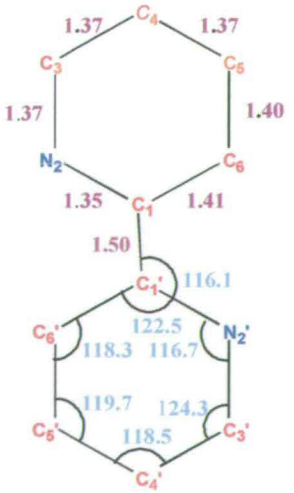

Figure 1.2 The experimental bond lengths (in Å) and bond angles (in °) for bpy

2,2′–Bipyridine (bpy) and its derivatives are renowned for their ability to form co–ordination complexes with metal ions from almost all groups in the Periodic Table.[11] Bpy is a bidentate, chelating ligand that co–ordinates to metal ions by making the M^{n+} part of a stable, five–membered ring. Furthermore, ligated bpy has the interesting ability to stabilise both very high and very low formal oxidation states of the central metal where it acts as a π-donor and π-acceptor, respectively (Figure 1.3).[12]

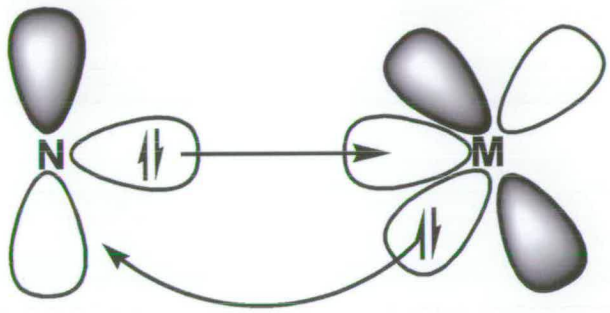

Figure 1.3 σ and π-back bonding between nitrogen atom on bpy and a metal centre.

The lone pair of electrons on the nitrogen can form a σ–bond by donating an electron into an unoccupied σ–orbital of the metal ion. Occupied orbitals of the metal having appropriate symmetry, (*i.e.* d–orbitals) can overlap with the unoccupied orbitals of the delocalised bpy π^* system. These two types of bonding reinforce each other; as the σ–donor bonding increases the electron density on the metal ion, its ability to form a π–bond with the bpy is enhanced, and back bonding occurs.

1.2. *Crystal field theory.*

1.2.1. Ligand effect in transition metal complexes.

Various definitions of the ligand effect have been given by people such as Golvin et al. [13] and most recently by Bursten.[14] The study of this effect has attracted attention from an early stage of coordination chemistry.[15] One area of interest is the influence of ligands in octahedral complexes. Tsuchida arranged the ligands in a series, which has become known as the spectrochemical series: $I^- < Br^- < S^{2-} < \underline{S}CN^- < Cl^- < NO_3^- < F^- < OH^- < C_2O_4^{2-} < H_2O < \underline{N}CS^- < CH_3CN < NH_3 < en < bpy < phen < NO_2^- < PPh_3 < \underline{C}N^- < \underline{C}O$. where the ligands are arranged in order of the increasing energy of the d–d transitions in a complex.[16] The series was found to be quite general and the same order of ligands was followed regardless of the metal centre. The effect of π–bonding correlates with the position of a ligand in the spectrochemical series, with π–donor ligands lying low in the series and π–acceptor ligands lying high in the series.[17]

Studies of ligand effect have led to the development of crystal field theory,[18–20] ligand field theory and molecular orbital theory. [21–24]

1.2.2. Square–planar complexes.

The five d–orbitals of transition metal atoms play a critical role in the formation of transition metal complexes. The five d–orbitals all have the same energy in the absence of a ligand field and are thus said to be degenerate. This thesis is primarily concerned with square–planar complexes. The square planar geometry is common for Pt(II) and

Pd(II), and is best explained by discussing six–coordinate complexes with distorted geometries. A tetragonal distortion of octahedral geometry is one where the M–L bonds along the z axis are extended and those along the x and y axes are compressed. This reduces the energy of the d_z^2 orbital, but increases the energy of the d_{x2-y2} orbital, see Figure 1.4. Therefore, if one, two, or three electrons occupy the e_g orbitals then a tetragonal distortion may be energetically advantageous.

The distortion of d^8 $(t_{2g})^6$ $(e_g)^2$ complexes may be large enough to encourage the two e_g electrons to pair in the d_z^2 orbital. In a square planar geometry, all the electrons are paired because the full advantage of filling the d_z^2 orbital must be exploited to compensate for the loss of two ligands, in the case of the tetragonal distortion.

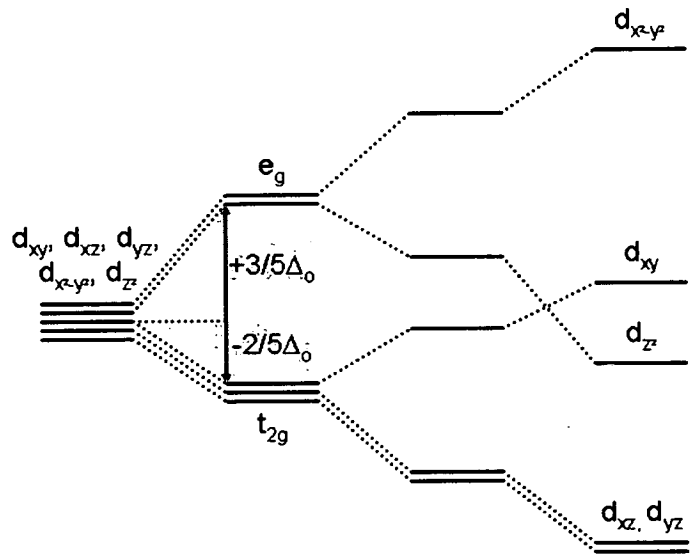

Figure 1.4 The splitting of d orbitals in fields of different geometries and the resulting electronic configuration of the d^8 Pt(II) ion.

1.3. Charge transfer transitions.

1.3.1. The ground state and excited states.

Electrons can move from the ground state energy level of a molecule to a higher level, if sufficient energy is supplied. In a photochemical process this energy is in the form of light E = hν, where is ν = frequency of the light (ν = velocity of light C divided by the wavelength λ) and h is Planck's constant.

1.3.2. Metal–to–Ligand charge transfer (MLCT).

Metal–to–ligand charge transfer spectra in transition metal complexes are ascribed to electronic excitations from an occupied molecular orbital, mainly of nd character, to an empty ligand–based acceptor orbital, usually of π symmetry. Metal–to–ligand charge transfer transitions can occur when there are empty ligand orbitals and the metal ion has filled orbitals lying higher than the highest filled ligand orbitals, *e.g.* complexes containing aromatic amines (pyridine, bipyridine, etc).[26] MLCT spectra in planar complexes have been characterized in great detail for the cyano complexes $[Ni(CN)_4]^{2-}$ and $[Pt(CN)_4]^{2-}$.[26] It is known that in the case of square planar Pt(II) complexes the MLCT band is observed at a higher energy than the corresponding bands in octahedral Pt(IV) complexes.[27]

Nowadays, information from many different experiments has been used to evaluate the valence electronic energy of metal complexes. For example, the correlation between optical and electrochemical properties of 2,2′–bipyridine complexes of ruthenium(II) has

been examined in order to estimate the energy of metal–to–ligand charge transfer absorption and emission processes.[28]

1.4. [Pt(bpy)Cl$_2$].

This thesis deals with Pt(II) complexes. An overview of the nature of [Pt(bpy)Cl_2] and its electronic spectra is discussed below.

There has been a great deal of interest in the recent chemical literature about the chemical and physical properties of related square–planar Pt(II) complexes, in which two labile ligands occupy *cis* positions in the coordination environment of the metal atom.
In particular, the title complex has been reported to exist in several different forms. Morgan and Burstal[29] reported two modifications of [Pt(bpy)Cl_2], both of which are described as light yellow. However, conversion of the yellow form to a red form is obtained by treatment of the former with concentrated HCl.

A detailed spectroscopic study of both the yellow and red forms was reported by Bielli *et al.*[30] who first suggested that the difference between the two forms was the stacking arrangement of the metal atoms in the red form, contrasted with the monomeric structure of the yellow form.

The coordination geometry of the platinum is approximately square planar (Figure 1.5).[30]

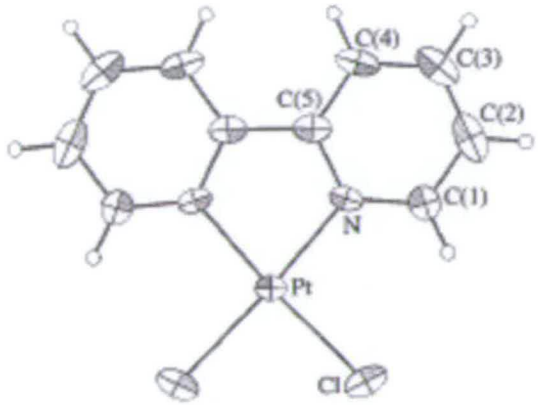

Figure 1.5 Square planar geometry of Pt(II) in [Pt(bpy)Cl_2].

1.4.1. Electronic spectra of [Pt(bpy)Cl_2].

Electrochemical and spectroelectrochemical techniques have been used by McInnes to characterise the electronic character of [Pt(bpy)Cl_2].[31,32,33] The spectroelectrochemical techniques will be explained in more detail in Chapter 2.

1.4.2. Electrochemistry of [Pt(bpy)Cl_2].

Several electrochemical studies on [Pt(bpy)Cl_2] have been done to gain more information about the electronic structure of the Pt(II) bpy complexes. Cyclic voltammetric studies on [Pt(bpy)Cl_2] show a fully reversible, one–electron reduction at –1.06 V (0.07) vs.Ag/AgCl (where the figure in brackets is the cathodic peak potential minus the anodic peak potential) followed by a second reduction at –1.79 V (0.110), the separation of ~ 700 mV between the two reductions has been reported to be a result of spin pairing of the two added electrons in the same molecular orbital.[31,32]

1.4.2.1. UV/Vis/nir Spectroelectrochemistry of [Pt(bpy)Cl_2].

In 1983, Kumar *et al.* [33] studied six mixed–ligand complexes of the formula [Pt(bpy)LL], where bpy is 2,2'–bipyridine and LL is the dianion of phthalic acid, salicylic acid, thiosalicylic acid, catechol, 4–tert–butylcatechol or 3,4–dimercaptotoluene. In their study, the electronic absorption spectra of [Pt(bpy)Cl_2] was reported. The UV/Vis spectrum of [Pt(bpy)Cl_2] in dimethylformamide (DMF) shows several bands. The position of these bands and their extinction coefficients (in brackets) are given in Table 1.1.[33]

Absorption band maxima (ε_{max}) in $1x10^3 cm^{-1}$

	Band 1	Band 2	Band 3	Band 4
[Pt(bpy)Cl_2]	25.38 (0.26[a])	30.49 (0.98)	31.60 (0.88)	35.34 (1.66)

Table 1.1 The electronic absorption spectra of [Pt(bpy)Cl_2] in DMF.

(a) Extinction coefficients in L mol $^{-1}$ cm^{-1} x 10^{-4} are given in parentheses.

L. Kumar *et al.* [33] attribute the first band in Table 1.1 to the charge transfer transition from a platinum d–orbital to the π^*–antibonding orbital of 2,2′–bipyridine. Band 3 was assigned to a charge–transfer transition from the same platinum orbital to a higher π^*–antibonding orbital of 2,2′–bipyridine. Bands 2 and 4 were assigned to the first and second internal $\pi \rightarrow \pi^*$ transitions of 2,2′–bipyridine.[33]

The absorption spectrum of $[Pt(bpy)Cl_2]^{1-}$ was studied by McInnes and co–workers,[32] which shows four bands at 11.2, 20.1, 21.6 and 27.9 kcm^{-1}. The UV/Vis/nir spectrum of Na^+ bpy^{1-} has four bands at 12.0 kcm^{-1}, 17.8 kcm^{-1}, 18.8 kcm^{-1} and 25.9 kcm^{-1}. Therefore, McInnes *et al.*[31] assigned the above bands in $[Pt(bpy)Cl_2]^{1-}$ to intraligand transitions of the co–ordinated bpy^{1-}. This suggests that the LUMO of $[Pt(bpy)Cl_2]$ is based on the bpy ligand and the first reduction product is best formulated as $[Pt(II)(bpy^{1-})Cl_2]^{1-}$.

1.4.2.2. EPR Spectroscopy of $[Pt(bpy)Cl_2]^{1-}$.

The solution EPR spectra of electrogenerated or chemically reduced $[Pt(bpy)Cl_2]^{1-}$ in DMF at room temperature show a broad single resonance with ^{195}Pt satellites, (^{195}Pt, 34 % natural abundance, I = ½). The solution spectrum observed indicates that the unpaired electron is coupling to the Pt nucleus, with any coupling to ligand nuclei unresolved. McInnes and co–workers attributed the small shift in g_{iso} from the free electron value, g_e = 2.0023, as a sign that there is only a small admixture of metal orbitals in the SOMO (Semi Occupied Molecular Orbital) and that the reduction electron must therefore be localised mainly on the bpy ligand in line with the results of UV/Vis/nir spectroelectrochemistry.[31,32] This suggests that the magnitude of the coupling of the unpaired electron to any ligand nuclei must be much smaller than coupling to the Pt centre. The solution EPR spectrum of $[Pt(bpy)Cl_2]^{1-}$ can be simulated with A_{iso} = –54 G and g_{iso} = 1.998, as shown in Table 1.2.[32]

On freezing the solution to 77 K the X–band EPR spectrum shows a rhombic splitting pattern with ^{195}Pt couplings to the low field, g_1 and g_2 components but no resolution of the ^{195}Pt coupling in the high field (g_3) component. A_3 is therefore estimated from the values of A_{iso}, A_1 and A_2.

	g_{iso}[a]	g_1[b]	g_2	g_3	A_{iso} (Pt)[c]	A_1[c]	A_2[c]	A_3[c, d]
$[Pt(bpy)Cl_2]^{1-}$	1.998	2.038	2.009	1.935	-54	-56	-95	-11

Table 1.2 EPR parameters for $[Pt(bpy)Cl_2]^{1-}$ from Collison et al.

(a) Isotropic data from chemically generated species in DMF. (b) Anisotropic data from the electrochemically generated species, 0.1 M [TBA][BF_4]/DMF, spectrum recorded at 77 K. (c) A/10^{-4} cm^{-1}. (d) estimated value from A_{iso}, A_1 and A_2.

EHMO calculations indicate that the only metal orbitals of the correct symmetry and energy to mix with π orbitals of bpy in the SOMO of $[Pt(bpy)Cl_2]^{1-}$ are the $6p_z$ and $5d_{yz}$ orbitals. The contribution of the Pt orbitals to the SOMO of $[Pt(bpy)Cl_2]^{1-}$ was calculated using Maki's Equations[34] with Rieger's nomenclature[35] (Equations 1.1 – 1.3) in C_{2v} symmetry, where the x and y axes are given in Figure 1.6.[32]

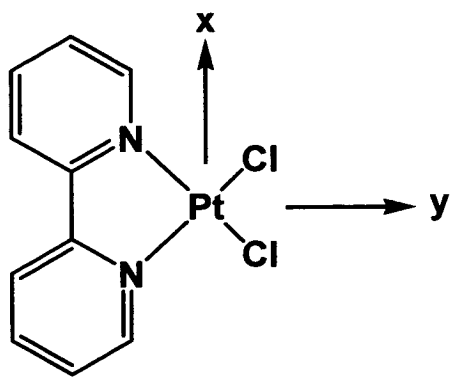

Figure 1.6 Principal axis of $[Pt(bpy)Cl_2]$.

$$A_{xx} = A_s - 4/7P_d a^2 - 2/5P_p b^2 \qquad \textbf{Equation 1.1}$$

$$A_{yy} = A_s + 2/7P_d a^2 - 2/5P_p b^2 \qquad \textbf{Equation 1.2}$$

$$A_{zz} = A_s + 2/7P_d a^2 + 4/5P_p b^2 \qquad \textbf{Equation 1.3}$$

In these equations a and b are the linear combination of atomic orbital coefficients of the $5d_{yz}$ and $6p_z$ orbitals in the SOMO, respectively, A_s is the isotropic Fermi contact interaction term, A_{xx}, A_{yy} and A_{zz} are the non–isotropic coupling constants along the respective x, y and z axes (cm^{-1}) and P_d and P_p are the electron–nuclear dipolar coupling parameters for the Pt 5d or 6p orbitals (cm^{-1}). Although the EPR spectra are dominated by the metal splitting, the results obtained using Equations 1.1 – 1.3 showed that the SOMO contained only 5 % from $5d_{yz}$ and 7.6 % from $6p_z$ orbitals and the remainder of the SOMO must be made up of a huge contribution (> 88 %), from the bpy ligand. Therefore, the SOMO of $[Pt(bpy)Cl_2]^{1-}$ is primarily bpy π^* based.[36,37]

In conclusion the one–electron reduction product of $[Pt(bpy)Cl_2]^{1-}$ can be formulated as $[Pt(II)(bpy^{1-})Cl_2]^{1-}$.

1.5. 4,4′–(X)$_2$–bpy and 5,5′–(X)$_2$–bpy.

DFT calculations on the lowest unoccupied molecular orbital of 2,2′–bipyridine show a significantly greater electron density at the 5,5′ position than at the 4,4′ position.[37] Thus, substitution of the 5,5′ position could be expected to have a greater effect on the electronic character of the species than substitution at the 4,4′ position.[38] While there have been many reports on the synthesis of 4,4′– and 6,6′–disubstituted bipyridyl

pro–ligands there are only a few examples of 5,5′–disubstituted bpys. This may be due to the difficulty in synthesising such ligands, as the β positions of 2,2′–bpy are unreactive to nucleophilic attack. Nitration of these positions has been reported as unsuccessful.[39]

Previous research found a correlation between the redox properties of disubstituted bipyridine with σ, the Hammett Parameter of the substituent X. σ can be viewed as the measure of the electron withdrawing (positive σ values) or electron donating (negative σ values) power of X. A linear plot between the Hammett Parameter σ_m / σ_p and the first reduction potential for both 4,4′ and 5,5′ substituted bpy has been demonstrated.[40] Such a correlation has been taken to indicate that the frontier orbitals of the substituted bpy ligands have similar electronic characters. Moreover, this correlation indicate that the 5,5′ position on the bpy molecule is electronically the more important site of substitution.

1.6. [Pt(4,4′–(X)$_2$–bpy)Cl$_2$] and [Pt(5,5′–(X)$_2$–bpy)Cl$_2$].

The Pt complexes of different substituted bpy ligands have been synthesised by heating to reflux an aqueous solution of the ligand and K_2PtCl_4.[31] The synthesis of [Pt(5,5′–(X)$_2$–bpy)Cl$_2$] (X = Me, CO_2Et, NH_2 or CO_2Me) was undertaken and comparisons were drawn with previously studied complexes.[38] These substituents are of particular interest as they have a wide range of electron withdrawing and donating abilities.[31] The electrochemical studies of these complexes give similar results to those of the corresponding free ligands. $E_{½}$ values of the ligand reduction were shifted to more positive potentials on complexation.[31] This indicates that the electron enters the lowest unoccupied π^* orbital of the X_2–bpy ligand. All reductions were reversible except for X=

NH_2, where the first reduction was followed by a rapid chemical reaction. The plots of the Hammett Parameter σ_m / σ_p and the first reduction potential of the Pt(II) complex for both 4,4′ and 5,5′ substitutions are linear, see Figure 1.7.[38] It is clear that the [Pt(5,5′–X_2–bpy)Cl_2] line is steeper than the line for the 4,4′ position. This implies that changing the substituents at the 5,5′ positions has a greater effect on the electrochemistry of the complex than at the 4,4′ position.[31] Hence we can conclude that the 5,5′ positions on the bipyridyl ligand is electronically more important than the 4,4′ position. This is in agreement with the conclusion reached by Baxter *et al.*[39] based on DFT calculations.

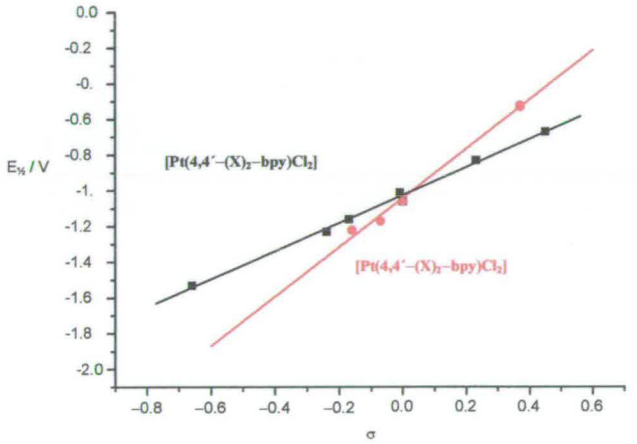

Figure 1.7 E½ of [Pt(4,4′–$(X)_2$–bpy)Cl_2] *vs.* Hammett parameter σ_p overlaid with the E½ of [Pt(5,5′–$(X)_2$–bpyCl_2] (X = H, Me, CO_2Et, NH_2 or CO_2Me) *vs.* Hammett parameter σ_m.

1.7. Aims of this thesis.

The aims of this thesis are to study several types of 5,5′ and 4,4′– (bpy) pro–ligands and their Pt(II) complexes. The study will involve electrochemistry and

spectroelectrochemistry techniques such as UV/Vis/nir spectroelectrochemistry and EPR spectroelectrochemistry. Comparison between the free ligand properties and their Pt(II) complexes will provide more understanding of the nature of the redox processes. The importance of the solvent on the reduction processes will also be investigated.

2. Experimental techniques.

2.1. Introduction.

During the course of this work a number of electrochemical and spectroelectrochemical techniques were used. This chapter explains each technique.

2.2. Electrochemical Techniques.

2.2.1. Background.

Electrochemistry is a powerful technique for studying redox–active species.[41] Briefly, the development of the three–electrode system and the cell used in this study will be described.

2.2.1.1. Three–Electrode System.

Electrochemical techniques are used for the study of redox active compounds. The simplest approach to the measurement of current/voltage characteristics involves the use of two electrodes. The first one is the working electrode (WE) where the electron transfer occurs. The second electrode is the reference electrode (RE) which has a known standard potential value. This means that the reference electrode provides a fixed potential, which does not vary during experiments. Consider a simple electrochemical reaction to be studied using a two–electrode system. If a potential is applied across the electrodes then it is distributed as shown in Equation 2.1.

$$E_T = E_1 + E_2 + IR \qquad \textbf{Equation 2.1}$$

Where:

E_T = The total potential (applied potential).

E_1, E_2 = The potential differences across each solution/electrode interface

I = The current

R= The resistance of the solution.

Voltammetry experiments measure I as a function of E and for reactions where only a small current is passed, IR is small and the two–electrodes system is acceptable.

However, for larger currents, the IR term is significant and, therefore, the potential at the working electrode will drop by an unknown amount. To circumvent this, a third electrode is used. This is called the counter electrode (CE) and is often made of Pt. In the work presented in this thesis, the three–electrode system has been used, see Figure 2.1. This consists of a working electrode, often made of platinum, a counter electrode which has a large surface area in order to pass an unlimited current and a reference electrode, usually Ag/AgCl in 0.45 M [TBA][BF_4] (tetrabutylammonium tetrafluoroborate) and 0.05 M [TBA]Cl in DCM (dichloromethane).

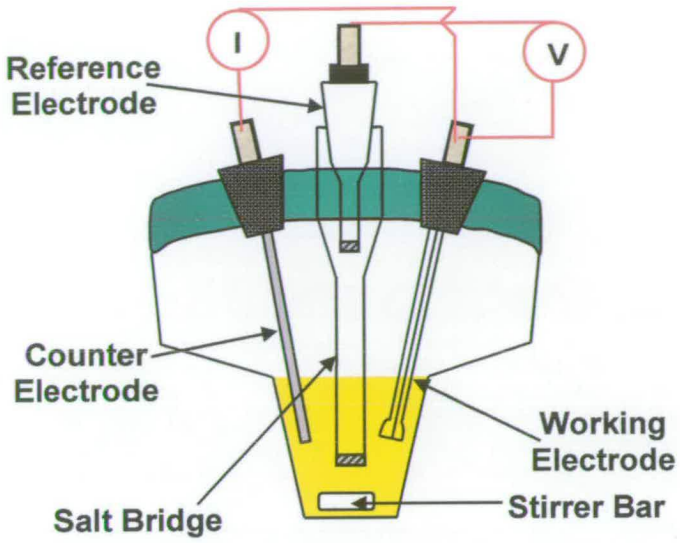

Figure 2.1 Schematic diagram of standard three-electrode cell used for cyclic voltammetry.

In order to prevent any contamination of the RE itself, or contamination of the species being studied by the RE, the RE is isolated from the test solution by a salt bridge. Potentials are corrected to the potential for the ferrocenium/ferrocene redox couple at +0.55 V, as ferrocene is used as the internal standard. The measured potentials are referred to the ferrocenium/ferrocene redox couple because ferrocene is reliable and very stable in different solvents. All redox potentials and peak to peak values are reported for a scan rate of 100 mV s^{-1}, unless otherwise stated. The peak to peak value is given in brackets after the redox potential. The three–electrode system is controlled by electronics to make sure that the current flows between the working electrode and the counter electrode, which means IR ~ 0 in the RE/WE part of the circuit.

The applied potential can now be attributed to the working and reference electrodes and since the reference electrode has a fixed value, the working electrode potential can be calculated.

2.2.1.2. Supporting electrolyte.

The resistance of the solution also needs to be considered. To minimize this an inert electrolyte known as the supporting electrolyte is added to the solvent. This electrolyte increases the conductivity of the solution and eliminates migration as a mode of mass transport for the electroactive species so that the electroactive species acts only under diffusion control. An ideal supporting electrolyte must satisfy all of these conditions:

It must be very soluble in the chosen solvent.

It must be electrochemically and chemically inert.

It must be easily prepared and purified.

Most of the electrochemical experiments in the course of the work described here used [TBA][BF_4] as the inert electrolyte.

All solutions were purged with N_2 before use to remove dissolved oxygen and a continuous stream of N_2 was passed over the top of the solution throughout electrochemical study. This is due to the fact that O_2 is easily reduced and its presence causes unwanted redox reactions:

$$O_2 + 2H_2O + 2e^- \rightarrow H_2O_2 + 2OH^- \qquad E_{½} = -0.1\ V.$$

$$H_2O_2 + 2e^- \rightarrow 2OH^- \qquad E_{½} = -1.2V.$$

Reduction of O_2 produces H_2O_2 which is capable of acting as a chemical oxidizing or reducing agent. Therefore, dissolved O_2 is removed from solution before electrochemical study.

The supporting electrolyte is used in different concentrations, depending on the solvent used. 0.1 M [TBA][BF_4] solution were used for DMF, acetonitrile, DMSO and acetone. A 0.2 M [TBA][BF_4] solution was used for pyridine and 0.3 M [TBA][BF_4] solutions were used for DCM, ethyl acetate and THF.

The choice of solvent depended on the solubility and the stability of the compound under investigation. For a solvent to be suitable for electrochemistry it should have a compatible potential range, a high dielectric constant, an accessible temperature range and a low viscosity. Ideally, it should also be easy to purify. If the solvent can act as a co–ordinating ligand, this should also be taken into account.

2.2.2. Cyclic voltammetry.

Cyclic voltammetry is a technique well–suited to initial electrochemical studies of new systems as it can be used to obtain information about fairly complicated electrode reactions. The technique uses stationary electrodes in a stagnant solution.[41]

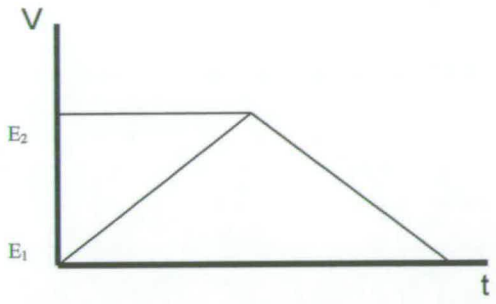

Figure 2.2 Change in potential with time during cyclic voltammetry.

$$A_{(eq)} + e^- \underset{K_{ox}}{\overset{K_{red}}{\rightleftharpoons}} B_{(eq)}$$

Equation 2.2

Linear–sweep voltammetry can be extended so that when the potential reaches the value E_2 the direction of sweep is reversed and the electrode potential is scanned back to the original value, E_1 (Figure 2.2). This gives a triangular potential cycle and the technique is termed cyclic voltammetry.[42]

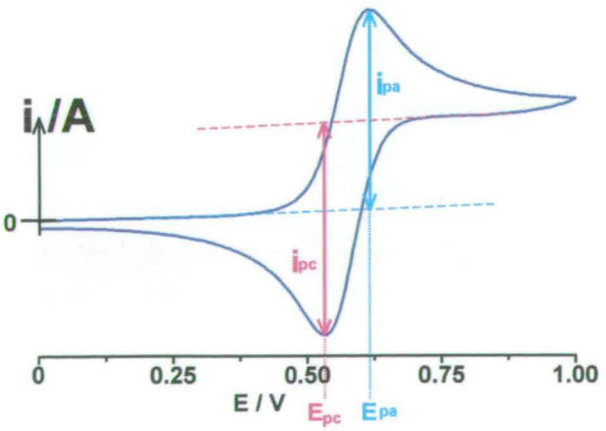

Figure 2.3 Normal cyclic voltammogram of a reversible oxidation process.

During a cyclic voltammetric experiment the current is measured while the potential of the working electrode is varied as described above.

Figure 2.3 shows the E versus i behaviour for a fully reversible redox process. Initially, there is no current flow since the potential is too low to induce an electron transfer. Then, as the potential approaches the $E_{½}$ value of the process, the current starts to increase. After all the compound around the working electrode has reacted, new compound can only reach the electrode by diffusion so the current reaches a maximum and then drops to the diffusion limited current. Then the potential is reversed and the opposite electron transfer occurs and a current of the opposite sign is observed. Gradually, all of B in Equation (2.2) present in the diffusion layer is reconverted to A and the current drops back to zero.

This is the case of reversible electrochemical process, where the maximum currents (i_p^{ox}, i_p^{red}) vary with the square root of the scan rate (ν_s). Therefore, the reversibility of a process can be established by ensuring that the plot of i_p *vs.* $\sqrt{v}$ is linear. However, in many cases the process is not reversible due to chemical decomposition of the product of electron transfer. In these cases the height of the return peak is smaller than the forward peak, $i_{pa} > i_{pc}$. To counteract this, the solution can be cooled and the scan rate increased to outrun the decomposition reaction.

2.2.2.1. Experimental setup.

The cyclic voltammetry setup used in this work involved a cell (container) to hold the solution under test. Three electrodes were inserted along with a nitrogen bubbler and a stirrer bar. The solutions were fully degassed using nitrogen before any experiments were performed.

All platinum electrodes were cleaned with concentrated nitric acid, washed with distilled water and dried before use.

Electrochemical studies were carried out using a Dell GX110 PC with General Purpose Electrochemical System (GPES) version 4.8 software, connected to an autolab system containing a PGSTAT 20 potentiostat.

2.2.3. Stirred voltammetry.

Using the same experimental set up as cyclic voltammetry, a stirred solution may be studied with a much slower scan rate, typically 20 mV s^{-1}.[41] Stirred voltammetry experiments, see Figure 2.4, determine which type of process is under study, a cathodic current flow indicates a reduction while an anodic current indicates an oxidation. Stirred voltammetry is mainly used in conjunction with coulometry to determine if the bulk electrolysis has been carried out to completion.

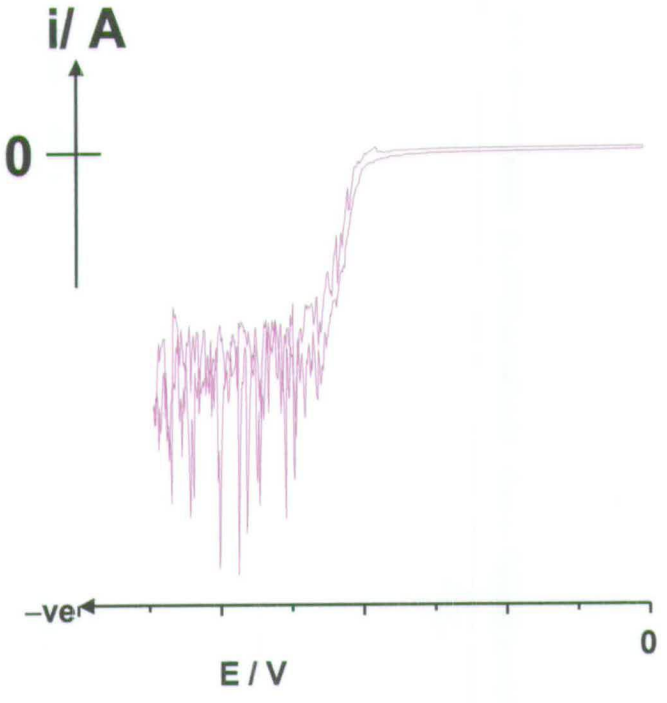

Figure 2.4 I vs. E response for a reductive stirred voltammetric experiment.

2.2.4. Differential pulse voltammetry (DPV).

In this technique the same three–electrode system is used to measure the changes in current with voltage.[41] The variation of potential with time used in DPV is illustrated in Figure 2.5.

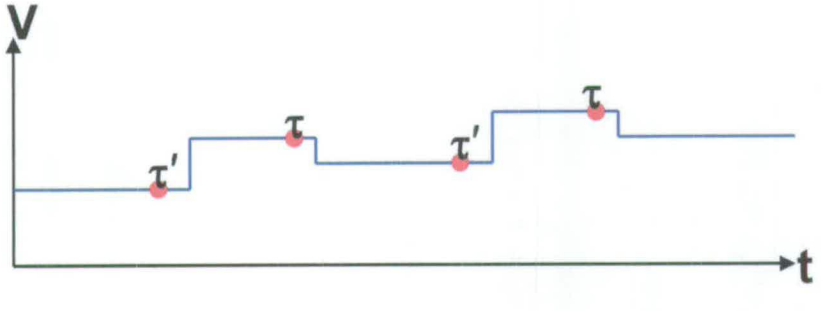

Figure 2.5 Waveform for differential pulse voltammetry.

The waveform is composed of a series of potential pulses. After each pulse the potential returns to a value which is slightly more negative (in a cathodic scan) or more positive (in an anodic scan) than the value preceding the pulse. The potential difference (ΔE_s) is the potential change that takes place after a full waveform cycle. The scan rate is given by the ratio between ΔE_s and the period of the cycle, τ.

The current is measured twice per pulse, before and after the pulse is applied. The current measuring points are indicated by $\tau'$and τ in Figure 2.5. The difference of these two current values is then plotted against the potential which gives a typical DPV as shown in Figure 2.6 .

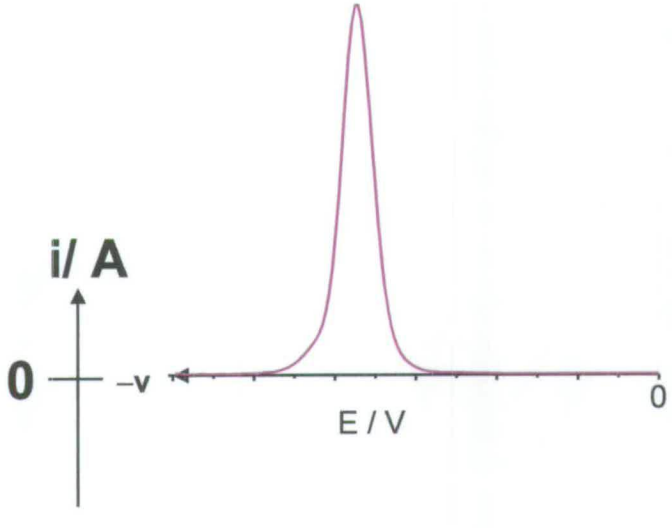

Figure 2.6 A typical differential pulse voltammogram.

As the data are presented as a differential measurement, this technique is very sensitive and is particularly useful for examining redox processes that occur in close proximity to each other. The same cell set–up is used (see Figure 2.1) as for cyclic voltammetry.

2.2.5. Coulometry.

The cell used in this technique is called an H–cell, see Figure 2.7. There are two types of working electrode shown in this Figure. The Pt basket working electrode is where the chosen potential is applied for bulk electrolysis. The Pt microdisc electrode is used for normal cyclic voltammetry. The counter electrode is separated from the working electrode by a sintered frit. This makes sure that electron transfer occurs, but stops any reaction occurring between the solution and the counter electrode products which may be produced during the electrolysis.[88]

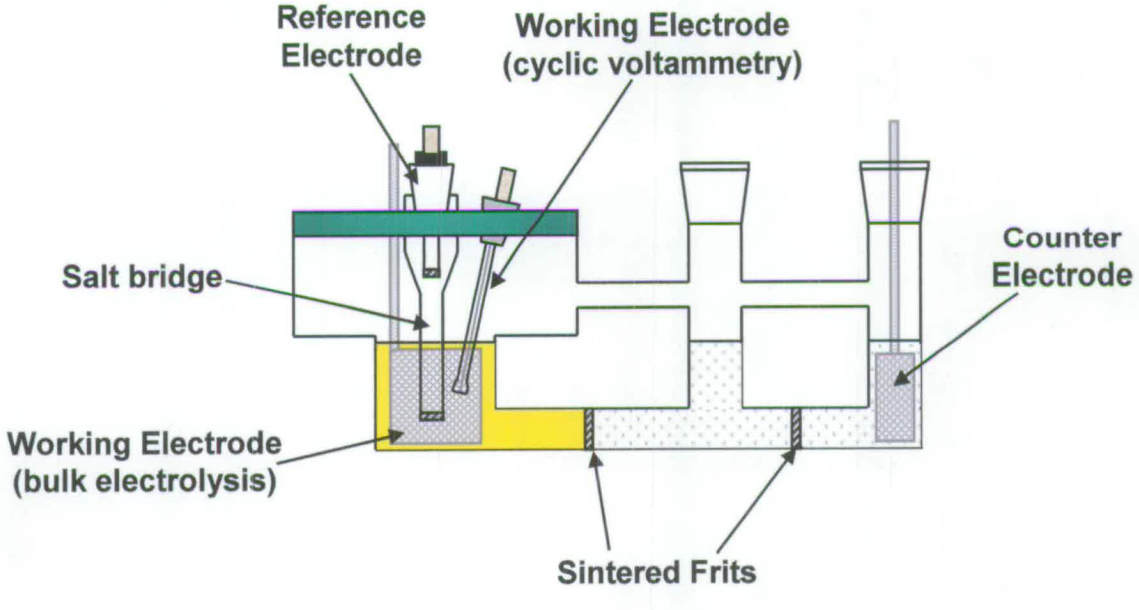

Figure 2.7 Schematic diagram of a standard of H-cell.

Coulometry provides information about the number of the electrons involved in the process by measuring the charge passed for a known concentration of the electroactive species solution using Equation 2.3.

$$Q = nFe \qquad \textbf{Equation 2.3}$$

Where is Q = total charge passed/C, n = number of moles of electroactive species, F = Faraday constant = (96485 $Cmol^{-1}$) and e = number of electrons transferred.

In this case the potential of the basket electrode is fixed and the charge passed is measured. Stirred voltammetry is used before and after passing the charge to make sure that the redox process is completed. The stirred voltammetric experiment requires a very slow scan rate (20 mV s^{-1}) and the platinum microdisc electrode. The solution is stirred continuously throughout the experiment.

For the electron transfer to be fully achieved at the WE, the potential applied must be at least 60 mV past the $E_{½}$ of the reduction (or the oxidation) process under study. The current flow is measured and its integral with respect to time, the charge Q, calculated. The complete solution of electroactive species must be reduced or oxidised.

2.2.5.1. Experimental set up.

In a typical coulometric experiment the H–cell is used, see Figure 2.7. Normal and stirred cyclic voltammetry is first applied using the microdisc working electrode, then the working electrode is exchanged for the Pt basket electrode while the solution is stirred and the number of electrons involved in the redox process is measured. To ensure stability of the electron transfer product species, the cell is held at low temperature (–40 °C) by using a slush bath (acetone/dry ice). The temperature was measured using a digital thermometer.

2.2.6. Chronoamperometry, e.g. Double Potential Step Technique.

An electron transfer process is often coupled to a chemical reaction which may succeed or precede the electrochemical reaction. These reaction systems are known as EC and CE processes respectively.[42]

Shwarz and Shain[42] proposed the chronoamperometry or the double potential step method for determining the rate of reaction for an EC process. The technique comprises two electrolysis steps at two appropriately controlled potentials. Double–step chronoamperometry was shown to have the least error in both rate constant and activation energy and could be employed over the largest temperature range.

Consider the reduction induced reaction,

$$O + ne^- \rightarrow R$$

$$R \xrightarrow{k} Y \qquad \textbf{Equation 2.4}$$

The waveform for a chronoamperometric experiment is illustrated in Figure 2.8.

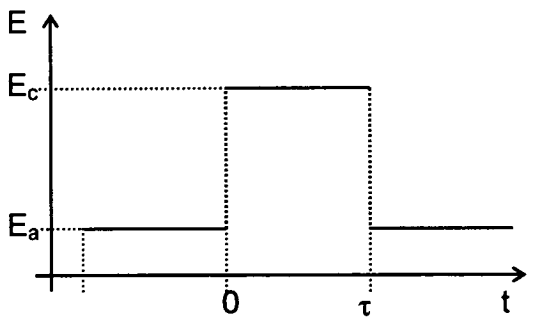

Figure 2.8 Change in potential with time during double-step chronoamperometry.

The potential is set at E_c where the species O is reduced (Equation 2.4) and the cathodic current–time is recorded. At some switching time τ, the potential is jumped to E_a at which the reduced species R is oxidised back to O and a second current–time curve is recorded. Both the electrode process and the chemical reaction consume R, which leads to a more rapidly decaying current–time response for the anodic response compared to the cathodic process. Thus, the ratio of the currents i_a/i_c is associated with the rate constant k. Typical cathodic and anodic current–time curves are shown in Figure 2.9.

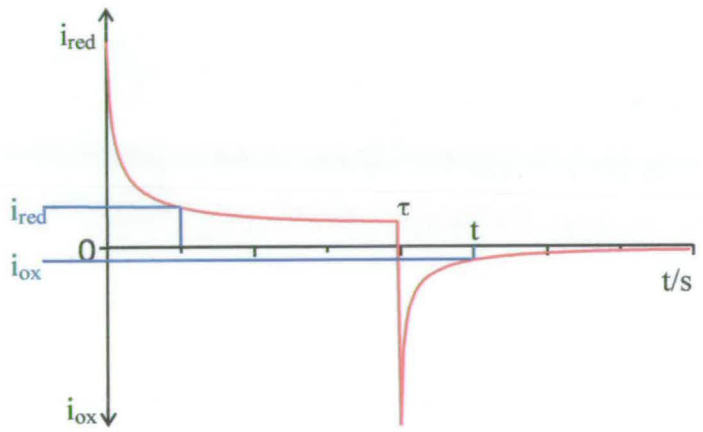

Figure 2.9 Reduction-oxidation current-time curve of a reduction induced electrochemical-chemical process for the double-step chronoamperomtry experiment.

The magnitude of the current is controlled by the amount of the species at the electrode and, therefore is dependent on the time, τ, and on the rate of the chemical reaction;

$$R \xrightarrow{k} Y$$

The rate constant (k) can be calculated from the differences in the current/time responses for the two steps.

From Equation 2.5, Schwarz and Shain[42] established a series of theoretical working curves for the first order reaction in which the current ratio i_a/i_c or i_{ox}/i_{red} is plotted against $k\tau$ for the time ratio $(t-\tau/t)$.

$$-\frac{i_{ox}}{i_{red}} = \phi[k\tau(t-\tau)/\tau] - \sqrt{\frac{(t-\tau)/\tau}{1+(t-\tau)/\tau}} \qquad \textbf{Equation 2.5}$$

where ϕ represents a mathematical function comprising the terms: electrode area, Faraday's constant, k, τ, t, bulk concentration, diffusion coefficients, and the number of electrons transferred. Measurement of such i/t curves and interpretation of the data using the working curves allows determination of $k\tau$ and hence k.

However, the selection of the switching time τ significantly affects the accuracy of the measurements. The value of τ has to be chosen carefully so that values of $-i_{ox}/i_{red}$ corresponded to the middle part of the working curves, thereby ensuring the greatest accuracy in the determination of k.

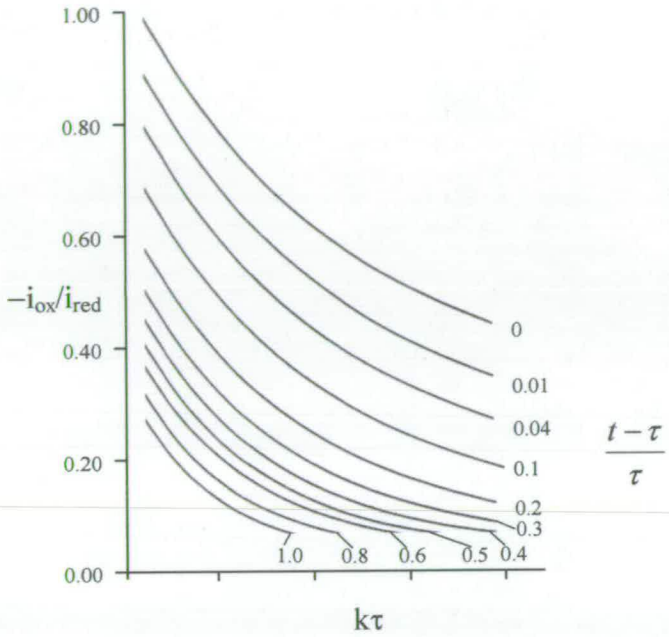

Figure 2.10 Theoretical working curves plotting $-i_{ox}/i_{red}$ against kτ devised by Schwarz and Shain.[42]

One very positive advantage of the double potential step technique is that the values of the current ratio are not sensitive to the internal resistance of the solution. It can also be shown that the rate constant is solved independently of electrode area, solution concentration, and diffusion coefficients.

The Arrhenius equation (Equation 2.6) is used to calculate the activation energy (E_A) of the chemical reaction.

$$k = Aexp^{(-Ea/RT)} \qquad \textbf{Equation 2.6}$$

A plot of ln k versus 1/T will give a slope with a gradient equal to $-E_A/R$ where R is the universal gas constant 8.3145 J mol^{-1} K^{-1}.

2.2.6.1. Experimental set up.

Double–step chronoamperometry experiments were carried out using the same hardware and software as the other electrochemistry techniques. A three–electrode system was also used although a platinum quasi–reference electrode was used instead of Ag/AgCl as it gives more consistent results. The jacketed cell maintained temperature control (Figure 2.11). It can be cooled with methanol down to 223 K or heated with silicon oil up to 498 K. The temperature was recorded using a digital thermometer.

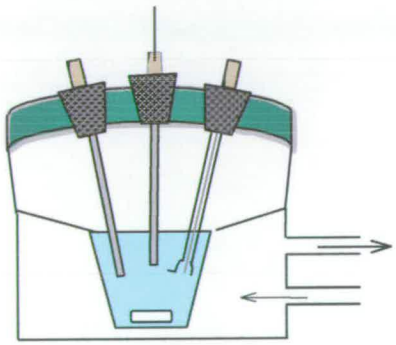

Figure 2.11 A jacketed cell used for temperature controlled double-step chronoamperometry experiments.

2.2.7. Spectroelectrochemical Techniques.

Spectroelectrochemical experiments are important and helpful tools in the characterisation of redox reaction products. Electrochemistry can be combined with electronic spectroscopy to monitor how the formation of a reduced or oxidised species can bring about changes in the transfer of electrons between valence shell molecular

orbitals. One of the main combined solution spectroelectrochemical techniques used is UV/Vis detection as it has a simple experimental set up and gives a great deal of information about the system under study.

One relatively under used spectroelectrochemical technique that has been utilised to great effect in this work is electron spin (or paramagnetic) resonance (EPR) spectroscopy.

2.2.7.1. UV/Vis spectroelectrochemical techniques (OTTLE).

Spectrochemical methods of analysis depend on the absorption of energy by atoms or molecules. Light can be considered to consist of energy packets, called photons, each with energy: $E = h\nu = h.c/\lambda$.

In a chemical species, the absorption of a photon depends on the difference between two energy levels. Therefore, when absorption occurs the electron is transferred from an occupied molecular orbital to a higher energy unoccupied molecular orbital. The lowest energy transition is usually between the highest occupied molecular orbital (HOMO) to the lowest unoccupied molecular orbital (LUMO), see Figure 2.12.

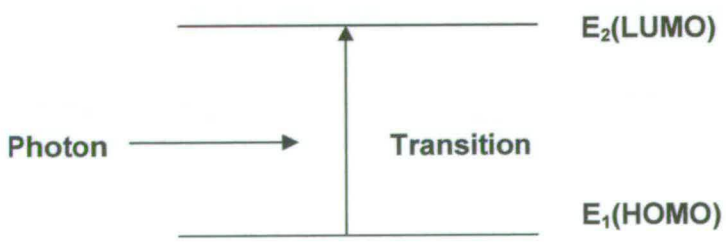

Figure 2.12 The scheme of an electronic transition.

OTTLE stands for Optically Transparent Thin Layer Electrode which describes the cell used in this technique. The UV/Vis spectroelectrochemical technique is a combination of electrochemistry, where the potential is held and simple UV/Vis/nir spectroscopy which gives details of the electron transformation. This method of analysis uses a different cell to those already described and is shown in Figure 2.13. It consists of a flat quartz cell of path length 0.05 cm, into which the Pt/Rh gauze working electrode fits and a quartz reservoir above the flat cell which contains the counter electrode, a Pt wire, and the reference electrode, usually Ag/AgCl. The counter electrode and reference electrode are separated from the working electrode by salt bridges containing a solution of $TBABF_4$/solvent (electro active solution).The transparency of the cell is approximately 40%. The quartz cell is placed into a gas tight PTFE block placed in the spectrometer. Pre–cooled N_2 is passed over the outside of the cell in order to study the redox process at low temperature. To prevent frosting of the flat cell, dry room temperature N_2 is passed between the inner and outer quartz windows of the PTFE block and the spectrometer cavity is kept under N_2. The temperature is monitored using a thermocouple connected to a digital thermometer.

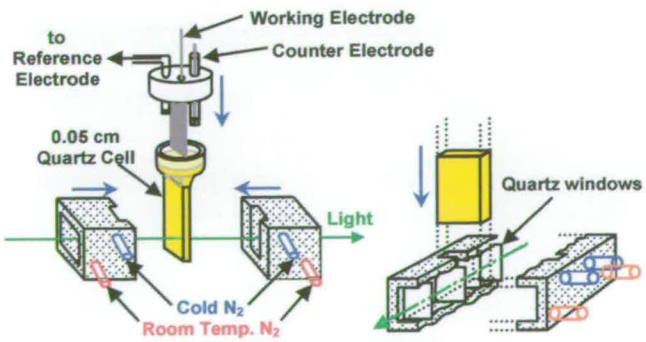

Figure 2.13 The OTTLE cell.

During a spectroelectrochemical experiment the potential of the gauze electrode is held beyond the redox potential and a current flows. The absorption spectrum changes as the starting material is converted to the electron transfer product, that is, the reduced/oxidised molecules. Complete electron transfer is achieved when the spectral changes stop. For the redox couple to be reversible, the spectrum should revert to that of the original sample when the potential is taken back to its starting value. The electrogeneration potential was usually set at 0 V to regenerate the starting material in order to ensure the chemical integrity of the system. Isosbestic points are a good evidence of a clean conversion.

A normal background UV/Vis spectrum was carried out in [TBA][BF_4]/solvent (electro active solution). After cleaning the cell, the solution of the compound under study was inserted in to the cell, (Figure 2.13) and degassed with N_2. The temperature was then adjusted and UV/Vis/nir spectra were recorded on a Perkin–Elmer spectrophotometer controlled by a data link PC running UV winlab software, version 2.70.01.

2.2.7.2. Electron Paramagnetic Resonance (EPR).

Electron Paramagnetic Resonance (EPR) spectroscopy is an extremely powerful probe of the electronic structures of materials with unpaired electrons.

With respect to d–transition metal ions, EPR spectroscopy is widely used to study coordination and organometallic complexes, and metal ion centres in biological materials and in catalysts.[44]

Electron paramagnetic resonance (EPR) can be viewed as the electronic analogue of nuclear magnetic resonance (NMR) and many of the principles of NMR apply to EPR.

An electron has a spin (s) of ½ and an associated magnetic moment. Consequently, in a magnetic field the two spin states, corresponding to the resolved spin, Ms = +1/2 and −1/2, have different energies. The difference in energy, ΔE, between the two states is given by Equation 2.7.

$$\Delta E = g\,\mu_B B \qquad \textbf{Equation 2.7}$$

Where:

μ_B, is the Bohr magnetion (9.274×10^{-24} JT^{-1})

B, is the magnetic field (in Tesla).

g, is a proportionality factor which is equal to 2.0023 for a free electron (g_e).

Transitions between the two spin states may be caused by absorption of energy in the microwave region of the electromagnetic spectrum. The resonance condition is usually put in the form shown in Equation 2.8:

$$h\nu = g\mu_B B \qquad \textbf{Equation 2.8}$$

If a sample is exposed to electromagnetic radiation of frequency (ν) a strong absorption or resonance occurs when the magnetic field satisfies the condition given in Equation 2.6. EPR spectra of transition metal complexes can be used to study electronic distributions. As the energy of ligand orbitals approaches that of the metal, the interaction between them increases. The orbital occupied by an unpaired electron becomes more ligand–like and the unpaired electron interacts less with the metal nucleus.

In practice, the most useful information is derived from the hyperfine and superhyperfine coupling of the unpaired electron to nuclei with non–zero nuclear spin. Since the EPR

time scale is small coupling to quadrupolar nuclei is also observed (*i.e.* to nuclei with I >1/2).

The EPR spectroelectrochemical cell is based on a high grade quartz flat cell, as shown in Figure 2.14. The Pt/Rh gauze working electrode sits in the flat portion of the cell as in the OTTLE experiments and again the connecting wire is covered in a Teflon tube to prevent bulk electrolysis of the solution in the reservoir. A Pt gauze counter electrode and an Ag/AgCl reference electrode complete the cell. The EPR cavity contains a specially designed quartz holder. A dewar containing liquid nitrogen and a heater is connected to the quartz sample holder by insulated tubing. A thermocouple inserted through the bottom of the quartz holder regulates the temperature. [45]

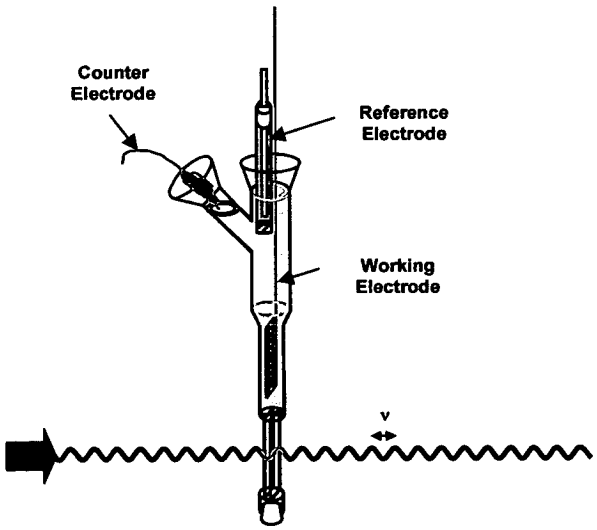

Figure 2.14 The *in situ*, variable temperature EPR cell

All spectra were recorded on an X–band Buker ER200D–SCR spectrometer, connected to a Datalink 486 DX PC running EPR Acquisition system, version 2.42 software. *In situ*

EPR spectra were electrogenerated using a BAS CV–27 voltammograph. Variable temperature work was carried out using a Bruker ER4III VT variable temperature unit.

2.3. Synthesis.

2.3.1. 5,5′–Diphenyl–2,2′–bipyridine.

2.3.1.1. 5,5′–Dibromo–2,2′–bipyridine

2,5–Dibromopyridine (8.00 g, 0.0338 mol), hexamethylditin (5.53 g, 0.0169 mol) and $[Pd(PPh_3)_4]$ (0.80 g) were heated to reflux in benzene (250 cm^3) for 65 h under argon. The reaction mixture was cooled and ether (200 cm^3) added. An off–white precipitate was filtered off and chromatographed on silica gel. Eluting with $CHCl_3$–CH_3OH (99.9:0.1) gave 5,5′–dibromo–2,2′–bipyridine as a white solid, yield 80%, mp 225.5–226.5 C.[45]

CHN analysis of $C_{10}H_6N_2Br_2$, Calculated: C 38.22%, H 1.91%, N 8.92%; Found: C 38.36%, H 2.25%, N 8.73%.

^1H NMR: 1H NMR (CD_3Cl, 200 MHz): δ = 8.35(d, J = 8.6 Hz,2H), 8.78 (s,2H), 7.99 (d, J = 2.4, Hz,2H) ppm. Mass Spec. m/z 315(M^+)

2.3.1.2. 5,5′–Diphenyl–2,2′–bipyridine

5,5′–Dibromo–2,2′–bipyridine (471 mg, 1.50 mmol) and tetrakis(triphenyl–phosphine)palladium(0) (14 mg, 0.012 mmol) were added to 48 ml of

toluene and the solution was degassed for 30 min with argon. Degassed sodium carbonate solution in water (15 ml, 2M) was added, and the mixture was degassed for a further 30 min under vigorous stirring. Phenylboronic acid (610 mg, 5.00 mmol) was dissolved in 12 ml of warm, oxygen–free MeOH and then added to the toluene/water mixture in one portion. The reaction emulsion was heated to reflux for 48 h under vigorous stirring. After the reaction mixture was cooled to room temperature, the two phases were separated, and the organic layer was dried with magnesium sulfate. After filtering, the solvent was removed *in vacuo*, affording colourless 5,5′–diphenyl–2,2′–bipyridine, yield 23 %.[46]

CHN analysis of $C_{22}H_{16}N_2$. Calculated: C 85.69%, H 5.23%, N 9.08%; Found: C 76.83%, H 5.59%, N 7.00% (recrystallisation may have been required but the compound was deemed pure enough to proceed).

^{1}H NMR (CD_3Cl, 200 MHz): δ = 7.41(m,2H), 7.49(m,4H), 7.65(m ,4H), 8.02 (dd,J = 8.2, 2.4 Hz, 2H), 8.50(dd, J = 8.2, 0.5 Hz,2H) 8.93 (dd, J = 2.4, 0.5 Hz, 2H) ppm. Mass Spec. m/z 309 (M^+)

2.3.2. 5,5′–Dichloro–2,2′–bipyridine

2.3.2.1. 2–Bromo–5–Chloropyridine

This was prepared from 2–amino–5–chloropyridine by the method of Graig. A three–necked flask fitted with a mechanical stirrer, dropping funnel and a thermometer was immersed in a salt freezing mixture; 30 g (2.5 mol) of 63% hydrobromic acid and

(10.2446 g, 0.08 mol) of 2–amino–5–chloropyridine was added, (12 g, 1.5 mol) of bromine was added dropwise during which a solid orange perbromide separated. Then, sodium nitrite (13.7 g, 2 mol) in 20 ml of water was added dropwise so that the temperature did not rise above 0 °C. A solution of NaOH (30 g, 0.75 mol) in water (10 ml) was added, keeping the temperature below 25 °C. The mixture was extracted with diethylether (6 x 5 ml).[47]

CHN analysis of C_5H_3ClBrN. Calculated: C 31.25%, H 1.56%, N 7.29%; Found: C 30.98%, H 1.47%, N 7.10%.

2.3.2.2. 5,5′–Cl_2–bpy

A mixture of base (N,N–diisopropylethylamine, 99%) (1.0332 g, 8 mmol), palladium acetate (0.0902 g, 0.4 mmol), tetra–n–butylammonium bromide (1.2917 g, 4 mmol) and 2–bromo–5–chloropyridine (1.5387 g, 8 mmol) in toluene (50 ml) was stirred under dinitrogen atmosphere for few minutes at 105 °C. Isopropanol (0.4805 g, 8 mmol) was added and the mixture was held at 105 °C for 20 h. After cooling to room temperature, water and ether were added. The organic phase was washed with water and dried over $MgSO_4$. The solvent was evaporated under vacuum. The product was purified by crystallization from ethanol, yield = 43 %.[48]

CHN analysis of $C_{10}H_6N_2Cl_2$. Calculated: C 53.33%, H 2.67%, N 7.31%; Found: C 52.63%, H 2.86%, N 11.37%.(further recrystallisation from ethanol may have been required but the compound was deemed pure enough to proceed).

^{1}H NMR (CD_3Cl,199.972 MHz): δ = 8.610(d, J = 2.343 Hz,2H), 8.349 (d, J = 8.594 Hz,2H), 7.789 (dd, J = 8.593, 2.343 Hz,2H) ppm. Mass Spec. m/z 225 (M^+)

2.3.3. 6,6′–Dichloro–2,2′–bipyridine

2,2′–Bipyridine (20 g, 0.128 mol) was dissolved in 70 ml of dimethyl sulfate under dinitrogen ; the solution was heated to reflux until the appearance of a white hygroscopic solid, 1,1′–dimethyl–2,2′–bipyridine sulfate, which was washed with diethylether under dinitrogen and dissolved without further purification in 500 ml of water below 5 °C. Potassium ferricyanide (120 g, 0.365 mol, dissolved in 400 ml of water) and sodium hydroxide (150 g, 3.75 mol, dissolved in 500 ml of water) were simultaneously added dropwise to the former solution over 3 h. The pH was adjusted to 8–9 with some drops of 37% hydrochloric acid at the end of the addition. The product 1,1′–dimethyl–2,2′–bipyridine–6,6′(1H,1′H)–dione, was extracted with chloroform and precipitated by evaporation. It was crystallized from chloroform yielding 12 g of the product. Then, 7 g, 0.0324 mol, were mixed under nitrogen with 15 g, 0.0719 mol, of phosphorus(v)chloride and 140 ml of phosphoryl chloride; the solution heated to reflux for 20 h and the excess of phosphoryl chloride removed by vacuum distillation. The remaining solid, 6,6′–dichloro–2,2′–bipyridine was neutralized with ammonia and recrystallized from chloroform. Yield = 68.80 %.[49]

CHN analysis of $C_{10}H_6N_2Cl_2$. Calculated: C 53.36%, H 2.69%, N 12.48%; Found: C 50.57%, H 3.52%, N 12.05 % (further recrystallisation from chloroform may have been required but the compound was deemed pure enough to proceed).

^{1}H NMR (CD_3Cl, 200 MHz): δ = 8.30 (d, J = 7.5 Hz,2H), 7.75 (t, 2H), 7.22 (d, J = 7.5 Hz,2H) ppm. Mass Spec. m/z 225 (M^+)

2.3.4. 4–Nitro–4′–chloro–bipyridine

4,4′–$(NO_2)_2$–bpy–N,N′–dioxide (109 mg, 0.393 mmol) and acetonitrile (10 ml) were heated to reflux with PCl_3 (1 ml) for 2h and 15 minutes. After 10 min the suspension became a homogeneous solution. The solution was allowed to stand at room temperature overnight. Then, the reaction mixture was thrown into ice–water (5 ml). This mixture was evaporated to leave an aqueous phase that was, basified with concentrated KOH to pH 11, and repeatedly extracted with chloroform (16 ml). After drying the combined chloroform extracts over K_2CO_3, the solvent was removed. Chromotography was carried out with ethyl acetate and hexane to give 4–chloro–4′–nitro–bipyridine as a yellow solid, yield = 60 %.[50]

CHN analysis of $C_{10}H_6N_3O_2Cl$. Calculated: C 50.97 %, H 2.57 %, N 17.83 %; Found : C 49.60% , H 3.06% , N 15.07 %.

^{1}H NMR (CD_3Cl, 200 MHz): δ = 8.45(s,1H), 8.52 (s, 1H), 8.96 (d, J = 5.0,1H), 8.63 (d, J = 7.0,1H) 8.13 (d, J = 8.1,1H), 7.40 (d, J = 7.4,1H) ppm. Mass Spec. m/z 236 (M^+)

2.3.5. 2–Cl–4–NO_2–py

Following the procedure of Hamana, a mixture of 2–chloro–4–nitropyridine–N–oxide (2 g), ethyl acetate (30 ml) and phosphorus trichloride (2.9 ml) was heated with stirring at 70 °C for 10 minutes. The mixture was cooled to room temperature, poured onto an ice–water mixture, made alkaline to litmus with 10% aqueous sodium hydroxide and extracted with chloroform. After drying the combined chloroform extracts, the solvent was evaporated to give 80 % yield of 2–chloro–4–nitropyridine as light yellow needles.[51]

CHN analysis of $C_5H_3N_2O_2Cl$. Calculated: C 37.97%, H 1.89%, N 17.72%; Found: C 37.40 %, H 1.89%, N 17.01%.

^{1}H NMR (CD_3Cl, 200 MHZ): δ = 7.99(dd, J = 3.8,2.6 Hz,1H), 8.73 (d, J = 5.20 Hz,1H), 8.09 (1H) ppm. Mass Spec. m/z 159 (M^+)

2.3.6. 4,4′–$(NO_2)_2$–6,6′–Cl_2–bpy

4,4′–Dinitro–2,2′–bipyridine N,N′–dioxide (0.65 g, 0.0023 mol) was heated to reflux with $POCl_3$ (15 ml) for 5 hr, after which period the evolution of brown nitrogen dioxide had ceased. Excess $POCl_3$ was removed *in vacuo* and the residue was treated with water (25 ml). The pale yellow solid was collected by filtration and washed well with hot MeOH (50 ml) to give a white solid, which was recrystallised from DMF to give white plates of 4,4′–$(NO_2)_2$–6,6′–Cl_2–bpy, yield = 13 %.[52]

CHN analysis of $C_{10}H_4N_4O_4Cl_2$. Calculated: C 38.22 %, H 1.27 % , N 17.83 %; Found : C 34.82% , H 1.46% , N 17.20 % (further recrystallisation from DMF may have been required but the compound was deemed pure enough to proceed).

^{1}H NMR (CD_3Cl, 200 MHZ): δ = 7.91(d, J = 1.5 Hz,1H), 8.90 (d, J = 1.5 Hz,1H), ppm. Mass Spec. m/z 317 (M^+).

2.3.7. 4–Cl–bpy

4–Nitro–2,2′–bipyridine–1–oxide (0.75 g) was heated to reflux with acetyl chloride (30 ml) for 1hr. The reaction mixture was cooled to 0 °C and phosphorus trichloride (5 ml) was added dropwise. The solution was heated to reflux for a further 2 hrs and then cooled to room temperature. The solution was poured onto ice water (50ml) and extracted with dichloromethane. The extracts were dried ($MgSO_4$), filtered and evaporated. The crude mixture was sublimed at 67 °C to give the product as fine white needles. (yield =0.1093 g, 17 %).[53]

CHN analysis of $C_{10}H_7N_2Cl$: Calculated: C 69.03 %, H 3.67 %, N 14.699 %; Found C 65.64 %, H 4.20 %, N 15.38 %.(further sublimation may have been required but the compound was deemed pure enough to proceed).

^{1}H NMR (CD_3Cl, 200 MHz): δ = 7.25(m, 2H), 7.82 (t, 1H), 8.40 (d, ,1H) 8.44(1H,dd), 8.55 (1H,d) , 8.67 (1H,d)ppm. Mass Spec. m/z 191 (M^+).

2.3.8. 4–NO_2–bpy

2.3.8.1. 2,2′–bpy N–oxide.

A solution of 2,2′–bpy (12.012 g, 7.69×10^{-2} moles) in $CHCl_3$ (43 ml) was stirred at 0 °C for 35 minutes. A solution of *m*–chloroperbenzoic acid (15.450 g, 9×10^{-2} moles) in $CHCl_3$ (150 ml) was then added dropwise over 80 minutes. The mixture was stirred at room temperature for 13.5 hours, then washed three times with 200 ml portions of 5 % Na_2CO_3, dried ($MgSO_4$) and evaporated. To remove the unreacted 2,2′–bpy, the residual oil was extracted with boiling hexane. The extract was evaporated and the residue kept under vacuum, giving the hygroscopic solid 2,2′–bpy N–oxide (3.650 g, 2.12×10^{-2} moles, percentage yield 28 %)[50]

2.3.8.2. 4–NO_2–bpy–N–oxide.

A stirred solution of 2,2′–bpy N–oxide (3.34 g, 1.94×10^{-2} moles), potassium nitrate (10.4 g, 0.1 moles) and concentrated sulfuric acid (26 ml) was heated to reflux for 23 hours. The reaction was poured onto ice (50 g) and neutralised to pH 8.5 using 38.5% NaOH. The pale yellow precipitate was filtered and washed with ice water. The precipitate was dissolved in $CHCl_3$ (100 ml) and shaken with water. The aqueous layer was extracted repeatedly with $CHCl_3$. The combined $CHCl_3$ layers were dried ($MgSO_4$), filtered and evaporated to yield 4–NO_2–bp–N–oxide (1.631 g, 7.51×10^{-3} moles, yield 39 %).

CHN analysis of $C_{10}H_7N_3O_3$: Calculated: C 55.31 %, H 3.25 %, N 19.34 %; Found: C 56.20 %, H 3.40 %, N 19.43 %.

2.3.8.3. 4–NO_2–bpy.

4–NO_2–bpy–N–oxide (1.55 g, 7.14×10^{-3} moles) and PCl_3 (25 ml) were heated to reflux together for 21 hours. The reaction was thrown into ice water (200 ml) and then worked up as described for 4,4′–$(NO_2)_2$–bpy. The orange/brown crystals obtained were recrystallised from DCM:hexane to yield 4–NO_2–bpy (0.127 g, 6.31×10^{-4} moles, yield 9 %).

CHN analysis for $C_{10}H_7N_3O_2$: Calculated: C 59.70 %, H 3.51 %, N 20.89 %; Found C 59.38 %, H 3.43 %, N 20.66 %. Mass Spec. m/z 202 (M^+)

2.4. Synthesis of Pt complexes

The complexes [Pt(5,5′–Cl_2–bpy)Cl_2], [Pt(5,5′–Ph_2–bpy)Cl_2], [Pt(5,5′–Br_2–bpy)Cl_2], [Pt(4–Cl–4–NO_2–bpy)Cl_2] and [Pt(4–Cl–bpy)Cl_2] were all prepared by the following general procedure. A suspension of the appropriate ligand (1.1 equivalents) was heated under reflux, with stirring, in an aqueous solution of $K_2[PtCl_4]$ (1 equivalent). The precipitate was collected by filtration, washed with water, dried under vacuum and recrystallised from *N,N′*–dimethylformamide (DMF) solution. The analytical results for all complexes are given in Table 2.1.

Compound	Colour	C %	H %	N %	Mass Spec m/z (M_+)
$Pt(4\text{-}Cl\text{-}4\text{-}NO_2\text{-}bpy)Cl_2]^{(c)}$	red brown	23.94 (a)	1.21	8.38	503
		26.50 (b)	2.23	8.05	
$[Pt(5,5'\text{-}Ph_2\text{-}bpy)Cl_2]$	Green	45.99 (a)	2.81	4.88	574
		43.56 (b)	2.31	5.12	
$[Pt(5,5'\text{-}Br_2\text{-}bpy)Cl_2]^{(c)}$	dark yellow	20.71 (a)	1.04	4.83	578
		25.19 (b)	2.09	5.62	
$[Pt(4'\text{-}Cl\text{-}bpy)Cl_2]$	dark green	26.29 (a)	1.55	6.16	457
		24.03 (b)	1.19	5.46	
$[Pt(5,5'\text{-}Cl_2\text{-}bpy)Cl_2]$	Orange	24.45 (a)	1.22	5.71	489
		24.67 (b)	1.39	4.80	
$[Pt(4,4'\text{-}(NO_2)_2\text{-}bpy)Cl_2]$	Green	23.04 (a)	0.91	1.035	512
		23.58 (b)	1.16	9.09	

Table 2.1 Analytical data for the compounds studied in this thesis. (a) calculated, (b) found. (c) Further purification was required via recrystallisation from DMF.

Several attempts to synthesise $[Pt(6,6'\text{–}Cl_2\text{–}bpy)Cl_2]$ following the general procedure above and another one by Beilli *et al.*[99] have failed. In an another attempt to synthesise $[Pt(6,6'\text{–}Cl_2\text{–}bpy)Cl_2]$, a solution of $6,6'\text{–}Cl_2\text{–}bpy$ (0.141 g, 6.30×10^{-4} moles) in dilute HCl (5 ml) was added to a solution of $K_2[PtCl_4]$ (0.250 g, 6.02×10^{-4} moles) in H_2O (20 ml) and was placed in a sealed Teflon container and heated at 100 °C for 12 hours.

However, this attempt was unsuccessful. The complex, [Pt(4,4′–NO_2–6,6′–Cl_2–bpy)Cl_2] could not be obtained.

2.5. Synthesis of $TBABF_4$ electrolyte.

Tetrafluoroboric acid (120 ml, 50 %) was dissolved in water (500 ml) and tetrabutylammonium hydroxide (660 ml, 40 %) was added until neutralisation was achieved (pH 7). More water (1 L) was added to ensure efficient stirring. The white precipitate of [TBA][BF_4] was filtered, recrystallised twice from a 1:1 mixture of methanol:water and dried in a vacuum oven before use, analysis for $C_{16}H_{36}NBF_4$ Calculated: C 58.56 %, H 11.02 %, N 4.25 %; Found: C 58.37 %, H 10.00 %, N 4.25 %.

2.6. Purification and drying solvents

DCM (Dichloromethane) was stored over KOH for two weeks prior to distillation from phosphorus pentoxide P_2O_5. MeCN (acetonitrile) was heated to reflux over aluminium chloride for 1 hour, followed by rapid distillation. The distillate was heated to reflux over alkaline potassium permanganate for 15 minutes followed by rapid distillation. The distillate was heated to reflux over potassium bisulphate ($KHSO_4$) for 1 hour followed by rapid distillation. The distillate was then refluxed over calcium hydride for 1 hour followed by a careful fractionation from a helice packed column at a high reflux ratio. The middle 80% fraction was retained and distilled three times from phosphorus pentoxide. The purified and dried MeCN was freshly distilled from phosphorus pentoxide before use. All other solvents were used as purchased *puriss* (>99.5 %).[88]

2.7. CaChe Calculations.

CAChe is a computer–aided molecular design modelling tool. In this work CAChe 3.2 software was used.

3. Chloro–substituted 2,2′–bipyridines.

3.1. Introduction.

In this chapter, the characterization of several chloro–substituted bpy molecules and their Pt complexes is described. Results are compared with those of 4,4′–Cl_2–bpy which has been studied previously electrochemically and spectrochemically by McInnes.[31]

3.1.1. Electrochemistry of 4,4′–Cl_2–bpy.

The electrochemical measurements of 4,4′–Cl_2–bpy in 0.1 M $TBABF_4$/DMF solution reveals a one–electron reduction at –1.69 V, which is chemically irreversible showing no anodic peak at all temperatures and scan speeds studied.[31] Due to this irreversibility, the reduction process could not be studied in any detail. However, [Pt(4,4′–Cl_2–bpy)Cl_2] has been synthesised and its redox chemistry reinvestigated in this thesis.

A cyclic voltammetric study of [Pt(4,4′–Cl_2–bpy)Cl_2] in 0.1 M [TBA][BF_4]/DMF showed a fully reversible reduction at –0.83 V, and an irreversible reduction at –1.65 V.[31] A spectroelectrochemical study in 0.1 M [TBA][BF_4]/DMF at 243 K showed the expected transitions in the visible and UV regions for a reduced bpy ligand. The lowest energy features in the UV/Vis spectrum of the complex were assigned to MLCT (d–π*) transitions, by comparison with [Pt(bpy)Cl_2] and the higher energy bands were assigned as internal ligand π–π* transitions.[31]

3.1.2. EPR spectra of $[Pt(4,4'–Cl_2–bpy)Cl_2]^{1–}$.

The bulk electrochemical reduction of $[Pt(4,4'–Cl_2–bpy)Cl_2]$ in DMF solution at 243 K yielded an EPR active solution. The EPR spectrum of $[Pt(4,4'–Cl_2–bpy)Cl_2]^{1–}$ at room temperature showed a broad central line with ^{195}Pt satellites. This had previously been explained as the coupling of the unpaired electron to the Pt nucleus with coupling to ligand nuclei unresolved. When the complex is reduced with $Na[BH_4]$ it gave an identical spectrum to that generated electrochemically.[31]

On cooling to 77 K a rhombic X–band EPR spectrum was obtained similar to that observed by McInnes for $[Pt(bpy)Cl_2]^{1–}$.[31] The g and A values are shown in Table 3.1,[31] A_3 can be estimated from the magnitudes of A_{iso}, A_1 and A_2 using Equation 3.1.

$$A_3 = 3\,A_{iso} - (A_1 + A_2) \qquad \textbf{Equation 3.1}$$

	g_{iso}[a]	g_1[b]	g_2	G_3	A_{iso} (Pt)[c]	A_1[c]	A_2[c]	A_3[c]
$[Pt(4,4'-Cl_2-bpy)Cl_2]^{1-}$	2.000	2.042	2.014	1.944	-51	-52	-96	(-5)

Table 3.1 EPR data for $[Pt(4,4'-Cl_2-bpy)Cl_2]^{1-}$. All parameters were estimated directly from spectra.

(a) Isotropic data from chemically generated species in DMF. (b) Anisotropic data electrochemically generated species in 0.1 M [TBA][BF_4]/DMF. (d) A/10^{-4} cm^{-1}.

3.2. Aims of this chapter.

In this chapter, additional chloro–substituted bipyridine pro–ligands have been studied and their electrochemical properties are reported and compared with their dichloroplatinum(II) complexes. The effects of changing the position of the chloro substituents on the electronic properties of the molecules are examined. The redox chemistry and spectroelectrochemistry (UV/Vis/nir, EPR) of 5,5′–Cl_2–bpy, 6,6′–Cl_2–bpy and 4–Cl–bpy and of the complexes [Pt(5,5′–Cl_2–bpy)Cl_2], and [Pt(4–Cl–bpy)Cl_2] are described and discussed.

3.3. Results and discussion.

3.3.1. 5,5′–Cl_2–bpy, 6,6′–Cl_2–bpy and 4–Cl–bpy.

3.3.1.1. Crystal structures of 5,5′–Cl_2–bpy and 6,6′–Cl_2–bpy.

The preparations of 5,5′–Cl_2–bpy and 6,6′–Cl_2–bpy are described in Chapter 2. Crystals suitable for X–ray structure determination were obtained by slow evaporation of a chloroform solution of 5,5′–Cl_2–bpy and by recrystallisation of 6,6′–Cl_2–bpy from dimethylformamide. Crystal data and details of the X–ray structure determinations are summarised in Table 7.1 and 7.2.

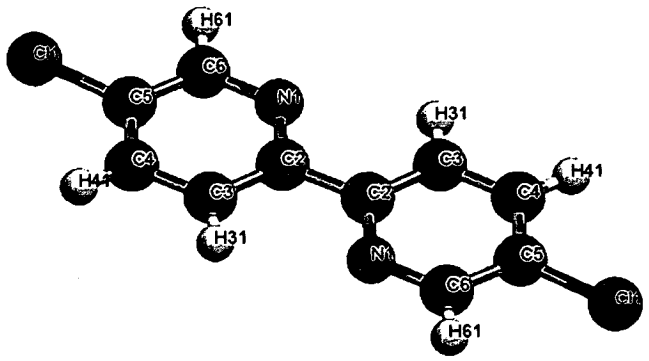

Figure 3.1 The X-Ray crystal structure of 5,5′-Cl_2-bpy showing the atom labelling used in Tables 3.2 and 3.3.

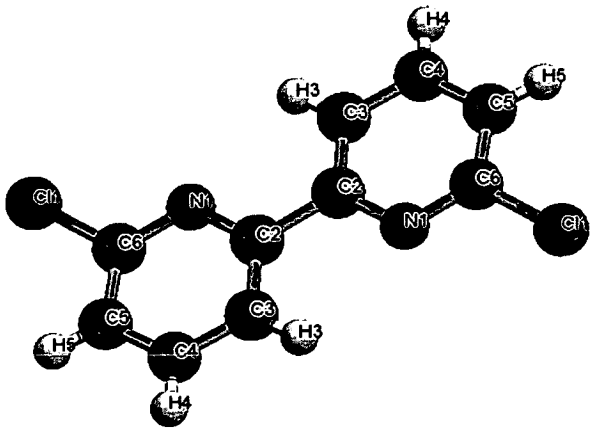

Figure 3.2 The X-Ray crystal structure of 6,6′-Cl_2-bpy showing the atom labelling used in Tables 3.2 and 3.3

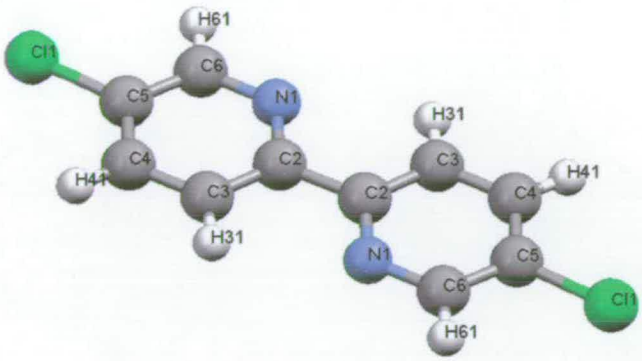

Figure 3.1 The X-Ray crystal structure of 5,5′-Cl_2-bpy showing the atom labelling used in Tables 3.2 and 3.3.

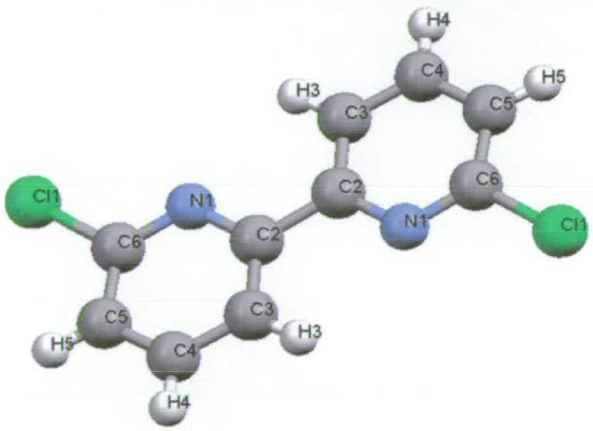

Figure 3.2 The X-Ray crystal structure of 6,6′-Cl_2-bpy showing the atom labelling used in Tables 3.2 and 3.3

Atoms	5,5'-Cl_2-bpy Bond lengths/Å	6,6'-Cl_2-bpy Bonds lengths/ Å
N(1)-C(2)	1.345(3)	1.350(3)
N(1)-C(6)	1.336(3)	1.318(3)
Cl(1)-C(5)	1.735(3)	-
Cl(1)-C(6)	-	1.748(2)
C(2)-C(2)#1	1.481(5)	1.490(4)
C(2)-C(3)	1.398(4)	1.390(3)
C(3)-C(4)	1.385(4)	1.388(3)
C(4)-C(5)	1.389(4)	1.385(3)
C(5)-C(6)	1.382(4)	1.389(3)

Table 3.2 Bond lengths (Å) obtained from the X-ray structure determinations of 5,5′-Cl_2-bpy and 6,6'-Cl_2-bpy.

Atoms	5,5'-Cl_2-bpy Bond Angles	6,6'-Cl_2-bpy Bond angles
C(2)-N(1)-C(6)	118.6(2)	116.7(2)
C(2)#1-C(2)-N(1)	116.4(3)	116.3(2)
C(2)#1-C(2)-C(3)	121.1(3)	121.2(2)
N(1)-C(2)-C(3)	122.6(2)	122.5(2)
C(2)-C(3)-C(4)	118.9(2)	119.0(2)
C(3)-C(4)-C(5)	117.6(2)	119.3(2)
C(4)-C(5)-C(6)	120.8(2)	116.6(2)
Cl(1)-C(5)-C(6)	118.7(2)	-
Cl(1)-C(6)-C(5	-	118.47(19)
C(5)-C(6)-N(1)	121.6(2)	125.9(2)

Table 3.3 Bond angles (°) for 5,5′-Cl_2-bpy and 6,6′-Cl_2-bpy obtained from X-ray crystallography.

The structure of 5,5′–Cl_2–bpy and 6,6′–Cl_2–bpy revealed that the two rings of py in both molecules were planar to each other (Figure 3.1 and 3.2). The pyridine N atoms are *trans* to one another in agreement with other 2,2′–bpy molecules.[5–7] The distances and bond angles (Table 3.2 and 3.3) are all as expected for a substituted 2,2′–bipyridine molecule.

3.3.1.2. Electrochemistry of chloro–substituted 2,2'–bipyridine molecules .

The electrochemistry of the chloro–substituted bipyridine molecules was studied by cyclic voltammetry of the molecules in a solution of 0.1 M [TBA][BF_4] in DMF at 293

K, unless otherwise stated. 5,5′–Cl_2–bpy and 4–Cl–bpy in 0.1M [TBA][BF_4]/DMF showed one irreversible reduction at –1.74 V and –1.84 V respectively, see Figure 3.3 and 3.4. Complete reversibility could not be achieved even at low temperature and spectroelectrochemical techniques, therefore, could not used to study these molecules.

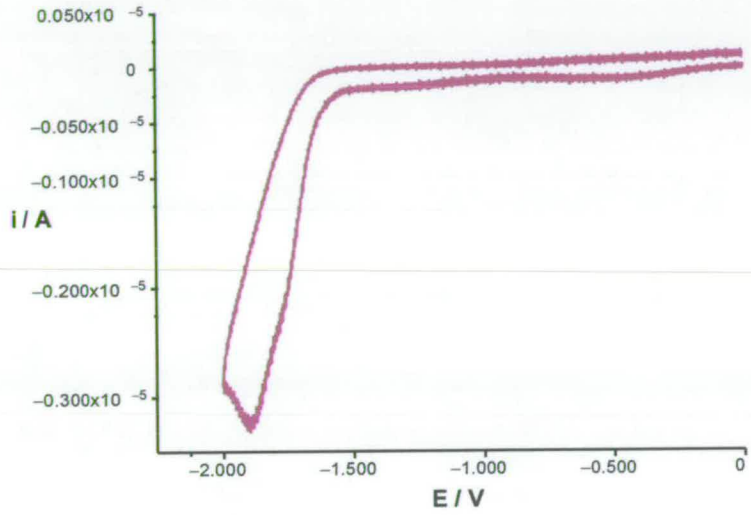

Figure 3.3 Cyclic voltammogram of 5, 5′-Cl_2-bpy in 0.1 M [TBA][BF_4]/DMF, vs. Ag/AgCl, at 293 K, scan rate 0.1 Vs^{-1}.

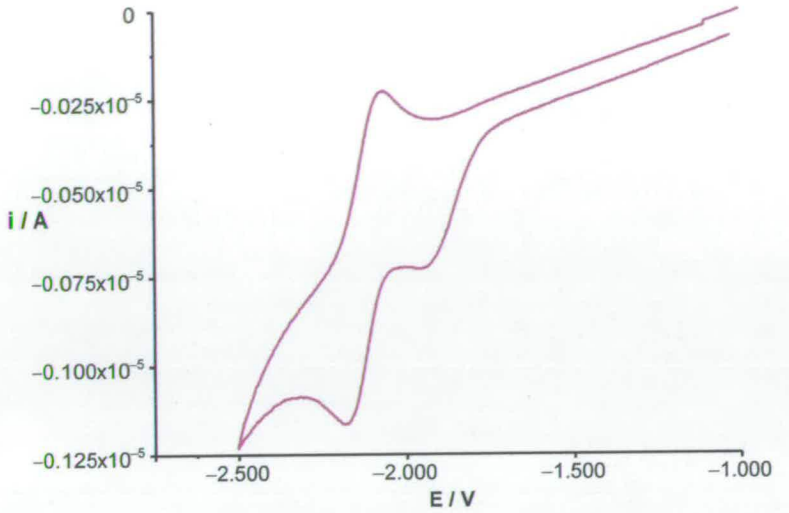

Figure 3.4 Cylic voltammogram of 4-Cl-bpy in 0.1 M [TBA][BF_4]/DMF, vs. Ag/AgCl, at 293 K, scan rate 0.1 Vs^{-1}.

In the case of 4–Cl–bpy, the irreversible reduction was followed by reduction of a daughter product which was fully reversible, see Figure 3.4. It is believed that this daughter product is the free bipyridine molecule, as the reduction at –2.05 V matches that of the unsubstituted bpy, see Figure 3.5. Also, addition of bpy to the cyclic voltammetry solution of 4–Cl–bpy resulted in an increase in the height of the peak at –2.05 V.

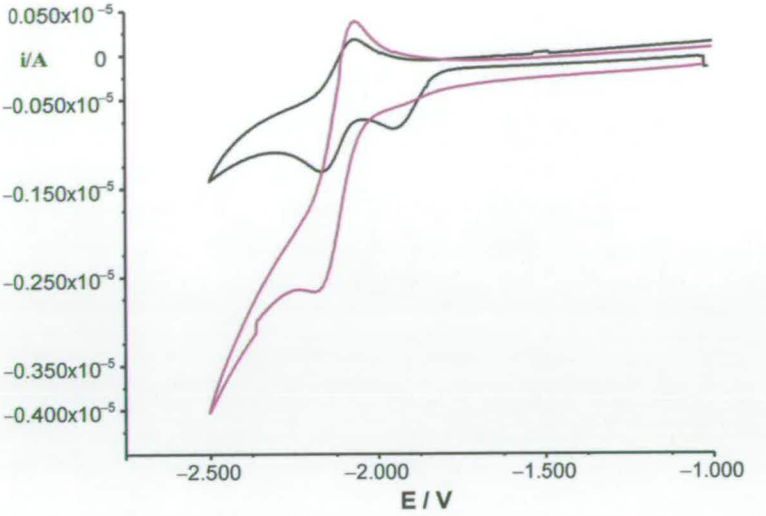

Figure 3.5 The cyclic voltammetric response of 4–Cl–bpy (black scan) and bpy (purple scan) in 0.1M [TBA][BF_4]/DMF , *vs.* Ag/AgCl, at 293 K, scan rate 0.1 Vs^{-1}.

On comparing the $E_{½}$ value of the mono–substituted pro–ligand (4–Cl–bpy) with the di–substituted pro–ligand (4,4′–Cl_2–bpy) and with bipyridine (bpy), a clear trend was found, see Table 3.4.

Compound	$E_{½}$ /V
bpy	-2.05[a]
4-Cl-bpy	-1.84
4,4′-Cl_2-bpy	-1.69

Table 3.4 $E_{½}$ of chloro-substituted bpy and the unsubstituted bpy.

(a) Irreversible reduction, for which no anodic peak was observed, cathodic peak potential is quoted.

From the data presented in Table 3.4, the $E_{½}$ value for the monochloro–substituted bipyridine ligand is approximately half way between $E_{½}$ potentials of the unsubstituted and dichloro substituted 2,2′–bipyridine. This implies an additive effect of the electron withdrawing chloro–group.

6,6′–Cl_2–bpy in 0.1 [TBA][BF_4]/DMF showed a reduction process at –1.63 V. This molecule proved to be a good example of the effects of changing the scan rate and temperature on the reversibility of the electrochemistry. Initially at a scan rate of 0.1 Vs^{-1} 6,6′–Cl_2–bpy exhibited an irreversible reduction, followed by the reduction of a daughter product at –1.95 V. However a more reversible process is observed by increasing the scan rate and/or decreasing the temperature. Figure 3.6 shows the effect of changing scan rate from 0.1 to 0.8 Vs^{-1}on the reversibility of reduction at room temperature.

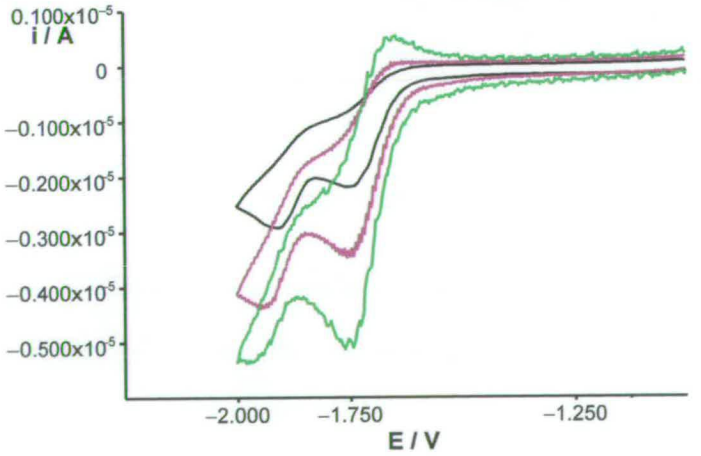

Figure 3.6 Cyclic voltammetric behaviour of 6,6′-Cl_2-bpy in 0.1 M [TBA][BF_4]/DMF, vs. Ag/AgCl, at 298 K at scan rates of 0.1 V s^{-1}, 0.2 V s^{-1} and 0.8 Vs^{-1}(black, purple and green lines respectively).

Increasing the scan rate results in an increased return wave and a relative decrease in the intensity of the wave associated with the daughter product. Thus by increasing the scan rate the following chemical reaction is out–run. Decreasing the temperature inhibits the following chemical reaction such that at 233 K the electron transfer process is fully reversible and no decomposition product was observed, see Figure 3.7.

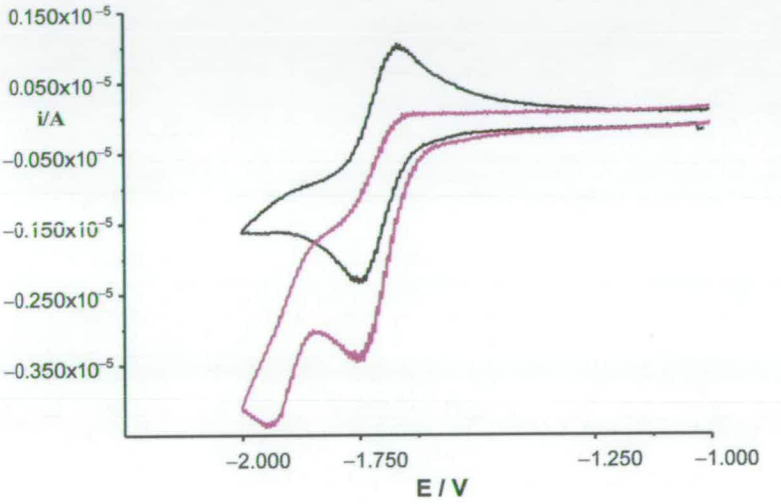

Figure 3.7 Cyclic voltammogram of 6,6′-Cl_2-bpy in 0.1 M [TBA][BF_4]/DMF, vs. Ag/AgCl, at 293 K and 233 K (purple and black traces) with a scan rate of 0.1 Vs^{-1}.

The reduction of 6,6′–Cl_2–bpy was investigated in different solvents to study their effect on the reversibility and $E_{½}$ value of the process, see Table 3.5.

Solvent	Acceptor Number	$E_{½}$ /V
Acetonitrile	18.9	-1.65
Dimethylsulphoxide	19.3	-1.65
Dimethylformamide	16.0	-1.63
Pyridine	14.2	-1.68
Tetrahydrofuran	8.0	-1.67

Table 3.5 $E_{½}$ values for reduction of 6,6′-Cl_2-bpy in different solvents at 293 K

The half wave potential values varied only from −1.63 V to −1.68 V, and we concluded that there is no measurable solvent effect.

To examine whether or not the chloro–substituent is released from the compound during the course of the electrochemical reduction, two experiments were undertaken. In the first one the cyclic voltammogram of 6,6'–Cl_2–bpy was compared in 0.1 M [TBA][BF_4] and in 0.1 M [TBA]Cl. The results were indistinguishable. If chloride was released on reduction then we would expect [TBA]Cl to slow down the release of chloride and hence for the cyclic voltammetric wave to become more reversible. In the second experiment the reduced species was generated in bulk using H–cell and then a cyclic voltammogram was run over the potential range where the one electron oxidation of chloride ion is expected. No peak corresponding to this was seen and therefore it was concluded that the chloro–substituent is not being released from the bpy compound on reduction. The identity of the electro–active species formed on reduction of 6,6′–Cl_2–bpy has not been further identified.

As the irreversibile process arises from a chemical reaction which occurs after reduction at low scan rate and high temperature, a kinetic study at varied temperature was undertaken to calculate the activation energy of reaction of $[6,6'–Cl_2–bpy]^{1-}$ in 0.1 M $[TBA][BF_4]$/DMF. Figure 3.8 gives the Arhenius plot of (ln k *vs* 1/T) for the reduction of 6,6′–Cl_2–bpy in DMF which yields a value of E_a of 74.4 kJ mol^{-1}, see Chapter 2 for methodology.

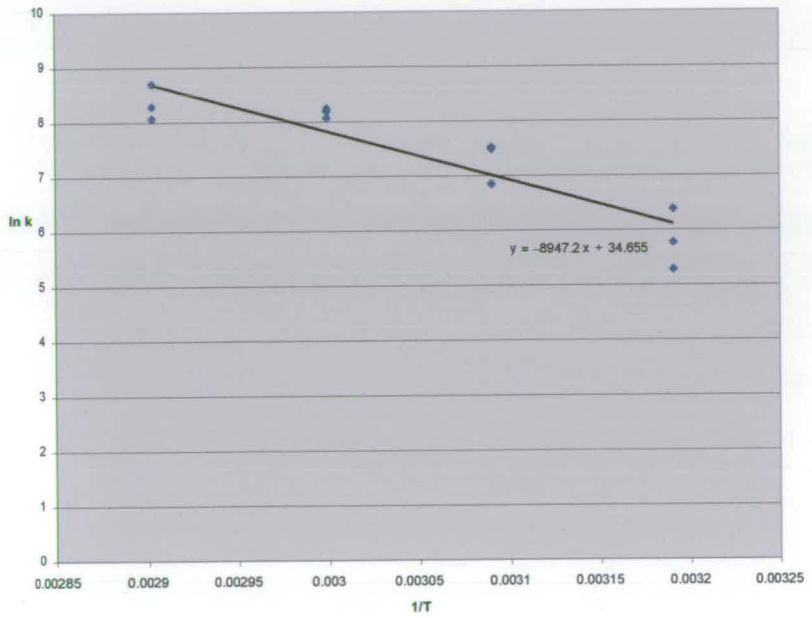

Figure 3.8 A plot of ln k versus 1/T for the one-electron reduction of 6,6′-Cl_2-bpy.

Due to the irreversibility of the reduction of 5,5′–Cl_2–bpy or 4–Cl–bpy, further studies on these free pro–ligands were not undertaken but $[6,6'–Cl_2–bpy]^{1-}$ was studied at 233 K.

3.3.1.2. UV/Vis/nir spectroelectrochemistry of 6,6′–Cl_2–bpy.

The UV/Vis/nir spectroelectrochemistry of 6,6′–Cl_2–bpy was investigated at 233 K in 0.1 M [TBA][BF_4]/DMF. The high energy band at 31,660 cm^{-1} (ε = 7,290 M^{-1} cm^{-1}) of 6,6′–Cl_2–bpy was assigned as an internal bpy $\pi \rightarrow \pi^*$ transition, see Figure 3.9 and Table 3.6. This peak is at lower energy than the corresponding $\pi \rightarrow \pi^*$ transition for the unsubstituted bpy (35,300 cm^{-1}, ε = 1,290 M^{-1} cm^{-1}) because the electron withdrawing chlorine atoms in the 6,6′ positions stabilize the LUMO with respect to bpy. This also has been observed in the potentials for the reduction of 6,6′–Cl_2–bpy which is less negative than the first reduction of bpy. On converting $[6,6'–Cl_2–bpy]^0$ to $[6,6'–Cl_2–bpy]^{1-}$ by holding the potential at –1.80 V, an intense band grows in at *ca.* 25,100 cm^{-1}. A second feature is observed at 18,660 cm^{-1} (ε = 2,900 M^{-1} cm^{-1}) and at 17,370 cm^{-1} (ε = 3,065 M^{-1} cm^{-1}). The spectrum of bpy^{1-} has three sets of diagnostic absorption bands : 1) a nir band at *ca.* 10 kcm^{-1} comprising of three peaks (or shoulders) 2) a doublet visible band at *ca.* 20 kcm^{-1} and 3) an intense near UV band at *ca.* 25 kcm^{-1}. $[6,6'–Cl_2–bpy]^{1-}$ was shown to contain peaks at similar positions. Therefore, the electronic character of the frontier orbitals of bpy and 6,6′–Cl_2–bpy are similar. On reducing $[6,6'–Cl_2–bpy]^0$ to $[6,6'–Cl_2–bpy]^{1-}$, the doublet in the visible region at ~ 20 kcm^{-1} and the intense near UV band at 25 kcm^{-1} are clearly visible in the spectrum of the mono–reduced species and can be assigned as intra ligand transitions of bpy^{1-}. The nir band at *ca.* 10 kcm^{-1} is less easily distinguished but is just observable in Figure 3.10. It can be assigned as the SOMO to LUMO–1 transition. The similarity of the UV/Vis/nir spectrum of $[6,6'–Cl_2–bpy]^{1-}$ to

similarity of the UV/Vis/nir spectrum of $[6,6'–Cl_2–bpy]^{1-}$ to that of $Na^+(bpy^{1-})$ indicates that the additional electron enters an orbital which is primarily based on the bpy part of the molecule. On resetting the electrode potential to 0 V the spectrum goes back to the original base line, *i.e.* the electron transfer is fully chemically reversible, see Figure 3.10. Note that the base line in the nir region of the spectrum collapses on re–oxidation confirming that $[6,6'–Cl_2–bpy]^{1-}$ does indeed have a low energy absorption band.

Oxidation State	Wavenumber /cm^{-1}	ε /$M^{-1}cm^{-1}$
0	31 660	7 290
1-	25 130	5 800
	18 660	2 900
	17 370	3 065

Table 3.6 Peak positions and molar extinction coefficients, ε, for $[6,6'-Cl_2-bpy]^{0/1-}$, in 0.1 M [TBA][BF_4]/DMF at 233 K.

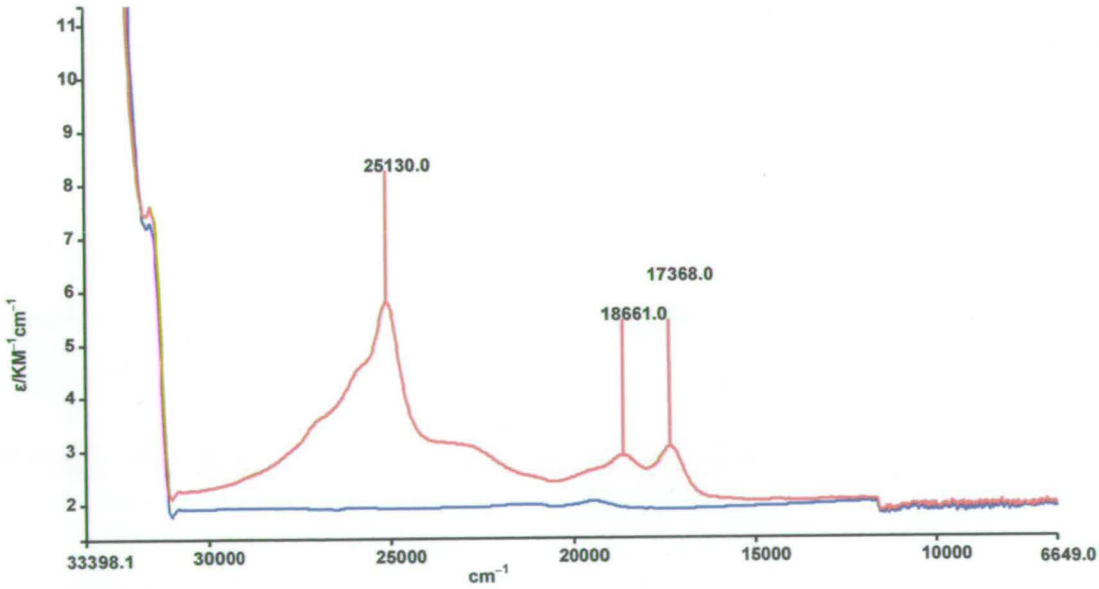

Figure 3.9 UV/Vis/nir spectra of $[6,6'–Cl_2–bpy]^0$ (blue) and $[6,6'–Cl_2–bpy]^{1-}$ (red), E_{gen} = – 1.8 V in 0.1 M [TBA][BF_4]/DMF at 233 K.

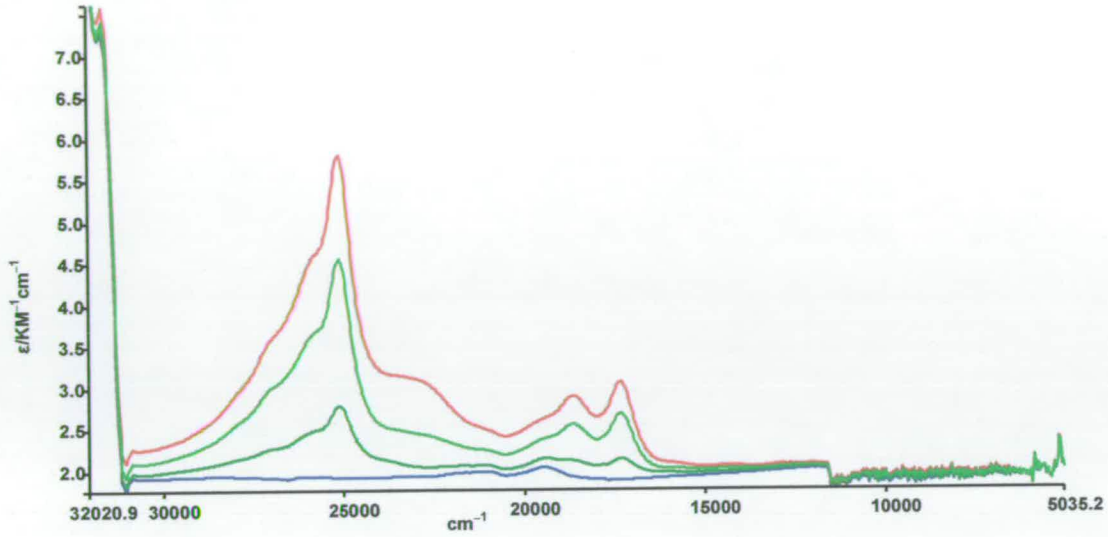

Figure 3.10 UV/Vis/nir spectra of $[6,6'–Cl_2–bpy]^0$ (blue)and $[6,6'–Cl_2–bpy]^{1–}$ (red), E_{gen} = –1.8 V, in 0.1 M [TBA][BF_4]/DMF at 233 K showing partially oxidised curves as the potential is switched back to 0 V.

3.3.1.3. EPR spectroelectrochemistry of $[6,6'–Cl_2–bpy]^{1–}$.

In situ electrochemical reduction of 6,6′–Cl_2–bpy in 0.1 M [TBA][BF_4]/DMF solution at 233 K yielded the EPR active mono–reduced species, see Figure 3.11. The X–band EPR spectrum of $[6,6'–Cl_2–bpy]^{1–}$ can be simulated with coupling to two equivalent ^{14}N nuclei on the bpy (0.950 G), six equivalent ^{1}H nuclei (1.400 G) and two equivalent Cl nuclei (0.132 G). The EPR spectrum of $[6,6'–Cl_2–bpy]^{1–}$ can only be satisfactorily simulated by assuming the unpaired electron occupies a molecular orbital which spans the whole molecule and it is therefore reasonable to assume that monoreduced $[6,6'–Cl_2–bpy]^{1–}$ is planar. Thus, the results of the spectroelectrochemical (UV/Vis/nir,

EPR) experiments are in agreement that the unpaired electron resides in a molecular orbital primarily located on the bpy molecule with a contribution from the Cl substituent.

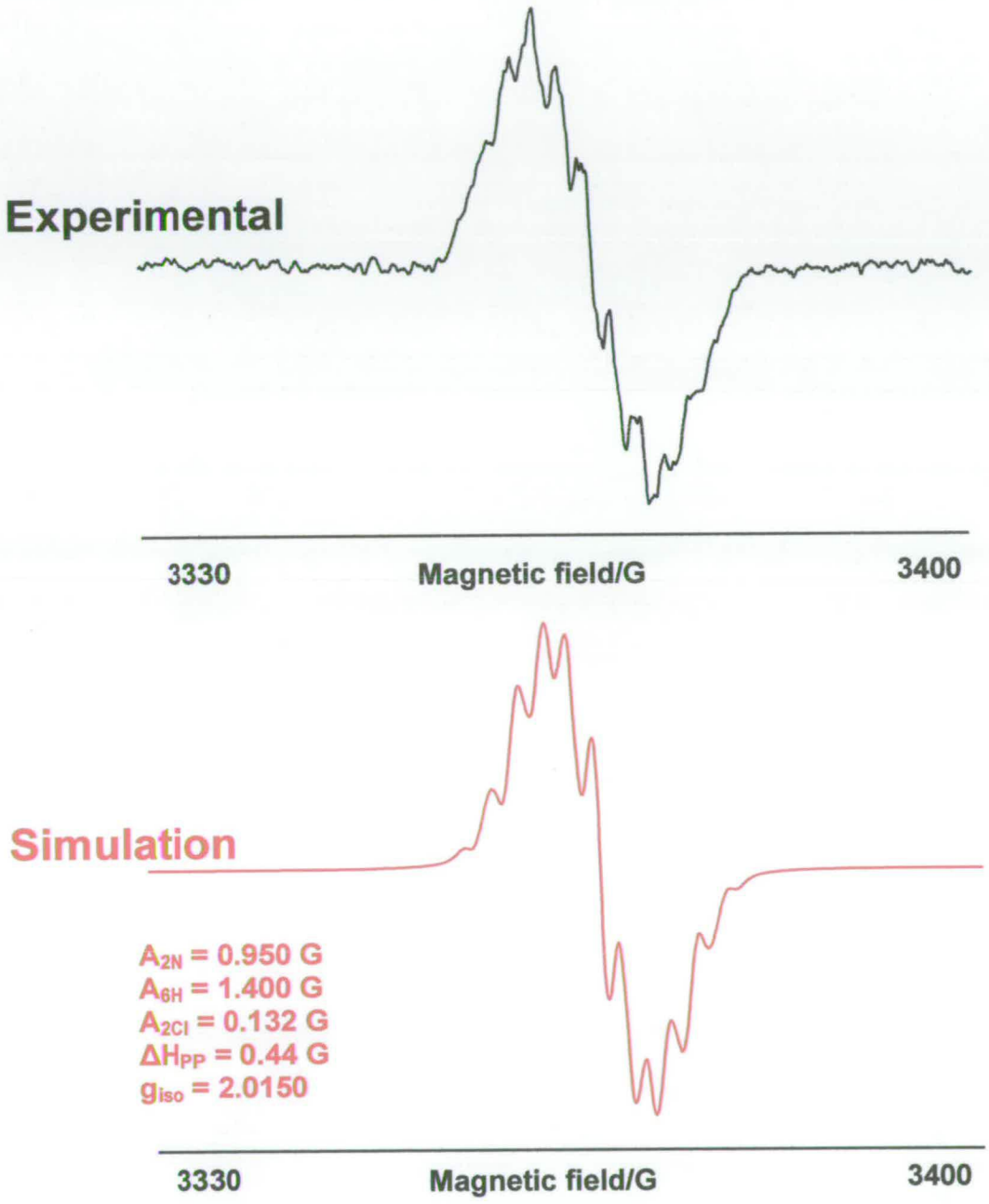

Figure 3.11 Experimental and simulated X–band EPR spectra of $[6,6'–Cl_2–bpy]^{1-}$ generated *in situ* in 0.1 M [TBA][BF_4]/DMF and E_{gen} = –1.8 V at 233 K.

3.3.2. Complexes with Pt(II).

3.3.2.1. Redox Chemistry of [Pt(5,5′–Cl_2–bpy)Cl_2] and [Pt(4–Cl–bpy)Cl_2].

The dichloroplatinum(II) complexes of 5,5′–Cl_2–bpy or 4–Cl–bpy were synthesised and spectroelectrochemical studies were carried out. Unfortunately the dichloroplatinum(II) complex of 6,6′–Cl_2–bpy could not be made, even under high pressure conditions, presumably due to the adverse steric effects of having the pyridine 6–chloro atoms too close to the chloride groups directly bound to the Pt(II) metal centre, see Figure 3. 12.

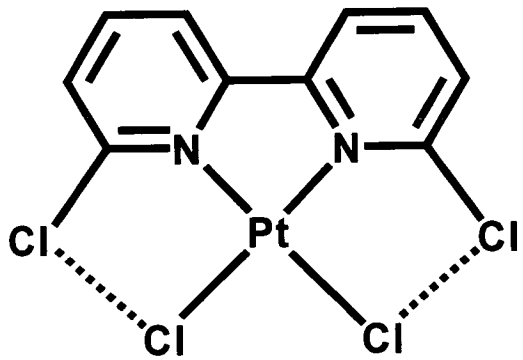

Figure 3.12 Steric problem which would occur in the planar form of [Pt(6,6′-Cl_2-bpy)Cl_2].

Complexes were synthesised as described in Chapter 2, see section 2.4. [Pt(5,5′–Cl_2–bpy)Cl_2] is only sparingly soluble in DMF and other organic solvents. The cyclic voltammogram of [Pt(5,5′–Cl_2–bpy)Cl_2] in 0.1M [TBA][BF_4]/DMF showed a fully reversible reduction at –0.83 V, see Figure 3.13.

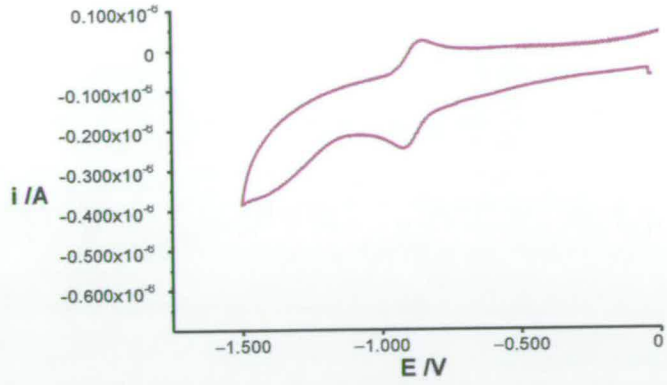

Figure 3.13 Cyclic voltammogram of [Pt(5,5′–Cl_2–bpy)Cl_2] in 0.1 M [TBA][BF_4]/DMF, *vs.* Ag/AgCl, at 293 K, scan rate 0.1 Vs^{-1}.

[Pt(4–Cl–bpy)Cl_2] in 0.1 M [TBA][BF_4]/DMF showed some reversibility at room temperature with a reduction process at –0.79 V. By increasing the scan rate the reversibility improves, see Figure 3.14. Decreasing the temperature was not sufficient to stabilise $[Pt(4–Cl–bpy)bpy]^{1-}$ in the OTTLE experiment. In both Pt complexes the $E_{½}$ potentials are more positive than the free uncoordinated ligands. This is commonly observed for reduced ligands bound to positive metal centers.[32,39,88]

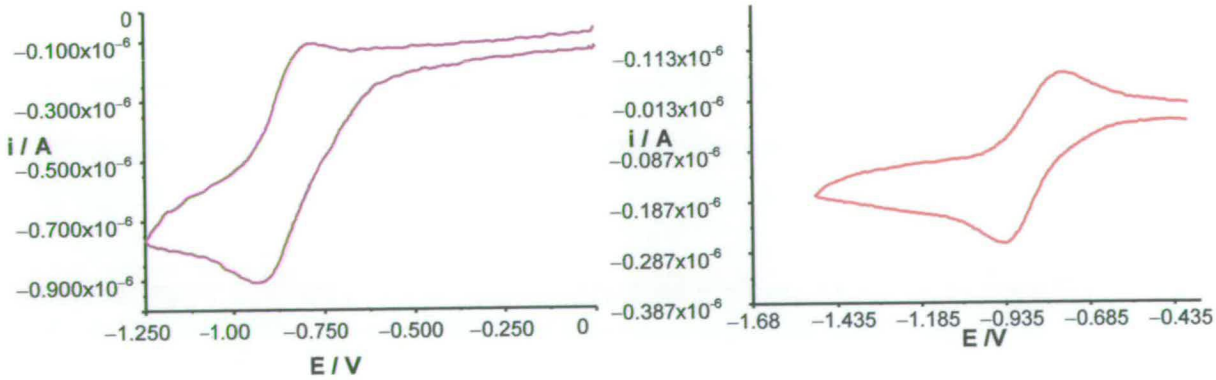

Figure 3.14 Electrochemistry of [Pt(4-Cl-bpy)Cl_2] in 0.1 M [TBA][BF_4]/DMF vs. Ag/AgCl at 0.1 Vs^{-1} (purple) and 0.8 Vs^{-1} (red) at 293 K.

3.3.2.2. UV/Vis/nir spectroelectrochemistry of [Pt(5,5′–Cl_2–bpy)Cl_2].

The spectrum of the neutral compound [Pt(5,5′–Cl_2–bpy)Cl_2] showed low energy bands at 29,180 cm^{-1} (7440 $M^{-1}cm^{-1}$) , 30,330 cm^{-1} (5980 $M^{-1}cm^{-1}$), 34,820 cm^{-1} (10465 $M^{-1}cm^{-1}$) and 37,310 cm^{-1} (9930 $M^{-1}cm^{-1}$) which were all assigned as bpy $\pi \rightarrow \pi^*$ internal transitions in line with related complexes such as [Pt(5,5′–Me_2–bpy)Cl_2].[39] Weaker low energy bands between 22 and 26 kcm^{-1}, see Figure 3.15, are assigned to MLCT ($d \rightarrow \pi^*$) transitions. On reduction to [Pt(5,5′–Cl_2–bpy)Cl_2]$^{1-}$ a broad nir band at around 11,000 cm^{-1}, visible bands at 19,350 cm^{-1}(4636 $M^{-1}cm^{-1}$), 21,000 cm^{-1}(4111 $M^{-1}cm^{-1}$) and 22,500 cm^{-1}(4574 $M^{-1}cm^{-1}$) and a large band at 26,900 cm^{-1} (8122 $M^{-1}cm^{-1}$) grew in. The similarity of the UV/vis/nir spectrum for the mono–reduced [Pt(5,5′–Cl_2–bpy)Cl_2]$^{1-}$ to that of $Na^+(bpy^{1-})$ indicates that the additional electron enters an orbital which is primarily based on the Cl_2–bpy ligand and more precisely is based on the bpy part of the ligand. In agreement with the band assignments of $Na^+(bpy^{1-})$ the absorption bands at 11,000 cm^{-1}, 19,350 cm^{-1}, 21, 000 cm^{-1} and 26,900 cm^{-1} result from intraligand transitions of the mono–reduced 5,5′–Cl_2–bpy ligand while the additional peak at around 22,500 cm^{-1} arises from a charge transfer transition involving the Pt centre and the reduced ligand. When the electrode potential was returned to 0 V the electron transfer was found to be fully chemically reversible as the spectrum returned to that of the starting material.

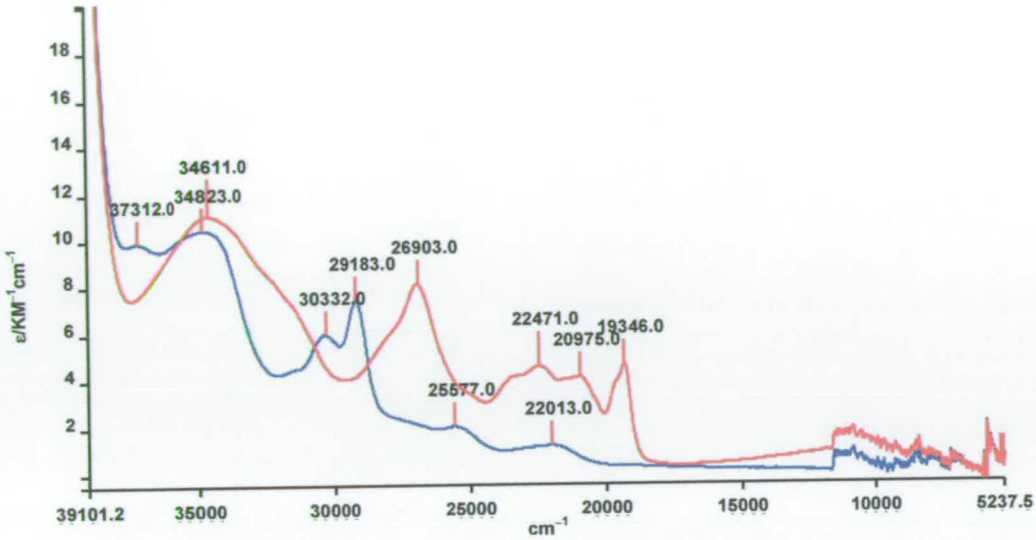

Figure 3.15 UV/Vis/nir spectra of $[Pt(5,5'\text{-}Cl_2\text{-}bpy)Cl_2]^0$ (blue) and $[Pt(5,5'\text{–}Cl_2\text{–}bpy)Cl_2]^{1-}$ (red) in 0.1 M $[TBA][BF_4]$/DMF at 233 K.

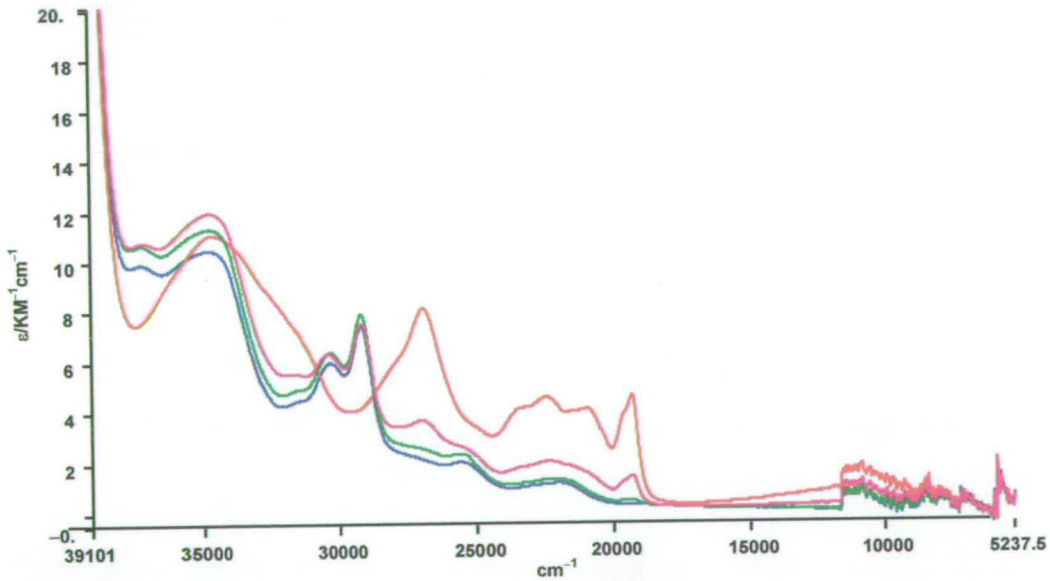

Figure 3.16 UV/Vis/nir spectra of $[Pt(5,5'\text{–}Cl_2\text{–}bpy)Cl_2]^0$ (blue) and $[Pt(5,5'\text{–}Cl_2\text{–}bpy)Cl_2]^{1-}$ (red) in 0.1 M $[TBA][BF_4]$/DMF at 233 K showing partially oxidised curves as the potential is switched back to 0 V.

The isosbestic point at 28,100 cm^{-1} in Figure 3.16 indicates a clean conversion from the mono–reduced anion to the neutral complex. During the conversion from $[Pt(5,5'–Cl_2–bpy)Cl_2]^{1-}$ to $[Pt(5,5'–Cl_2–bpy)Cl_2]^0$ the bands at 29,180 cm^{-1} (7440 $M^{-1}cm^{-1}$) and 30,330 cm^{-1}(5980 $M^{-1}cm^{-1}$) start to collapse. This may be due to solubility differences between $[Pt(5,5'–Cl_2–bpy)Cl_2]$ and $[Pt(5,5'–Cl_2–bpy)Cl_2]^{1-}$. Initially $[Pt(5,5'–Cl_2–bpy)Cl_2]$ is made up as a saturated solution in DMF at room temperature. As the temperature is decreased to 233 K $[Pt(5,5'–Cl_2–bpy)Cl_2]$ partially precipitates from the DMF. The reduced anion $[Pt(5,5'–Cl_2–bpy)Cl_2]^{1-}$ is more soluble in DMF and hence on reduction the concentration of the Pt species increases in solution. Oxidation of the anion back to the parent results firstly in the spectrum of $[Pt(5,5'–Cl_2–bpy)Cl_2]^{1-}$ collapsing to that of $[Pt(5,5'–Cl_2–bpy)Cl_2]^0$ and then decreasing in intensity as the neutral species precipitates from the solution.

3.3.2.3. EPR spectroelectrochemistry of $[Pt(5,5'–Cl_2–bpy)Cl_2]^{1-}$.

Reduction of $[Pt(5,5'–(Cl)_2–bpy)Cl_2]$ to its mono–reduced state gives EPR active solutions, see Figure 3.17. The spectrum was best simulated by a coupling of the unpaired electron to the ^{195}Pt (A_{iso} = 63.00 G) nucleus. The solution EPR spectra of $[Pt(5,5'–(Me)_2–bpy)Cl_2]^{1-}$ and $[Pt(5,5'–Cl_2–bpy)Cl_2]^{1-}$ are similar, [38] both showing coupling of the reduction electron to the ^{195}Pt nucleus, (natural abundance 34 %, I = ½). The EPR signal is a broad central line with ^{195}Pt satellites and any superhyperfine coupling of the unpaired electron to ligand nuclei remains unresolved at a range of temperature. However, the contribution of the Pt

nucleus to the SOMO is very small for $[Pt(5,5'–(Me)_2–bpy)Cl_2]^{1-}$ as calculated by Equations 1.1 – 1.3 in Chapter 1. The contribution of the Pt–based orbitals to the SOMO of the mono–reduced 5,5′–$(X)_2$–bpy derivatives is approximately the same as for the 4,4′–derivatives which have been studied by McInnes *et al.*[31] Table 3.7 gives the contribution from Pt based $5d_{yz}$ and $6p_z$ orbitals to the SOMO of the reduced anion. Unfortunately, EPR spectrum of a frozen solution of $[Pt(5,5'–Cl_2–bpy)Cl_2]^{1-}$ could not be recorded due to solubility problems. However, the very similar UV/Vis spectra and solution EPR spectra for the dichloro and dimethyl 5,5′ bpy analogues suggest that the Pt contribution to the SOMO would be of an equivalent size.

X	$[Pt(5,5'-(X)_2-bpy)Cl_2]^{1-}$		
	a^2	b^2	Total Pt
Me	0.060[b]	0.064	0.12
H[a]	0.051[a]	0.075[a]	0.13
CO_2Me	0.038[b]	0.058	0.10
CO_2Et	0.038[b]	0.046	0.08

Table 3.7 Platinum $5d_{yz}$ (a^2) and $6p_z$ (b^2) admixtures to the SOMO of $[Pt(5,5'–(X)_2–bpy)Cl_2]^{1-}$ [a] Values from McInnes *et al.*[36] [b] Values from Jack.[38]

The total Pt contributions to the SOMO are in the range 8 – 13 % and confirm that the reduction electron enters a predominantly ligand–based orbital in each case. The similarity between the EPR spectrum of $[Pt(5,5'–Cl_2–bpy)Cl_2]^{1-}$ and $[Pt(5,5'–Me_2–bpy)Cl_2]^{1-}$,[38] suggest a similar ground state and that the spectra can be

interpreted in a similar fashion. The small shift in g_{iso} from the free electron value, g_e of 2.0023 suggests that the reduction electron is based mainly on the bpy ligand. The reduced anion is therefore best formulated as $[Pt(II)(5,5'–Cl_2–bpy^{-})Cl_2]^{1-}$.

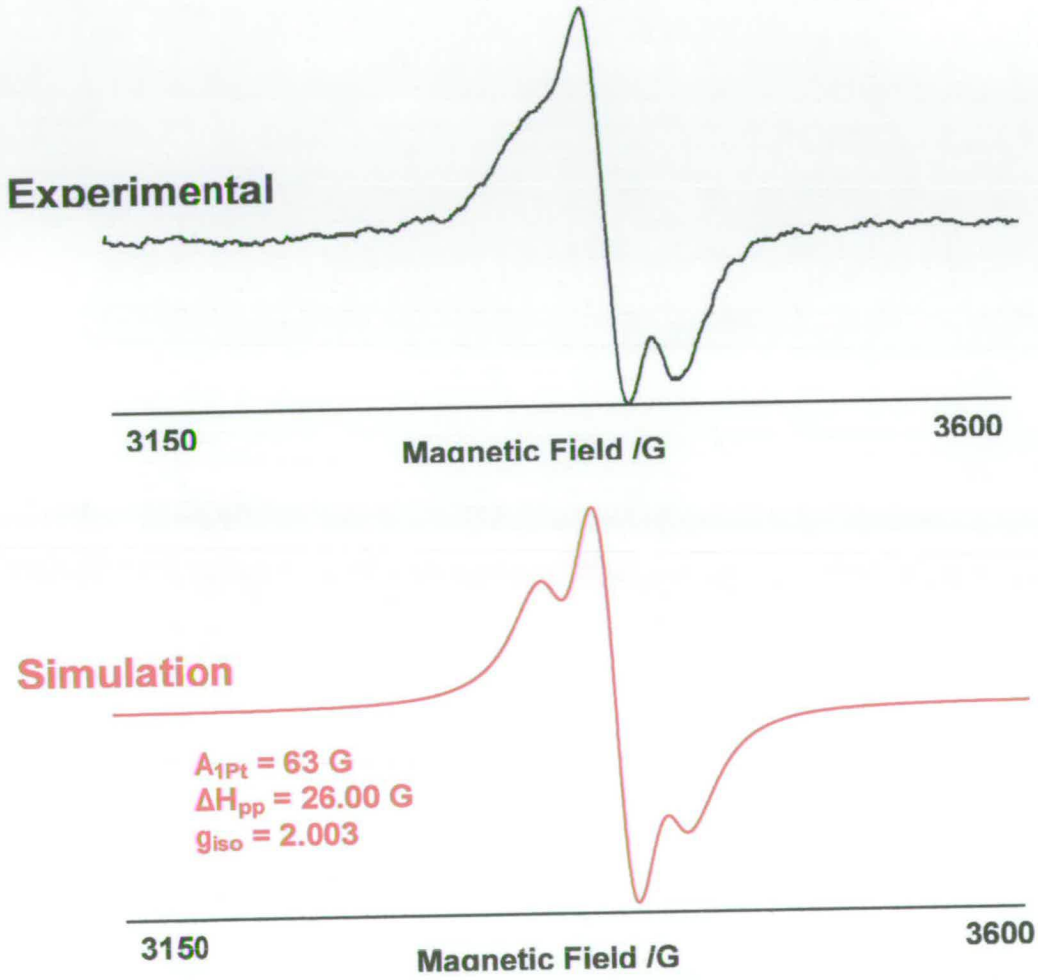

Figure 3.17 Experimental and simulated X–band EPR spectra of $[Pt(5,5'–Cl_2–bpy)Cl_2]^{1-}$ generated *in situ* in 0.1 M [TBA][BF_4]/DMF and E_{gen} = –1.65 V at 253 K.

3.4. Conclusions.

This chapter contains the first electrochemical and spectroelectrochemical study of the mono–chloro–substituted 2,2′–bipyridine pro–ligand (4–Cl–bpy) and the dichloro–substituted 2,2′–bipyridine compounds 5,5′–Cl_2–bpy and 6,6′–Cl_2–bpy alongside their Pt complexes, where synthesised.

5,5′–Cl_2–bpy and 4–Cl–bpy undergo one irreversible reduction in 0.1 M [TBA][BF_4]/DMF at –1.74 V and –1.84 V respectively. In contrast 6,6′–Cl_2–bpy in 0.1 M [TBA][BF_4]/DMF shows one reversible reduction at –1.63 V. The reversibility of the one–electron reduction process of [6,6′–Cl_2–bpy] can be readily influenced by reducing temperature and increasing scan rates. UV/Vis/NIR and the EPR results of 6,6′–Cl_2–bpy indicate that the electron introduced by reduction is delocalised over the two pyridine rings with a only small contribution from the chloro–substituents.

The dichloroplatinum(II) complexes of 5,5′–Cl_2–bpy and 4–Cl–bpy undergo a reversible reduction at –0.83 V and –0.79 V respectively. [Pt(4–Cl–bpy)Cl_2] was not sufficiently stable even at low temperature to allow detailed studied to be carried out.

Spectroelectrochemical studies of [Pt(5,5′–Cl_2–bpy)Cl_2] indicate that the electron reduction is ligand based and the reduction product can be rewritten as [Pt(5,5′–Cl_2–bpy^{1-})Cl_2]$^{1-}$. A dichloroplatinum(II) complex of the 6,6′–Cl_2–bpy ligand

could not be prepared under comparable conditions to those used for the synthesis of the other complexes or under high pressure.

4. Nitro–substituted bipyridines and solvent effects.

4.1. Introduction.

Many reports of nitro–substituted bipyridines, particularly 4,4′–$(NO_2)_2$–bpy and the unsymmetrical 4–NO_2–bpy analogue, have been published.[50,54,55] However, relatively few papers have been published which deal with the electronic behaviour of these ligands and their complexes with transition metals.[50] Wiener *et al.*[56] noted that the electron withdrawing nitro substituents lowered the redox potential necessary for the reduction of the π–system relative to unsubstituted N–hetrocyclic ring compounds in their study of substituted pyridine and 2,2'–bipyridine with NO_2 and $(C_2H_5)_3P$ groups *para* to the ring nitrogens.[56]

X–ray crystallography of 4,4′–$(NO_2)_2$–bpy showed that the molecule is almost planar. The nitro group is slightly displaced from the best plane through the atoms of the pyridine ring and the two pyridine rings are slightly offset.[57] All bond lengths and angles of the py rings and the connecting C–C bond are the same as in 2,2'–bipyridine.[10]

Studies on the series of related complexes [(4,4′–$(X)_2$–bpy)$Ru(CO)_2Cl_2$] (where X = H, Me, ^{t}Bu, NO_2, H_2PO_3, Cl, or Br) showed a trend relating the nature of the substituent and the MLCT transition wavelength exhibited by the species. The electron–donating substituents shifted the absorption maximum of the MLCT transition to lower wavelength while electron–withdrawing substituents had the opposite effect.[84] DFT calculations on

this series showed that the electronic effect of the substituent altered the HOMO–LUMO energies and that [(4,4′–$(NO_2)_2$–bpy)$Ru(CO)_2Cl_2$] has the lowest HOMO–LUMO energy difference and hence the MLCT transition at longest wavelength. [84]

4,4′–$(NO_2)_2$–bpy has been reported to undergo two consecutive one–electron reductions at –0.80 and –0.91 V.[56] It is believed that the nitro group has a strong effect on the electronic properties of the nitro–substituted 2,2'–bipyridine pro–ligands, as Basu and co–workers concluded from resonance Raman vibrational spectra that a considerable portion of the charge transferred in the MLCT excited state for $[Ru(4–NO_2–bpy)_3]^{2+}$ resides on the nitro substituent, *i.e.* that the ligand π^* orbital is localised mainly on the nitro group.[57, 58]

Jack and McInnes[38,31] have studied both 4,4′–$(NO_2)_2$–bpy and 4–(NO_2)–bpy pro–ligands and their respective complexes of Pt(II) and Pd(II). These electrochemistry and spectroelectrochemistry studies indicated that the redox orbital is localised on the NO_2–py moiety of the bpy ligand. The [M(4,4′–$(NO_2)_2$–bpy)Cl_2] compounds, M = Pt(II) or Pd(II), showed that the LUMO→LUMO–1 energy gap is smaller than the spin pairing energy and that the redox orbitals (LUMO and LUMO–1) are localised on singly substituted py rings.

Few references to 4–NO_2–4′–Cl–bpy and 4,4′–NO_2–6,6′–Cl_2–bpy could be found[50,52] in the literature due to the difficulties of making the unsymmetrical bpy in the first case and the difficulties of making the *ortho* substituted bipyridine.

Previous studies by Weaver *et al.*[60,61] showed that the entropy change ΔS^{o}_{rc} of the M(III/II) couple in water is dependent on the nature of the ligand due to the specific interaction of the ligands with surrounding water molecules. Thus, many studies have been focused on the relationship between ΔS^{o}_{rc} and the nature of the solvent.[61–81] Jaworski[82] recorded an important result regarding the solvent effect on the electro–reduction of organic molecules and a linear correlation was observed between ΔS^{o}_{rc} and the acceptor number (AN) of the solvent. Borsari *et al.*[83] have examined the reduction of a number of pyrimidine derivatives. They found that increasing the acceptor number of the solvent also increased the ease of reduction. Given that the acceptor number[100] is a measure of solvent acidity, this can be attributed to greater interaction between the negatively charged reduction product and more acidic solvents.

4.2. Aims of this chapter.

The aims of this chapter are to investigate the electronic properties of the unsymmetrical nitro–substituted bpy compound 4–NO_2–4′–Cl–bpy, and the symmetrical nitro–substituted compound, 4,4′–NO_2–6,6′–Cl_2–bpy. Comparison with the corresponding pyridyl compound, 2–Cl–4–NO_2–py is made. Furthermore, where possible, Pt(II) complexes of these compounds have been synthesized and studied. In this chapter the effects of changing the solvent on the electrochemical properties of 4,4′–$(NO_2)_2$–bpy, 4–NO_2–bpy and 4–NO_2–4′–Cl–bpy and their corresponding Pt(II) complexes have been investigated. The triplet species of $[4,4'–(NO_2)_2–bpy]^{2-}$ has been studied using EPR spectroscopy.

4.3. Results and discussion.

2–Cl–4–NO_2–py was synthesised, following the procedure of Hamana,[51] see section 2.3.5 yielding 80.26% of 2–chloro–4–nitropyridine as light yellow needles. CHN, ^{1}H NMR and mass spectroscopy indicate a successful synthesis has been achieved. 4,4′–Dinitro–2,2′–bipyridine N,N′–dioxide was the starting material for the synthesis of both 4,4′–$(NO_2)_2$–6,6′–Cl_2–bpy and 4–NO_2–4′–Cl –bpy. Good CHN, ^{1}H NMR and mass spectroscopy results have been obtained. Full details are given in Chapter 2, see sections 2.3.6 and 2.3.4.

4.3.1. 4–NO_2–bpy.

4–NO_2–bpy has been studied previously by Jack and therefore will not be discussed in detail here.[38] This study focused on the influence of the solvent on the redox potential values. Murray found that there was a solvent effect on the electrochemical behaviour of 5,5′–$(NO_2)_2$–bpy.[87] Therefore, 4–NO_2–bpy has been investigated in a range of solvents. Cyclic voltammetric study of 4–NO_2–bpy at 293 K in 0.1 M [TBA][BF_4]/DMF solution revealed a fully reversible one–electron reduction at –0.71 V, followed by a second irreversible reduction at a more negative potential –1.62 V. The $E_{½}$ values obtained are presented in Table 4.1.

Solvent [a]	Acceptor Number	$E_{½,1}$ /V
DCM (1)	20.4	-0.68
DMSO (2)	19.3	-0.65
DMF (3)	16.0	-0.71
Py (4)	14.2	-0.74
Acetone (5)	12.5	-0.75
Ethyl Acetate (6)	9.3	-0.76
THF (7)	8.0	-0.78

Table 4.1 The acceptor number of the solvent and the $E_{½}$ value of 4-NO_2-bpy.

(a) Numbers in parentheses correspond to points in Figure 4.1

From the data in Table 4.1, it is apparent that the solvent has a strong effect on the half–wave potential for 4–NO_2–bpy.

Figure 4.1 shows the linear correlation between the $E_{½}$ of the pro–ligand and the acceptor number[100] of the solvent which has been used in this study. A clear trend is observed on going from the lowest acceptor number solvent to the highest acceptor number solvent with the half wave potential value shifting to more positive values.

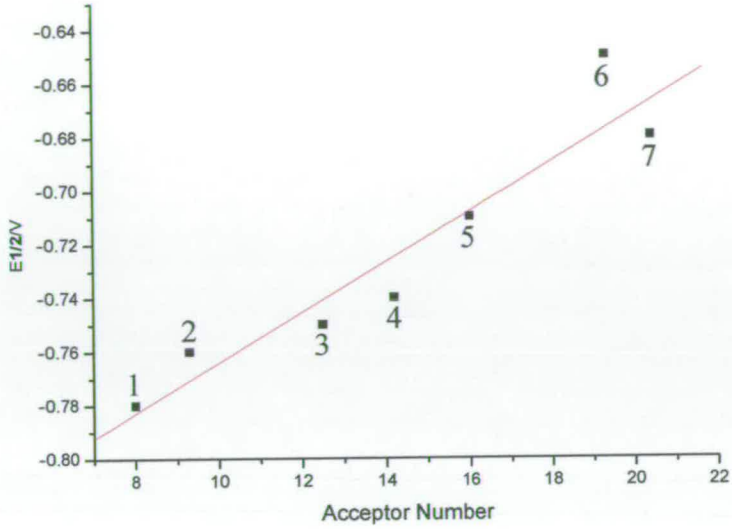

Figure 4.1 The correlation between the acceptor number and the $E_{½}$ value of 4-NO_2-bpy. Values given in Table 4.1.

This trend can be explained by the fact that solvents with higher acceptor numbers are more acidic and therefore stabilise the negative charge of the reduced molecule.[87]

4.3.2. 4,4′–$(NO_2)_2$–bpy.

4.3.2.1. Electrochemistry of 4,4'–$(NO_2)_2$–bpy.

The redox chemistry of 4,4′–$(NO_2)_2$–bpy in 0.1 M [TBA][BF_4]/DMF exhibited two reversible one–electron reductions at –0.65 V and –0.79 V (Figure 4.2). This is in agreement with previous work carried out by Jack.[38] The redox chemistry of 4,4′–$(NO_2)_2$–bpy in different solvents is reported here.

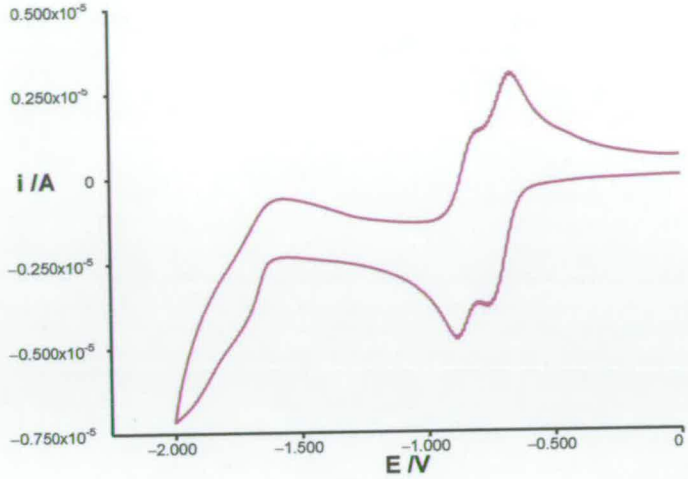

Figure 4.2 Cyclic voltammogram of 4,4′–$(NO_2)_2$–bpy in 0.1 M [TBA][BF_4]/DMF, *vs.* Ag/AgCl, scan rate 0.1 Vs^{-1}, at 293 K.

Since there is a marked redox dependence for 5,5′–$(NO_2)_2$–bpy with solvent,[87] the redox behaviour of 4,4′–$(NO_2)_2$–bpy in different solvents has also been investigated. The 4,4′–$(NO_2)_2$–bpy compound was studied in 0.1 M [TBA][BF_4]/DMF, 0.3 M [TBA][BF_4]/DCM, 0.1 M [TBA][BF_4]/MeCN and 0.1 M [TBA][BF_4]/DMSO. Table 4.2 shows the $E_{½}$ values for 4,4′–$(NO_2)_2$–bpy and the solvent which has been used in each electrochemical study.

Solvent [a]	Acceptor Number100	$E_{½,1}$ /V	$E_{½,1}$ /V
DCM (4)	20.4	-0.65	-0.78
DMSO (3)	19.3	-0.56	-0.70
MeCN (2)	18.9	-0.63	-0.74
DMF (1)	16.0	-0.67	-0.79

Table 4.2 $E_{½}$ values *vs.* Ag/AgCl for 4,4′–$(NO_2)_2$–bpy in various solvents at 298 K.

(a) Numbers in parentheses correspond to the values in Figure 4.3.

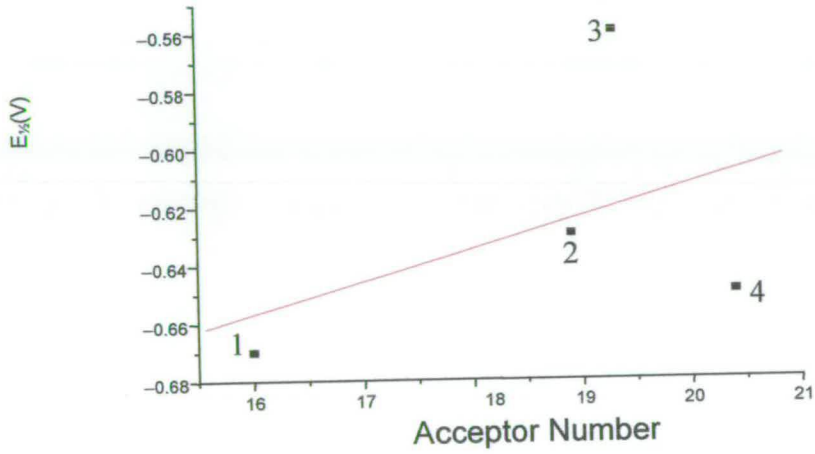

Figure 4.3 Plot of $E_{½}$ vs. acceptor number for 4,4′-$(NO_2)_2$-bpy. Numbers defying solvents are given in Table 4.2.

From Table 4.2 and Figure 4.3, it can be concluded that there is a slight solvent dependence. The lack of solubility of this molecule is a problem and prevented study in a more extensive range of solvents.

4.3.2.2. UV/Vis/nir Spectroelectrochemistry of 4,4′–$(NO_2)_2$–bpy.

In a study of the electronic absorption spectrum of 4,4′–$(NO_2)_2$–bpy in 0.1 M [TBA][BF_4]/DMF, Jack showed the similarities between the spectrum of 4,4′–$(NO_2)_2$–bpy and that of 4–NO_2 –bpy.[38] The close proximity of the two reduction potentials for [4,4′–$(NO_2)_2$–bpy]^0 to [4,4′–$(NO_2)_2$–bpy]$^{1-}$ and [4,4′–$(NO_2)_2$–bpy]$^{1-}$ to [4,4′–$(NO_2)_2$–bpy]$^{2-}$ means that it is not possible to isolate the [4,4′–$(NO_2)_2$–bpy]$^{1-}$ species. Therefore, only the spectrum of [4,4′–$(NO_2)_2$–bpy]$^{2-}$ can be recorded. Before the reduction, high energy peaks were observed at 34,370 cm^{-1} (7470 $M^{-1}cm^{-1}$) and 32,050 cm^{-1} (7511 $M^{-1}cm^{-1}$) which were assigned as $\pi \rightarrow \pi^*$ transitions of the molecule. For [4,4′–$(NO_2)_2$–bpy]$^{2-}$ in 0.1 M [TBA][BF_4]/DMF the band at 20,615 cm^{-1} (10160 $M^{-1}cm^{-1}$) and shoulders at 33,900 cm^{-1} (17950 $M^{-1}cm^{-1}$) and 32,560 cm^{-1} (17820 $M^{-1}cm^{-1}$), see Figure 4.4, were assigned as intraligand transitions to/from the partially filled low–lying π^* orbitals. According to König and Kremer,[85] the spectrum of bpy^{1-} has three sets of absorption bands that are diagnostic for the presence of co–ordinated bpy^{1-}. These are: 1) a nir band at *ca.* 10 kcm^{-1}, comprising of three peaks (or shoulders); 2) a doublet visible band at *ca.* 20 kcm^{-1} and 3) an intense near UV band at *ca.* 25 kcm^{-1}. Furthermore, the spectrum of bpy^{2-} is characterised by a very intense band at *ca.* 26.8 kcm^{-1}. These characteristic bands of bpy^{1-} and bpy^{2-} were not observed in the spectra of [4,4′–$(NO_2)_2$–bpy]$^{2-}$. Thus, it is assumed that the unpaired electrons enter molecular orbitals with a substantial amount of NO_2 character. This is due to the strong electron withdrawing character of the NO_2 substituent. It was deduced from the similarity between

the UV/Vis spectra of $[4,4'–(NO_2)_2–bpy]^{2-}$ and $[4–NO_2–bpy]^{1-}$ and the small separation between E_1 and E_2 of $4,4'–(NO_2)_2–bpy$ that the first unpaired electron enters the LUMO and is localised on one half of the molecule, that is on the $4–NO_2–py$ part of the molecule. The second electron enters an empty orbital close in energy to the LUMO which is LUMO–1. The LUMO and LUMO–1 of $4,4'–(NO_2)_2–bpy$ must have two similar energies since the difference between the half wave potentials is of the order of 140 mV and $[4,4'–(NO_2)_2–bpy]^{2-}$ is paramagnetic.[36] DFT calculations also show that there are two low energy unoccupied molecular orbitals.[78]

$4,4–(NO_2)_2–bpy$ was also examined in 0.3 M [TBA][BF_4]/DCM, see Figure 4.5. The same bands as $4,4–(NO_2)_2–bpy$ in 0.1 M [TBA][BF_4]/DMF were obtained with only a slight difference in the positions, which agrees with cyclic voltammetry results, see Table 4.2. Before reduction of the species, a band was obtained at 31,960 cm^{-1} (8920 $M^{-1}cm^{-1}$) and a high energy band at 42,020 cm^{-1} (35300 $M^{-1}cm^{-1}$), which were assigned as $\pi \rightarrow \pi^*$ internal transitions of the pro–ligand. On generation of the di–reduced product, a peak at 21,280 cm^{-1} (10240 $M^{-1}cm^{-1}$) grew in. The changes in the spectrum as the pro–ligand was reduced are continuously monitored. There was one clear set of isosbestic points observed and hence it must be concluded that either the spectra of the mono– and di–reduced anions are very similar or that the mono reduced species is not stable and immediately disproportionates to the neutral and di–reduced states. X–band EPR results favour the former explanation as the frozen spectrum of $[4,4'–(NO_2)_2–bpy]^{1-}$, at 77 K,

may be simulated for a S = ½ system whereas the $[4,4'–(NO_2)_2–bpy]^{2-}$ requires an S = 1 spin state for successful simulation *vide infra.*

$4,4'–(NO_2)_2–bpy$ was also studied in 0.1 M [TBA][BF_4]/MeCN, see Figure 4.6. In this case, the highest energy bands obtained for the pro–ligand before the reduction were at 47,620 cm^{-1} (33135 $M^{-1}cm^{-1}$), 42,550 cm^{-1} (31945 $M^{-1}cm^{-1}$), 32,450 cm^{-1} (7675 $M^{-1}cm^{-1}$) and 34,470 cm^{-1}(7600 $M^{-1}cm^{-1}$) and were all assigned as $\pi \rightarrow \pi^*$ internal pro–ligand transitions. For $[4,4'–(NO_2)_2–bpy]^{2-}$ peaks were observed at 21,330 cm^{-1} (6400 $M^{-1}cm^{-1}$), 31,260 cm^{-1}(18840 $M^{-1}cm^{-1}$) and 38,770 cm^{-1} (27230 $M^{-1}cm^{-1}$). Thus, the well defined absorption in the visible region of the spectrum of di–reduced $[4,4'–(NO_2)_2–bpy]^{2-}$ appears to have a slight solvent dependence. However, unlike the redox potential values, the energy of the visible band did not appear to vary linearly with solvent acceptor number, see Figures 4.4–4.6. Further experiments should be undertaken in different solvents with different concentrations of electrolyte to explore this further. Unfortunately, the lack of solubility of this compound will be a problem for any extensive studies.

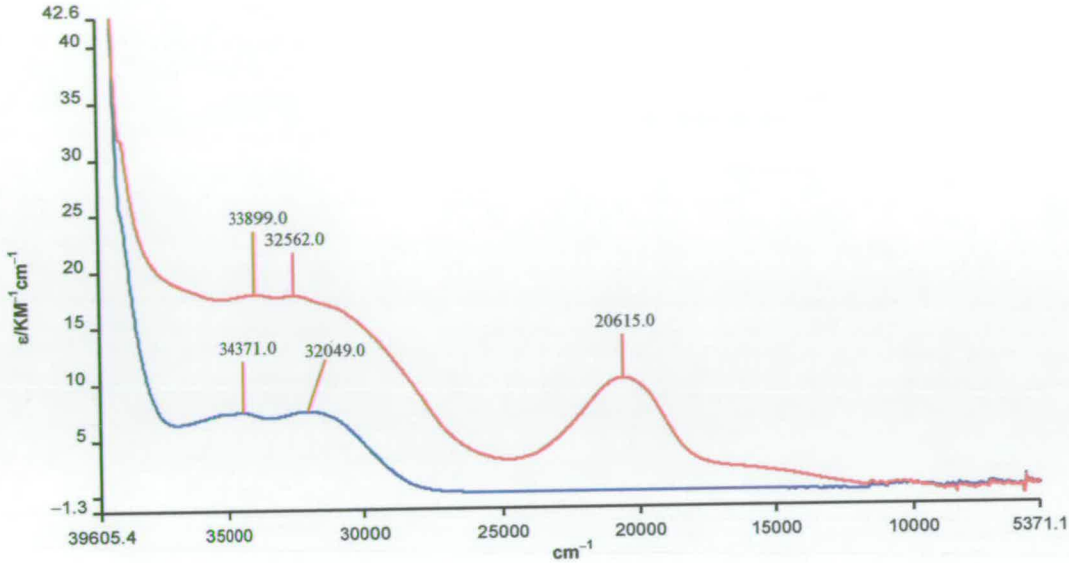

Figure 4.4 UV/Vis/nir absorption spectra of 4,4′–$(NO_2)_2$–bpy (blue) and $[4,4'–(NO_2)_2–bpy]^{2-}$ (red) in 0.1M $[TBA][BF_4]$/DMF at 233 K.

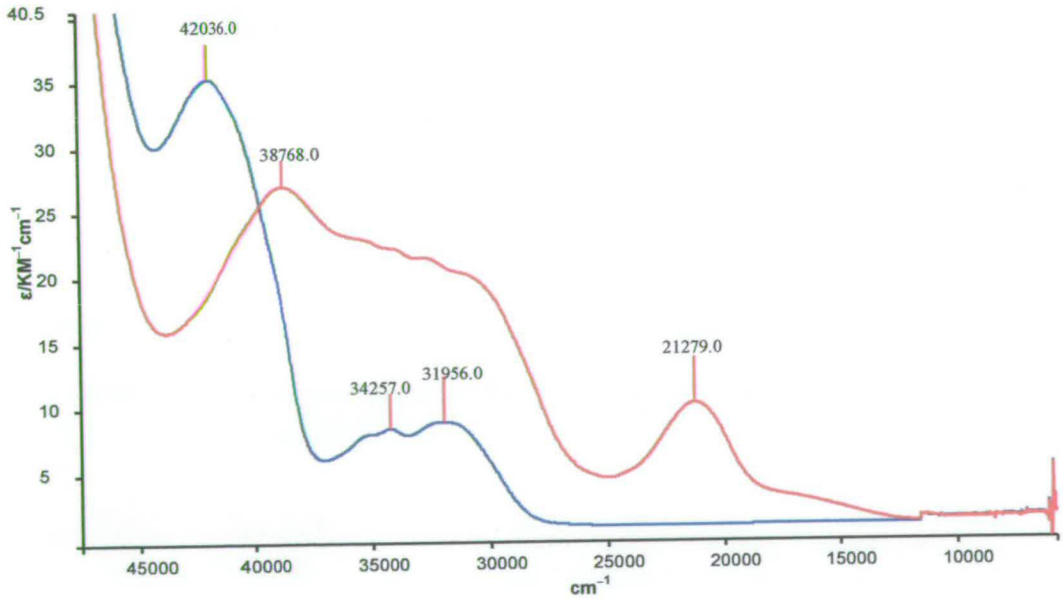

Figure 4.5 UV/Vis/nir absorption spectra of 4,4′–$(NO_2)_2$–bpy (blue) and $[4,4'–(NO_2)_2–bpy]^{2-}$ (red) in 0.3 M $[TBA][BF_4]$/DCM at 233 K.

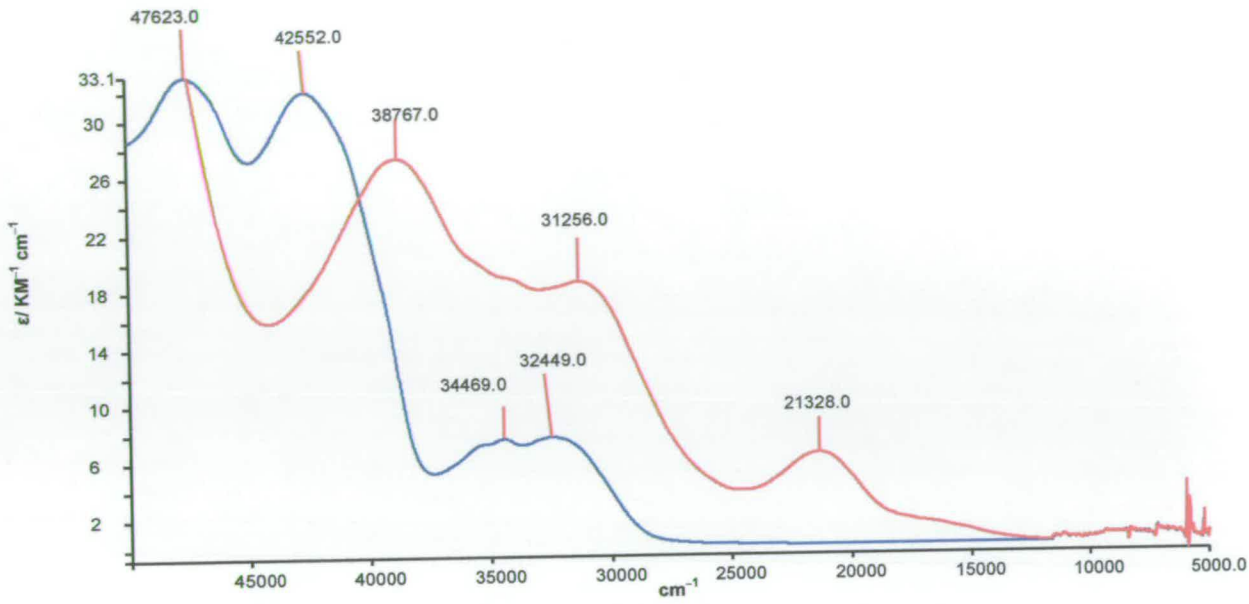

Figure 4.6 UV/Vis/nir absorption spectra of 4,4′–$(NO_2)_2$–bpy (blue) and $[4,4'–(NO_2)_2–bpy]^{2–}$ (red) in 0.1 M $[TBA][BF_4]$/MeCN at 233K.

4.3.2.3. EPR Spectroelectrochemistry of $[4,4'–(NO_2)_2–bpy]^{2–}$.

The parent compound 4,4′–$(NO_2)_2$–bpy was EPR silent as expected. The di–reduced species was EPR active and was a spin triplet. Thus, [4,4′–$(NO_2)_2$–bpy] must have two π* anti–bonding orbitals close in energy which are both singly populated in $[4,4'–(NO_2)_2–bpy]^{2–}$.

The X–band EPR spectra of $[4,4'–(NO_2)_2–bpy]^{2–}$ revealed a significant solvent dependence. The solution X–band EPR spectrum of $[4,4'–(NO_2)_2–bpy]^{2–}$ generated *in situ* at –1.5 V *vs.* Ag/AgCl, at 233 K in 0.1M $[TBA][BF_4]$/MeCN was similar to that

obtained in 0.3 M [TBA][BF_4]/DCM, giving an 11 line EPR signal see Figure 4.7 and 4.8. The X–band EPR spectrum of [4,4′–$(NO_2)_2$–bpy]$^{2-}$ can be successfully simulated by assuming coupling of the unpaired electron to two inequivalent N nuclei (7.95 G and 2.9 G) and to an equivalent pair of H nuclei (2.55 G), with a Lorentzian linewidth of 0.9 G. Note that the best simulation, *i.e.* the one which correlates best with the experimental result requires localization of the unpaired electron on only one NO_2–py fragment. This may arise from the two py rings being in a staggered arrangement along the C2–C2′ bond. The X–band EPR spectrum of [4,4′–$(NO_2)_2$–bpy]$^{2-}$ in 0.1 M [TBA][BF_4]/DMF was more resolved than in other solvents (*e.g.* MeCN, DCM) see Figure 4.9.

The X–band EPR spectrum of [4,4′–$(NO_2)_2$–bpy]$^{2-}$ species in 0.1M [TBA][BF_4]/DMF was best simulated with the molecular orbital containing an unpaired electron based on one 4–NO_2–py moiety, with coupling to two nitrogen (6.770 G and 2.700 G) and three hydrogen (3.25, 2.99 and 0.20 G) nuclei (Figure 4.9). The smallest hydrogen coupling is assigned to the hydrogen next to the pyridine N atom based on the study of 4,4′–$(NO_2)_2$–6,6′–Cl_2–bpy, discussed later in this chapter, and on the results of DFT calculations.[87] The largest H couplings were assigned to the *meta* hydrogens on either side of the NO_2 substituient on the py ring. No attempt has been made to further assign couplings to specific H nuclei. Work done by Murray[87] on the 4–$^{15}NO_2$–bpy and 4–$^{14}NO_2$–bpy concluded that the largest electron density on the singly reduced pro–ligand is on the NO_2 group, thus, it is possible to assign the N couplings. The largest nitrogen coupling is assigned to the nitro group nitrogen and the smaller N coupling is assigned to the py ring nitrogen. From the results obtained by the EPR study it would

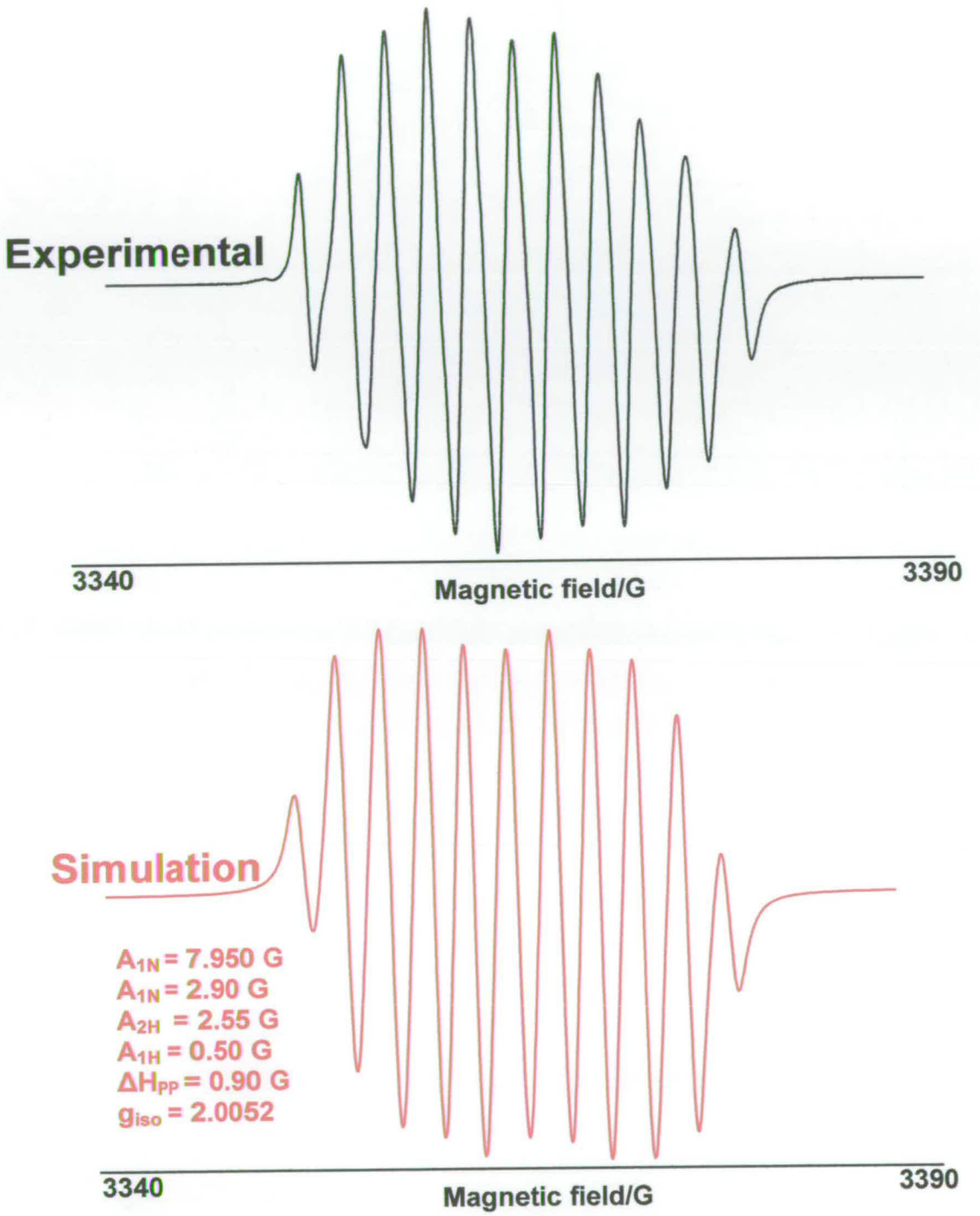

Figure 4.8 Experimental and simulated X–band EPR spectra of $[4,4'–(NO_2)_2–bpy]^{2-}$ generated *in situ* at –1.2 V vs. Ag/AgCl, 233 K in 0.3 M [TBA][BF_4]/DCM.

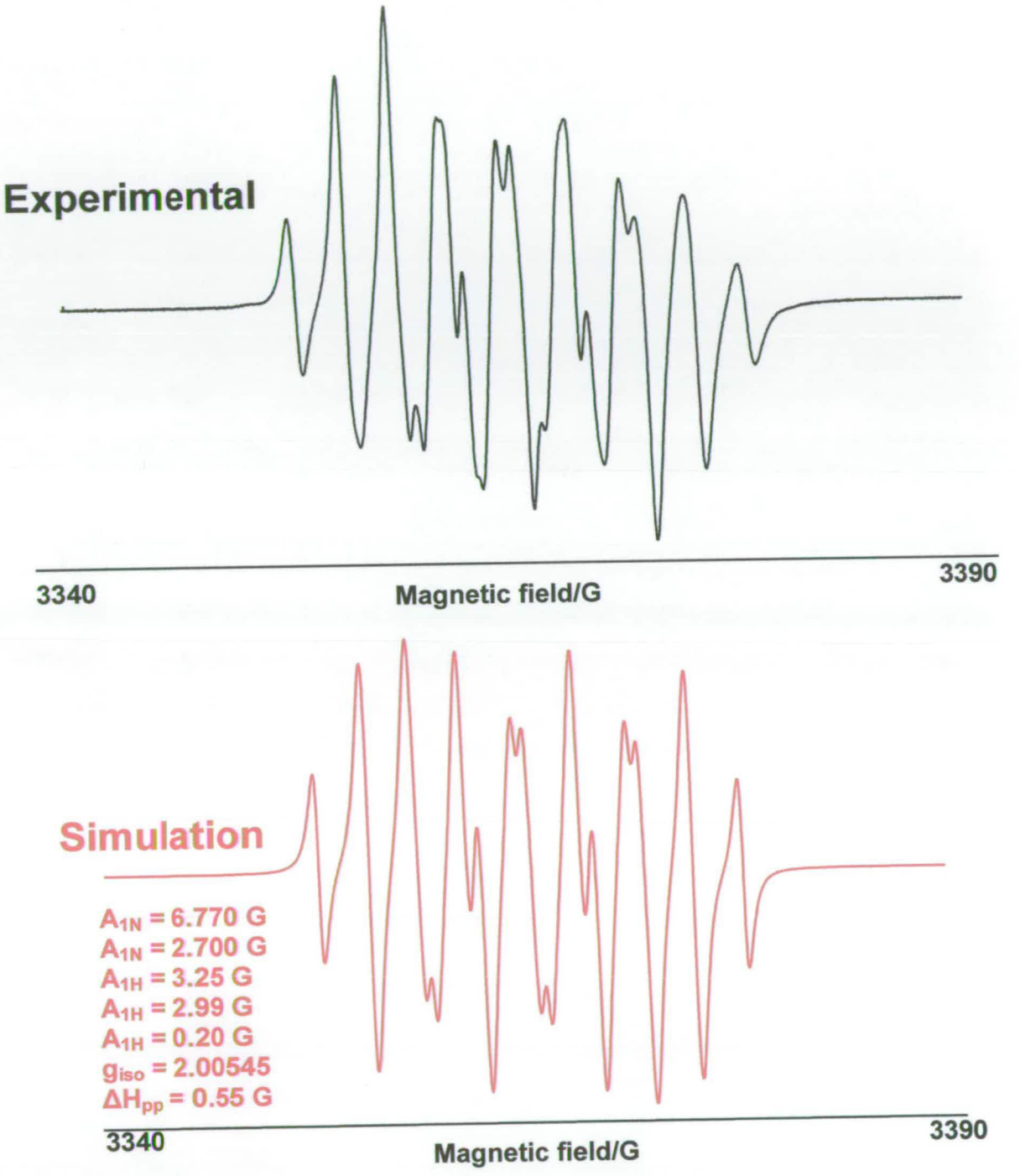

Figure 4.9 Experimental and simulated X–band EPR spectra of $[4,4'–(NO_2)_2–bpy]^{2-}$ generated *in situ* at –1.2V vs. Ag/AgCl, at 233 K in 0.1 M [TBA][BF_4]/DMF.

The lack of resolution on the X–band EPR spectrum of $[4,4'–(NO_2)_2–bpy]^{2-}$ in DCM and MeCN can be attributed to the solvent dependence, rather than an electron hopping mechanism as it was reported by Jack,[38] as the X–band EPR spectrum of $[4,4'–(NO_2)_2–bpy]^{2-}$ was more resolved in DMF solution than it was obtained in DCM and MeCN solutions. DCM and MeCN will interact more strongly with the reduced dianion $[4,4'–(NO_2)_2–bpy]^{2-}$ than DMF, as expected from their higher acceptor numbers and the increased solvent interaction will lead to a less resolved X–band EPR spectrum due to less efficient tumbling of the larger extended system.

The electrogeneration of $[4,4'–(NO_2)_2–bpy]^{2-}$ results in changes in intensity of the UV/Vis/nir and EPR bands. However, there are only features observed which are assigned to either the neutral starting material or the di–reduced anion. Therefore, either the mono–reduced species has a spectrum similar to that of the di–reduced material or the mono–reduced material immediately disproportionates to the neutral and di–reduced species and is thus not observable. However, frozen X–band EPR spectra of reduced $4,4'–(NO_2)_2–bpy$ in DCM allowed a distinction to be made between $[4,4'–(NO_2)_2–bpy]^{1-}$ and $[4,4'–(NO_2)_2–bpy]^{2-}$, see Figure 4.10.

The black spectrum in Figure 4.10 is the frozen spectrum recorded early in the electrogeneration process whereas the red spectrum is the frozen spectrum recorded after electrogeneration at –1.2 V at 233 K for six hours and then the temperature of the cell was decreased to 153 K. The black spectrum has been scaled to fit the maximum of the red spectrum. The central signal in the red spectrum and the black spectrum was

attributed to $[4,4'-(NO_2)_2-bpy]^{1-}$. It has proved impossible to date to generate a frozen EPR spectrum of $[4,4'-(NO_2)_2-bpy]^{2-}$ alone. The central mono–reduced signal is always present. This is in part because of the way the EPR spectroelectrochemical experiment is set up. The electro–generation potential is applied to the gauze electrode with the connection above the gauze shielded from the solution not in the flat part of the cell. When the temperature is decreased in order to record the frozen EPR signal the solvent will contract and unreduced solution will be pulled into the flat portion of the cell thereby generating mono–reduced material. It was attempted to generated the di–reduced species chemically using an excess of $Na[BH_4]$ but this led to an unresolved EPR spectrum presumably due to ion pairing of the reduced pro–ligand with Na^+ ions.

Figure 4.11 shows the EPR spectrum which results from subtraction of the black spectrum from the red spectrum in Figure 4.10 and is primarily that of $[4,4'-(NO_2)_2-bpy]^{2-}$. The central feature in Figure 4.11 results from a slight mismatch of the intensities of the two spectra. Interpretation of the EPR spectrum in Figure 4.11 will now be attempted.

Figure 4.12 shows four EPR spectra. The top black trace is the difference spectrum as shown in Figure 4.11. The red spectrum is that for an axial spin triplet with the zero field splitting parameter D = 0.0080 cm^{-1} which is set by the position of the two outermost features and $g_z = 2.017$, $g_x = g_y = 2.016$ and an isotropic Gaussian linewidth of 10 G. The splitting of the z component is equal to 2D whereas the x,y features will be separated by

D in an axial spectrum. Clearly the simulation is of the correct shape but the positions of the x,y features do not match those predicted for an axial spectrum.

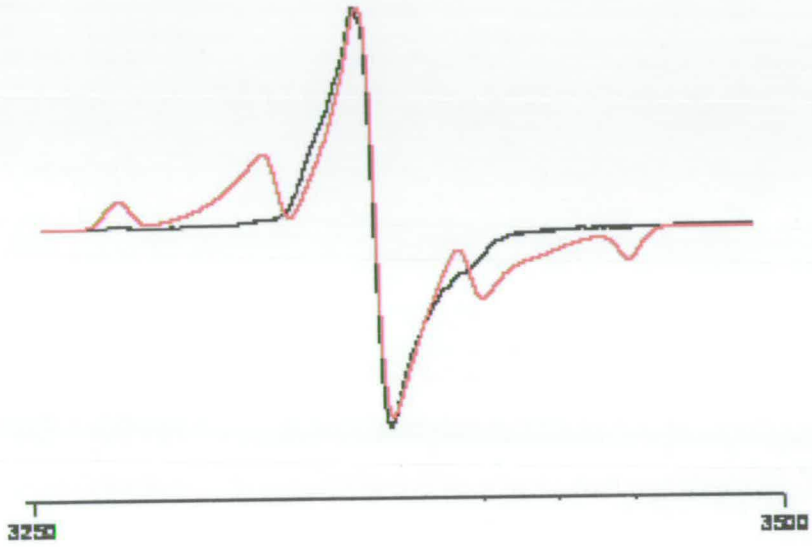

Figure 4.10 Overlay of scaled X–band EPR spectra of the mono–and di–reduced species of 4,4′–$(NO_2)_2$–bpy in 0.3 [TBA][BF_4]/DCM, at 153 K.

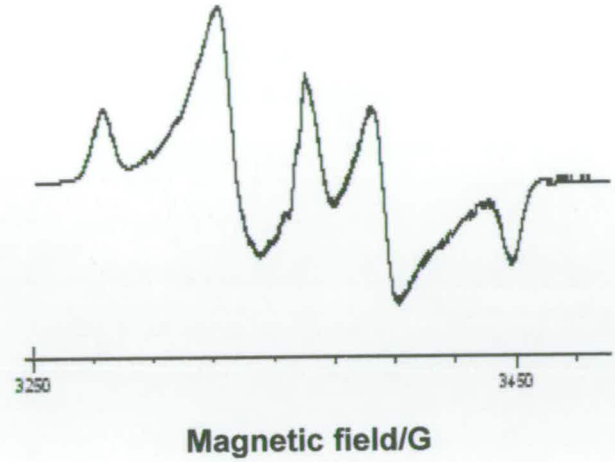

Figure 4.11 The X-band EPR spectrum $[4,4'\text{-}(NO_2)_2\text{-bpy}]^{2-}$ as a result from subtraction of the black and red spectrum in Figure 4.10.

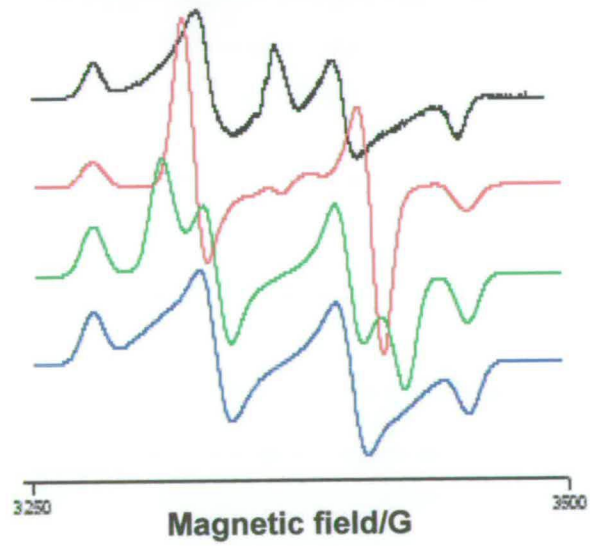

Figure 4.12 Difference spectrum (black) is essentially that of frozen $[4,4'\text{–}(NO_2)_2\text{–bpy}]^{2-}$ in 0.3 [TBA][BF_4]/DCM and three simulations.

The green spectrum in Figure 4.12 is the simulated spectrum for a rhombic signal with D = 0.008 cm^{-1} and λ = E/D =0.1 where E = rhombic zero–field splitting parameter. All other parameters are the same as in the red spectrum, *i.e.* relaxing the system from axial to rhombic has the effect of moving the x components of the perpendicular part of the axial spectrum inwards while pushing the y features outwards to meet z. The green spectrum shows a good fit for the positions and shapes of the x and z features to the experimental spectrum (black). However, the experimental spectrum shows no sign of the y features. The final blue spectrum uses the same parameters in the simulation as the green spectrum but with linewidth W_y = 50 G and $W_z = W_x$ = 10 G. The blue spectrum agrees well with the black (experimental) spectrum but there is no obvious reason why there should be a huge linewidth on y.

The black spectrum in Figure 4.13 is the difference spectrum of $[4,4'–(NO_2)_2–bpy]^{2-}$. The red spectrum uses the same parameters as those previously for the blue spectrum apart from the following changes: W_y = 9 G, $W_x = W_z$ = 6 G, A^N_y = 15 G, $A_z^N = A_x^N$ = 1 G. The simulation now includes a hyperfine coupling to the N nuclei of the nitro groups and gives a good fit to the experiment. A previous study[101] of the radical anion of nitrobenzene measured $A^N_{\parallel}$ = 30 G and $A^N_{\perp}$ = 7 G where the unique axis is normal to the plane of the molecule. In the case of $[4,4'–(NO_2)_2–bpy]^{2-}$ the two electrons are exchanging (as witnessed by the triplet spectrum) and hence each electron only sees each N for half the time, hence coupling to two nitrogen nuclei with half the magnitude; A^N = 15 G. The anisotropic hyperfine coupling values should average to the solution value of around 7 G. The z axis in the molecule will contain the NO_2 substituent with the x–axis

also in the plane of the molecule and the y axis is therefore orthogonal to the molecular plane. The orbital occupied by the unpaired electron is expected to have p–character and thus $A^N y$ is indeed expected to be significantly greater than $A^N z$ or $A^N x$.

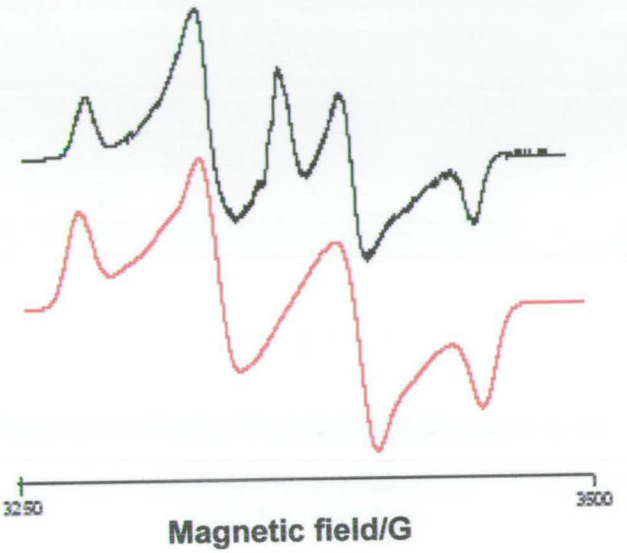

Figure 4.13 The difference X-band EPR spectrum of $[4,4'\text{-}(NO_2)_2\text{-bpy}]^{2-}$ (black) and the simulated spectrum (red).

The final piece of evidence that the di–reduced species is a spin triplet system is the experimental observation of a half field signal at 1700 G, corresponding to the $\Delta ms = \pm 2$ transition. The signal is very small as seen in Figure 4.14. This signal is not observed in the mono–reduced spectrum of $[4,4'\text{–}(NO_2)_2\text{–bpy}]^{1-}$.

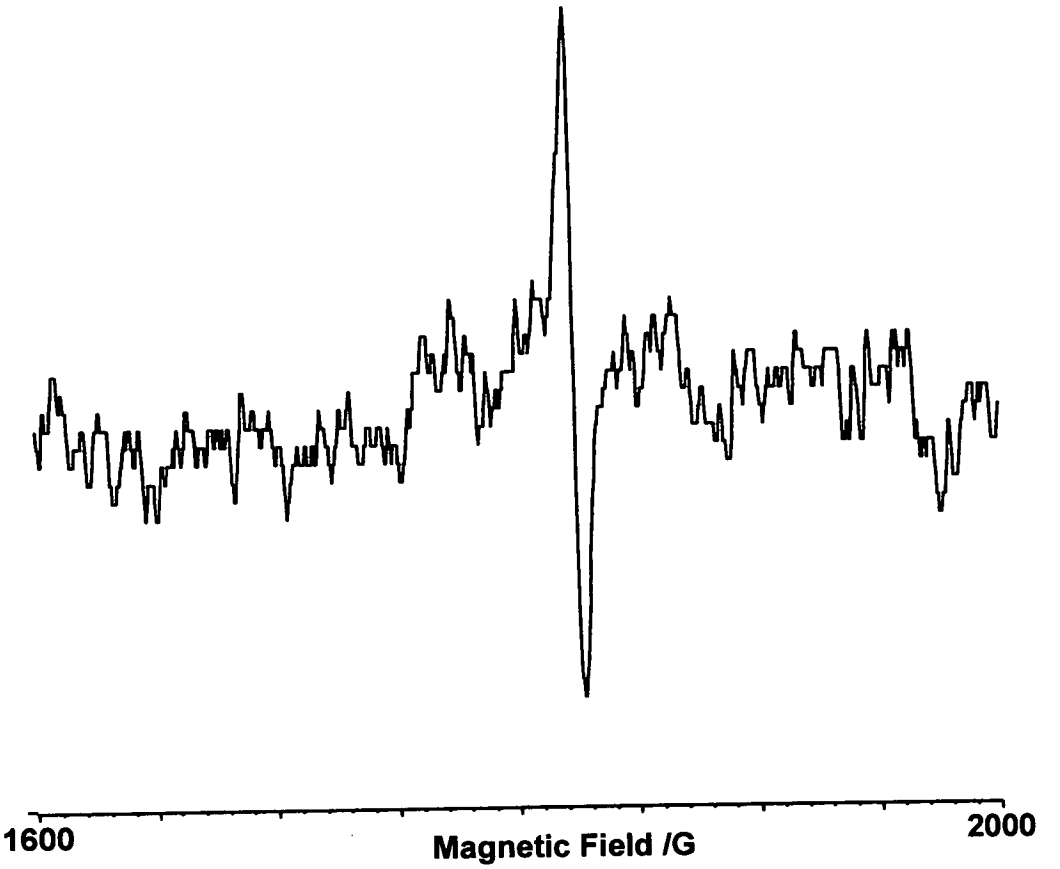

Figure 4.14 Half X–band field EPR signal observed for frozen $[4,4'–(NO_2)_2–bpy]^{2-}$ in 0.3 M [TBA][BF_4]/ DCM.

4.3.3. $4,4'–(NO_2)_2–6,6'–Cl_2–bpy$.

4.3.3.1. Electrochemistry of $4,4'–(NO_2)_2–6,6'–Cl_2–bpy$.

The cyclic voltammetric studies of $4,4'–(NO_2)_2–6,6'–Cl_2–bpy$ at 293 K in 0.1 M [TBA][BF_4]/DMF solution showed two reversible reductions at –0.48 V and –0.59 V and a third irreversible process at –1.51 V, as shown in Figure 4.15. It was reported by McInnes,[31] that the small separation between E_1 and E_2 in $[4,4'–(NO_2)_2–bpy]$ is

inconsistent with spin pairing of the two added electrons in the same π* orbital. The reduction potentials for 4,4′–$(NO_2)_2$–6,6′–Cl_2–bpy are more positive than 4,4′–$(NO_2)_2$–bpy which is as expected for replacement of H by electron withdrawing Cl groups.

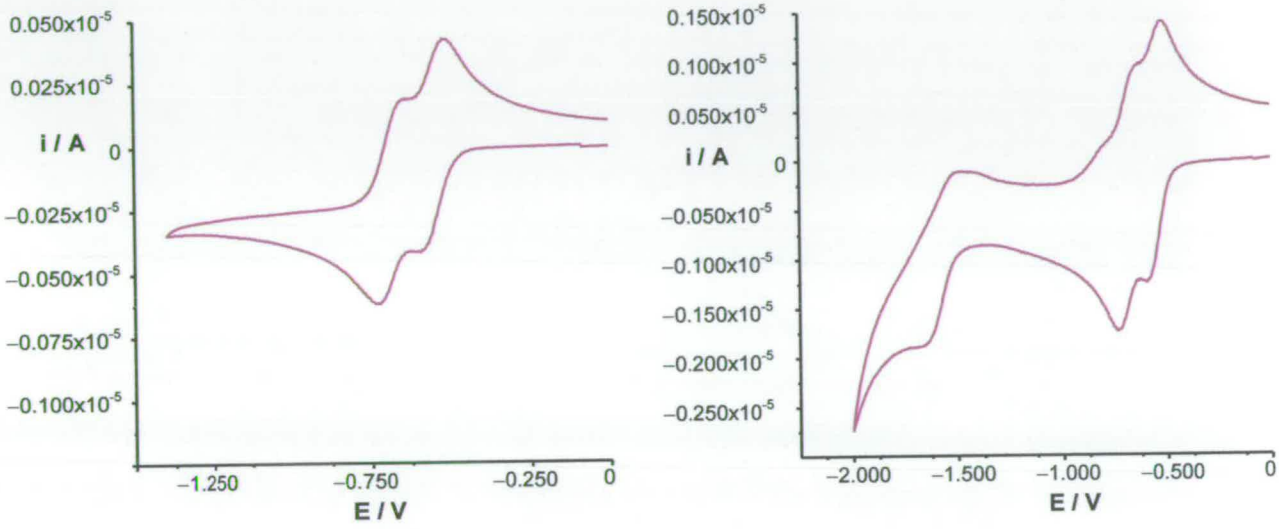

Figure 4.15 Cyclic voltammograms of 4,4′-$(NO_2)_2$-6,6′-Cl_2-bpy in 0.1 M [TBA][BF_4]/DMF , vs. Ag/AgCl, at 293 K, scan rate 0.1 Vs^{-1}.

4.3.3.2. UV/Vis/nir spectroelectrochemistry of 4,4′–$(NO_2)_2$–6,6′–Cl_2–bpy.

The UV/Vis/nir spectrum obtained for $[4,4'–(NO_2)_2–6,6'–Cl_2–bpy]^{2-}$ (Figure 4.16) was similar to the corresponding spectrum of $[4,4'–(NO_2)_2–bpy]^{2-}$. It was impossible to isolate the mono–reduced species $[4,4'–(NO_2)_2–6,6'–Cl_2–bpy]^{1-}$ as a result of the two reduction potentials for $[4,4'–(NO_2)_2–6,6'–Cl_2–bpy]^{0}$ to $[4,4'–(NO_2)_2–6,6'–Cl_2–bpy]^{1-}$ and $[4,4'–(NO_2)_2–6,6'–Cl_2–bpy]^{1-}$ to $[4,4'–(NO_2)_2–6,6'–Cl_2–bpy]^{2-}$ being close

together. A high energy band is observed at 30,390 cm^{-1} (19120 $M^{-1}cm^{-1}$) in the neutral species, [4,4′–$(NO_2)_2$–6,6′–Cl_2–bpy] which was assigned as a $\pi \rightarrow \pi^*$ transition of the molecule. For $[4,4'–(NO_2)_2–6,6'–Cl_2–bpy]^{2-}$ an intense band at 32,347 cm^{-1} (27180 $M^{-1}cm^{-1}$) with a shoulder at lower energy 30,390 cm^{-1} (ε = 27450 $M^{-1}cm^{-1}$) and a band at 20,400 cm^{-1} (ε = 18840 $M^{-1}cm^{-1}$) grew in. A broad band in the visible region at 15,000 cm^{-1} (ε = 65970 $M^{-1}cm^{-1}$) was also observed. These peaks were all assigned as $\pi \rightarrow \pi^*$ intramolecular transitions of the reduced molecule. The bands observed did not demonstrate the characteristic peaks attributed to the bpy^{1-} or bpy^{2-} species as discussed previously, therefore, it is likely that the unpaired electron enters a molecular orbital with a substantial amount of a NO_2 character hence the similarities with the spectrum of $[4,4'–(NO_2)_2–bpy]^{2-}$.

The small potential separation of 110 mV between the two reductions and the similarity of the spectra of $[4,4'–(NO_2)_2–6,6'–Cl_2–bpy]^{2-}$ and $[4–NO_2–bpy]^{1-}$ are evidence that the second electron reduction of $[4,4'–(NO_2)_2–6,6'–Cl_2–bpy]^{2-}$ enters an empty orbital close to energy to the LUMO.

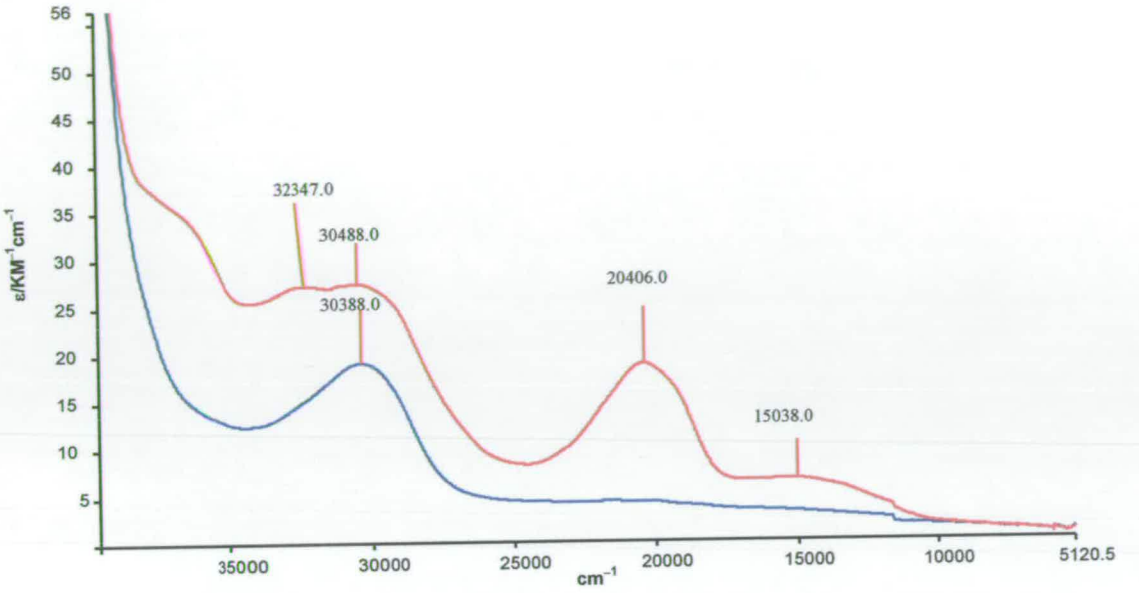

Figure 4.16 UV/Vis/nir absorption spectra of 4,4′–$(NO_2)_2$–6,6′–Cl_2–bpy (blue) and $[4,4'–(NO_2)_2–6,6'–Cl_2bpy]^{2-}$ (red) in 0.1 M [TBA][BF_4]/DMF at 233 K.

4.3.3.3. EPR Spectroelectrochemistry of $[4,4'–(NO_2)_2–6,6'–Cl_2–bpy]^{2-}$.

In situ electrochemical reduction of 4,4′–$(NO_2)_2$–6,6′–Cl_2–bpy in 0.1 M [TBA][BF_4]/DMF yielded the EPR active di–reduced species, the basic structure of which has 9 lines, see Figure 4.17. The experimental X–band EPR spectrum of $[4,4'–(NO_2)_2–6,6'–Cl_2–bpy]^{2-}$ can be successfully simulated with coupling to two N nuclei (6.650 G and 2.552 G), two H nuclei (3.325 G and 2.552 G) and a small coupling to chloride (0.290 G). On consideration of the compound 4,4′–$(NO_2)_2$–6,6′–Cl_2–bpy, this would suggest that each of the unpaired electrons must occupy a molecular orbital based on different aromatic rings with only minor interaction between them. The unpaired

electron is coupling to all the EPR active nuclei present on the ring, namely the N nuclei from the NO_2 group and pyridine N, the two unique protons in the 3 and 5 positions and the Cl in the 6 position. Once again the EPR data indicated that the unpaired electron is localized on only one substituted py ring. The hyperfine couplings of $[4,4'–(NO_2)_2–bpy]^{2-}$ given in Figure 4.9 and that of $[4,4'–(NO_2)_2–6,6'–Cl_2–bpy]^{2-}$, see Figure 4.17 are similar and hence the LUMOs of both of the compounds have similar electronic properties. The coupling to the chloro substituent is small but necessary to fit the observed shape of the outermost lines and indicates that the 6 position on the py ring gives only a minor contribution to the semi–occupied MO. This result suggests that the protons in the 6,6′–position in $[4,4'–(NO_2)_2–bpy]^{2-}$ should also have a small effect as assigned previously.

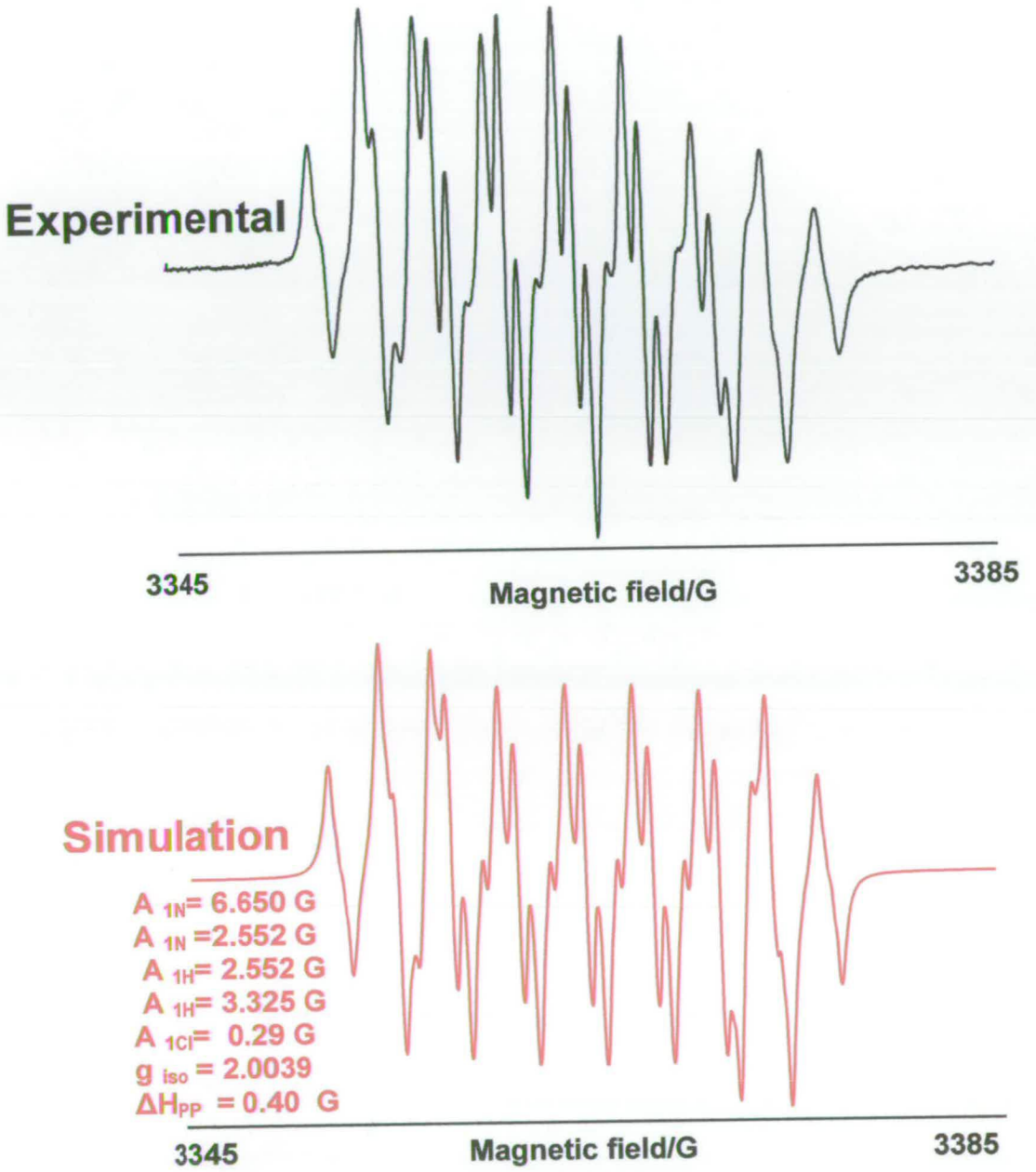

Figure 4.17 Experimental and simulated X–band EPR spectra of $[4,4'–(NO_2)_2–6,6'–Cl_2–bpy]^{2-}$ generated *in situ* in 0.1 M [TBA][BF_4]/DMF, E_{gen} = –1.40 V, vs. Ag/AgCl, 233 K.

4.3.4. 4–NO_2–4′–Cl–bpy.

Although the syntheses of many di– and poly–substituted 2,2′–bipyridyls and their 1–oxides have been reported, there are few examples of mono–substituted compounds.[50,86] A review of the literature revealed just one paper regarding the synthesis of an unsymmetrical 4–nitro–4′–chloro–bipyridine. Therefore, it was interesting to investigate the electronic effect of another unsymmetrical bipyridine replacing the hydrogen on the other ring with a different substituent such as chlorine.

One paper has been published on the synthesis of the 4–NO_2–4′–Cl–bpy[50] which was successfully employed here, see section 2.3.4. These sections below report on the electro– and spectroelectrochemical studies of this compound.

4.3.4.1. Electrochemistry of 4–NO_2–4′–Cl–bpy.

4–NO_2–4′–Cl–bpy in 0.1 M [TBA][BF_4]/DMF gave a fully reversible reduction at –0.68 V, see Figure 4.18. Reinvestigation of electrochemistry of 4–NO_2–bpy has been done alongside a solvent dependence study for comparative purposes. 4–NO_2–bpy revealed one reversible reduction at –0.72V, followed by an irreversible reduction at –1.92 V.

The reduction potential of 4–NO_2–4′–Cl–bpy is slightly shifted to a more positive potential value compared with 4–NO_2–bpy, which correlates with the chloro–substitutent behaving as a more electron withdrawing group than hydrogen.

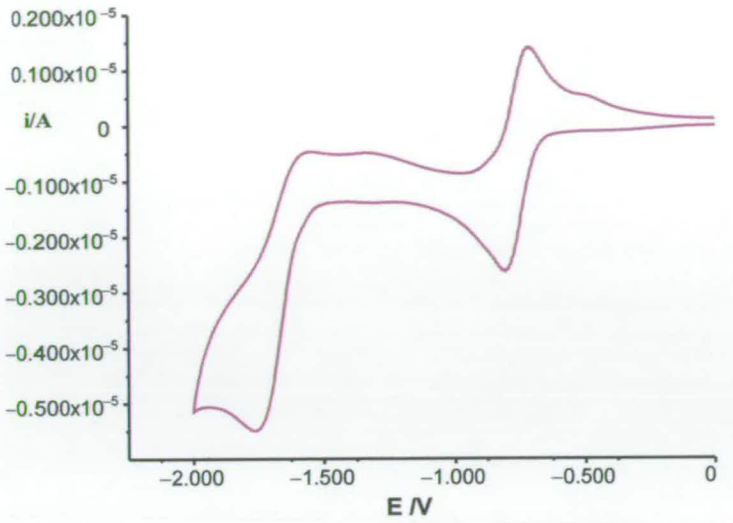

Figure 4.18 Cyclic voltammogram of 4-NO_2-4′-Cl-bpy in 0.1 M [TBA][BF_4]/DMF, vs. Ag/AgCl, at 293 K, scan rate 0.1 V s^{-1}.

4–NO_2–4′–Cl–bpy was examined in a range of solvents in order to examine whether there was a solvent effect. A trend has been observed for NO_2 containing molecules regarding the acceptor number of the solvents and the redox potential of the compound; the smaller the acceptor number, the more negative the reduction potential, see Table 4.3. The electrochemistry of 4–NO_2–4′–Cl–bpy has been studied in 0.1 M [TBA][BF_4]/DMF, 0.3 M [TBA][BF_4]/DCM, 0.1 M [TBA][BF_4]/MeCN, 0.2 M [TBA][BF_4]/acetone, 0.3 M [TBA][BF_4]/THF, 0.3 M [TBA][BF_4]/ethyl acetate and 0.1 M [TBA][BF_4]/DMSO. The results are shown in Table 4.3 and are plotted in Figure 4.19.

Solvent [a]	Acceptor Number100	$E_{½,1}$ /V
DCM (1)	20.4	-0.6
DMSO (2)	19.3	-0.62
DMF (3)	16.0	-0.67
Py (4)	14.2	-0.68
Acetone (5)	12.5	-0.75
Ethyl Acetate (6)	9.3	-0.73
THF (7)	8.0	-0.70

Table 4.3 $E_{½}$ values of 4-NO_2-4′-Cl-bpy vs.Ag/AgCl, in various solvents at 293 K.

(a) Number in parentheses correspond to values in Figure 4.19.

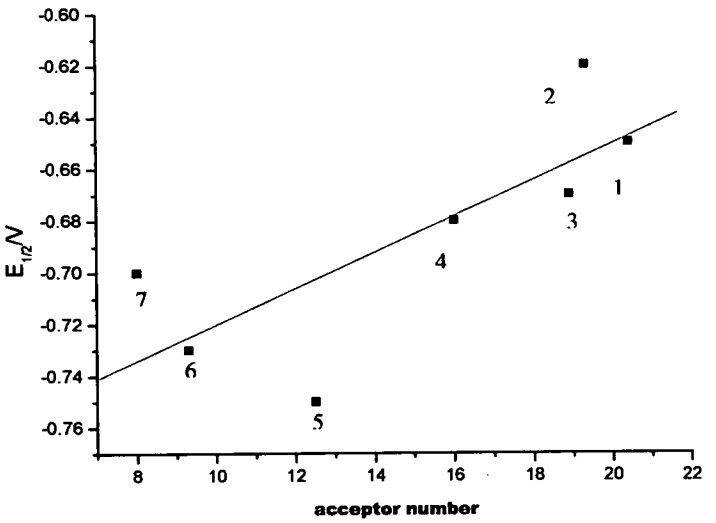

Figure 4.19 Plot of $E_{½}$ *vs.* acceptor number for 4–NO_2–4′–Cl–bpy. Solvent numbers given in Table 4.3.

From the data presented in Table 4.3 and Figure 4.19 there is a significant shift of the reduction potential of 4–NO_2–4′–Cl–bpy in different solvents. The linear correlation is not as good as for other NO_2–containing pro–ligands, see Figure 4.1, but the observation that the higher the acceptor number of the solvent the easier the molecule is reduced still holds. Solvents with higher acceptor numbers are more acidic and will therefore surround and solvate the negatively charged moiety of a reduced molecule, thus stabilising the reduced species, which leads to a positive shift in the half–wave potential.

4.3.4.2. UV/Vis/nir Spectroelectrochemistry of 4–NO_2–4′–Cl–bpy.

The OTTLE spectrum of the neutral species of 4–NO_2–4′–Cl–bpy in 0.1 M [TBA][BF_4]/DMF showed an intense band at high energy at 35,500 cm^{-1} (ε = 10,400 $M^{-1}cm^{-1}$) and a broad band at *ca.* 31,000 cm^{-1} (ε = 3,000 $M^{-1}cm^{-1}$), see Figure 4.20. On reduction of 4–NO_2–4′–Cl–bpy to [4–NO_2–4′–Cl–bpy]$^{1-}$ intense bands at 35,000 cm^{-1} (ε = 15,400 $M^{-1}cm^{-1}$), with a broad shoulder at lower energy and 20,400 cm^{-1} (ε = 3,9000 $M^{-1}cm^{-1}$) grew in. A broad band in the visible region at 15,000 cm^{-1} was also observed. The spectrum of the reduced anion was very similar to other reduced compounds containing the NO_2 group, see Figures 4.4 and 4.16.

4–NO_2–4′–Cl–bpy was further investigated electrochemically in 0.3 M [TBA][BF_4]/DCM, see Figure 4.21. The potential was held at −1.408 V in order to convert 4–NO_2–4′–Cl–bpy to [4–NO_2–4′–Cl–bpy]$^{1-}$. The peak at 35,500 cm^{-1} (ε = 23,100 $M^{-1}cm^{-1}$) remained unchanged with a broad shoulder at 35,900cm^{-1}. A further

band grew in at 21,000 cm^{-1} (ε = 3,6000 $M^{-1}cm^{-1}$). Moreover, 4–NO_2–4′–Cl–bpy was also studied in 0.3 M [TBA][BF_4]/THF, see Table 4.4 and Figure 4.22. All three spectra of [4–NO_2–4′–Cl–bpy]$^{1-}$ showed a band in the visible region of the spectrum around 20,500 cm^{-1} and a further feature in the UV region around 35,000 cm^{-1}. The energy of the visible band did vary with the solvent system employed but there was no obvious correlation with solvent acceptor number.

Species	ν(0.3 M [TBA][BF_4]/DCM) /cm^{-1} (ε / $M^{-1}cm^{-1}$)	ν(0.1 M [TBA][BF_4]/DMF) / cm^{-1} (ε / $M^{-1}cm^{-1}$)	ν(0.3 M [TBA][BF_4]/THF) / cm^{-1} (ε / $M^{-1}cm^{-1}$)
4-NO_2-4′-Cl-bpy	30,800 (2,8900) 35,400 (16,300) 40,800 (23,400)	31,000 (3,000) 34,400 (8,5000) 35,500 (10,400)	30,800 (2,7500) 35,474 (17,600) 39,300 (18,600) 40,800 (21,800)
[4-NO_2-4′-Cl-bpy]$^{1-}$	14,900 (6,000) 21,000 (36,000) 35,200 (23,100) 39,500 (19,300)	15,000 (7,000) 20,400 (39,000) 33,900 (14,000) 35,100 (15,400)	13,800 (0,7000) 20,500 (3,9000) 31,100 (13,800) 35,600 (28,800) 39,300 (26,000)

Table 4.4 Peak position cm^{-1} and molar extinction coefficients (ε/$M^{-1}cm^{-1}$), for 4-NO_2-4′-Cl-bpy and [4-NO_2-4′-Cl-bpy]$^{1-}$ in different solvents.

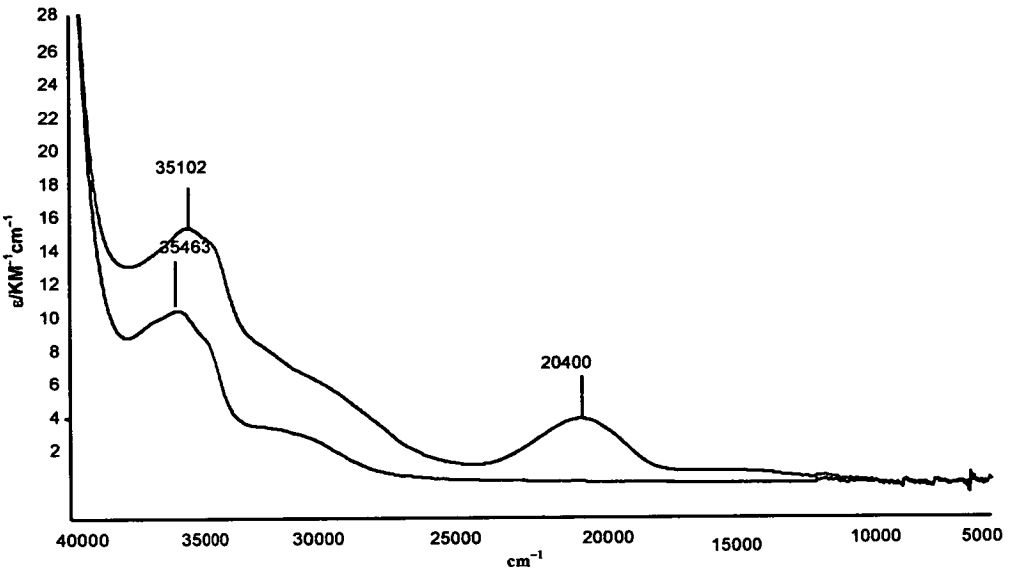

Figure 4.20 UV/Vis/nir absorption spectra of 4–NO_2–4′–Cl–bpy (blue) and [4–NO_2–4′–Cl–bpy]$^{1-}$ (red) in 0.1 M [TBA][BF_4]/DMF, 233 K.

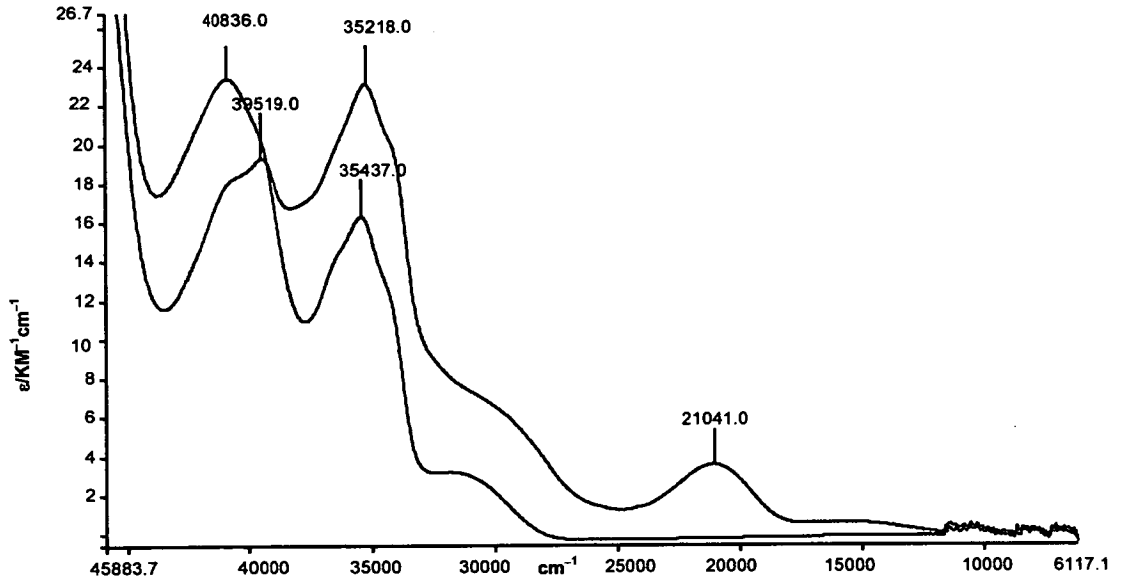

Figure 4.21 UV/Vis/nir absorption spectra of 4–NO_2–4′–Cl–bpy (blue) and [4–NO_2–4′–Cl–bpy]$^{1-}$ (red) in 0.3 M [TBA][BF_4]/DCM, 233 K.

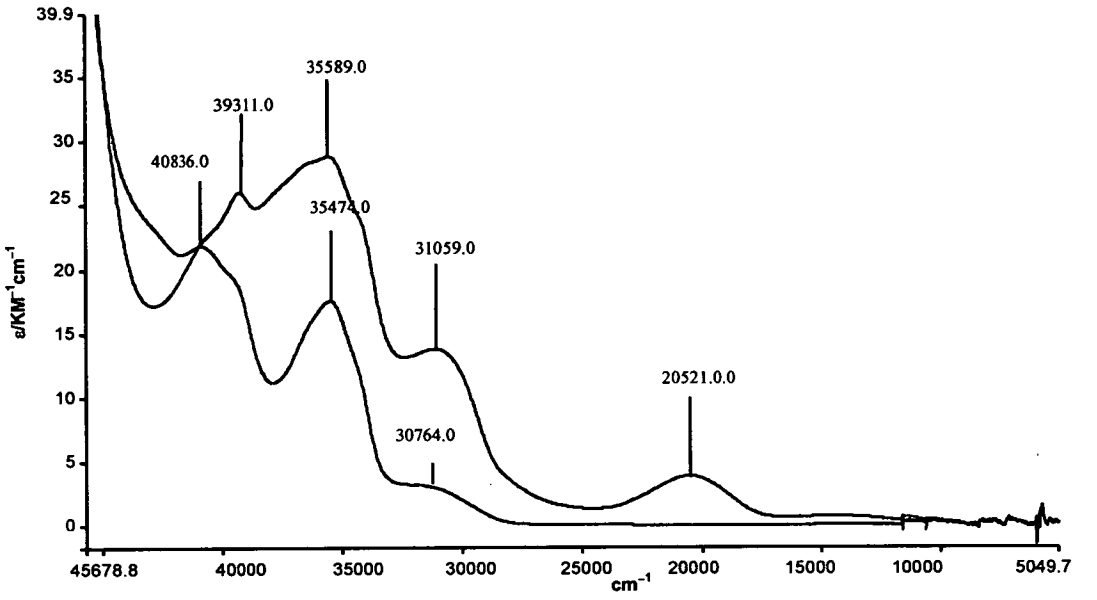

Figure 4.22 UV/Vis/nir absorption spectra of 4–NO_2–4′–Cl–bpy (blue) and [4–NO_2–4′–Cl–bpy]$^{1-}$ (red) in 0.3 M [TBA][BF_4]/THF.

The spectra do not resemble the typical $Na^+(bpy)^{1-}$ spectrum which implies that the unpaired electron in [4–NO_2–4′–Cl–bpy]$^{1-}$ is not delocalised over the entire bpy molecule. The spectra of the mono–reduced 4–NO_2–4′–Cl–bpy and the di–reduced 4,4′–$(NO_2)_2$–bpy have strong similarities and thus, the electron enters a molecular orbital with a substantial amount of NO_2 character due to the strong electron withdrawing character of the NO_2 group.

4.3.4.3. EPR Spectroelectrochemistry of $[4–NO_2–4'–Cl–bpy]^{1–}$.

The X–band EPR of $[4–NO_2–4'–Cl–bpy]^{1–}$ in 0.1 M $[TBA][BF_4]$/DMF at 273 K gave an EPR active signal see Figure 4.23. CAChe calculations, see section 2.7, indicated that the LUMO is based on one ring of the free pro–ligand.

The best simulation of the X–band EPR spectrum of $[4–NO_2–4'–Cl–bpy]^{1–}$ was achieved by coupling of the reduction electron to two nitrogen nuclei (7.200 G and 2.980 G), two equivalent hydrogen nuclei (2.750 G) and a unique hydrogen nucleus (0.400 G). The EPR spectrum of $[4–NO_2–bpy]^{1–}$ has been simulated previously[87] with hyperfine coupling constants of N (7.2 and 3.0 G) and H (two equivalent of 2.6 G and a unique 0.4 G) which are close agreement with those observed here for $[4–NO_2–4'–Cl–bpy]^{1-}$ and were thus assigned along similar lines. Previous studies[87] on $[4–^{14}NO_2–bpy]^{1–}$ and $[4–^{15}NO_2–bpy]^{1–}$ showed that the large N coupling (7.2 G) may be assigned to the N nucleus of the NO_2 group. DFT calculations on $4–NO_2–bpy$ suggest that the other N nucleus was the py N on the same ring as the NO_2 group.[87] The equivalent protons are the 5 and 5′ protons and the further proton is in the 3′ position,[87] *i.e.* there is delocalisation of the electron onto both py rings, but the greater amount of electron density is located on the NO_2 substituted py ring.

X–band EPR spectra of $[4–NO_2–4'–Cl–bpy]^{1–}$ in THF and DCM yielded less resolved spectra than those in DMF, see Figure 4.23–4.25. This may be due to a stronger

interaction between the anion and the electrolyte in the less solvating THF and DCM solvents giving a larger anionic system which tumbles less efficiently, resulting in broader lines in the EPR spectrum.

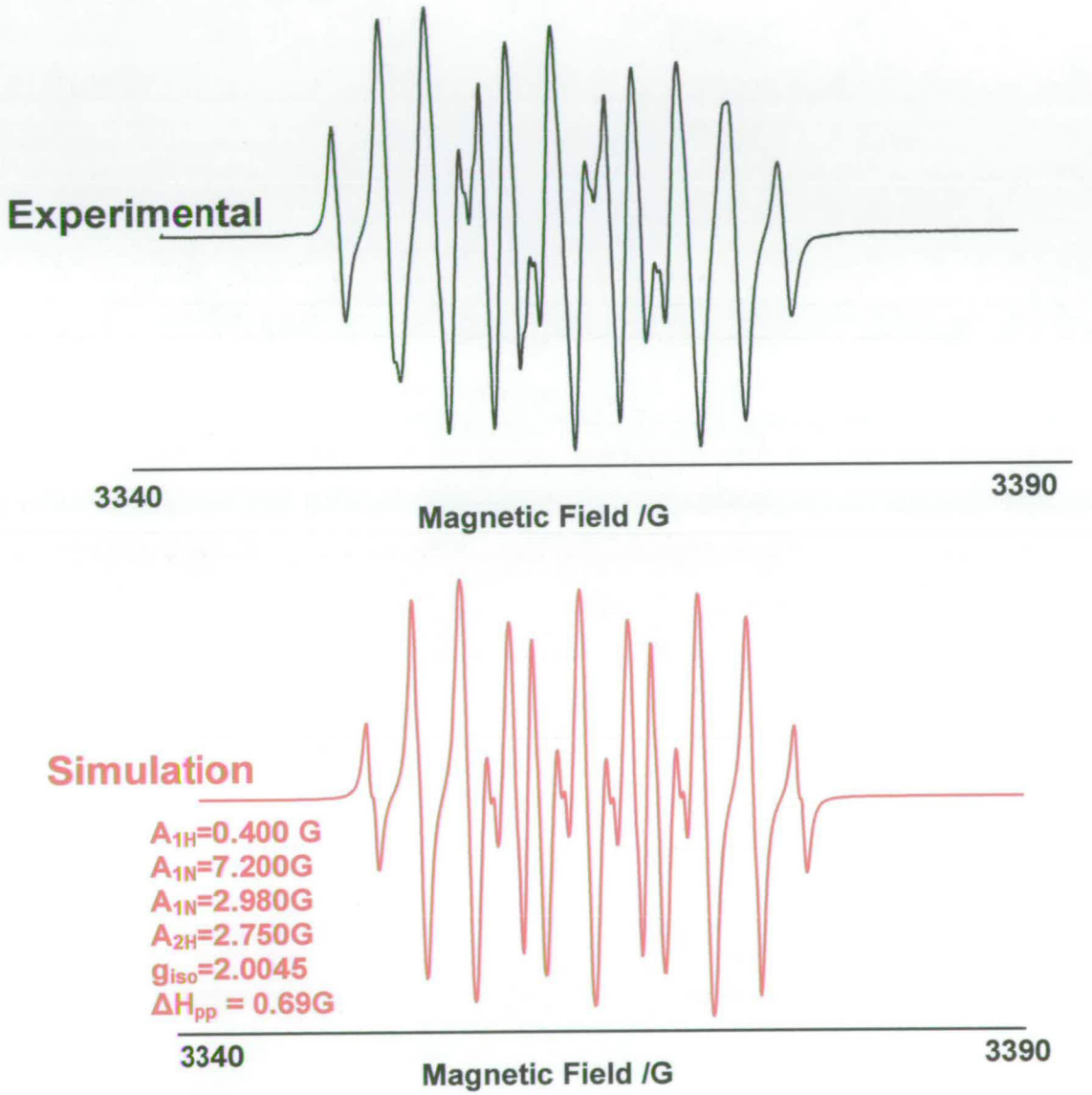

Figure 4.23 Experimental and simulated X–band EPR spectra of $[4\text{–}NO_2\text{–}4'\text{–}Cl\text{–}bpy]^{1-}$ generated *in situ* in 0.1 M $[TBA][BF_4]$/DMF, E_{gen} = –1.40 V, vs. Ag/AgCl, at 273 K.

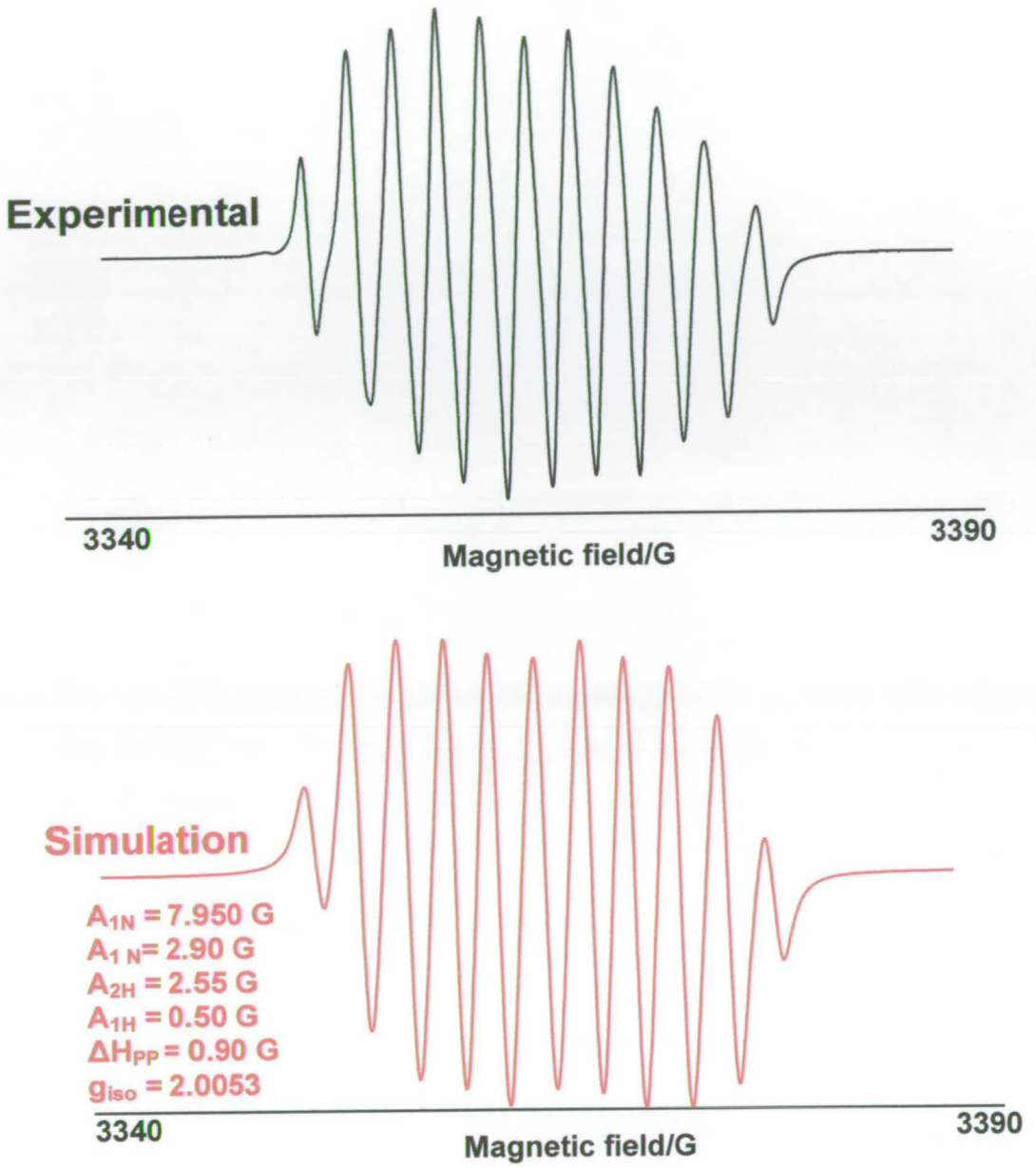

Figure 4.24 Experimental and simulated X–band EPR spectra of $[4–NO_2–4'–Cl–bpy]^{1-}$ generated *in situ* in 0.6 M [TBA][BF_4]/THF, E_{gen} = – 1.40 V, vs. Ag/AgCl, at 273 K.

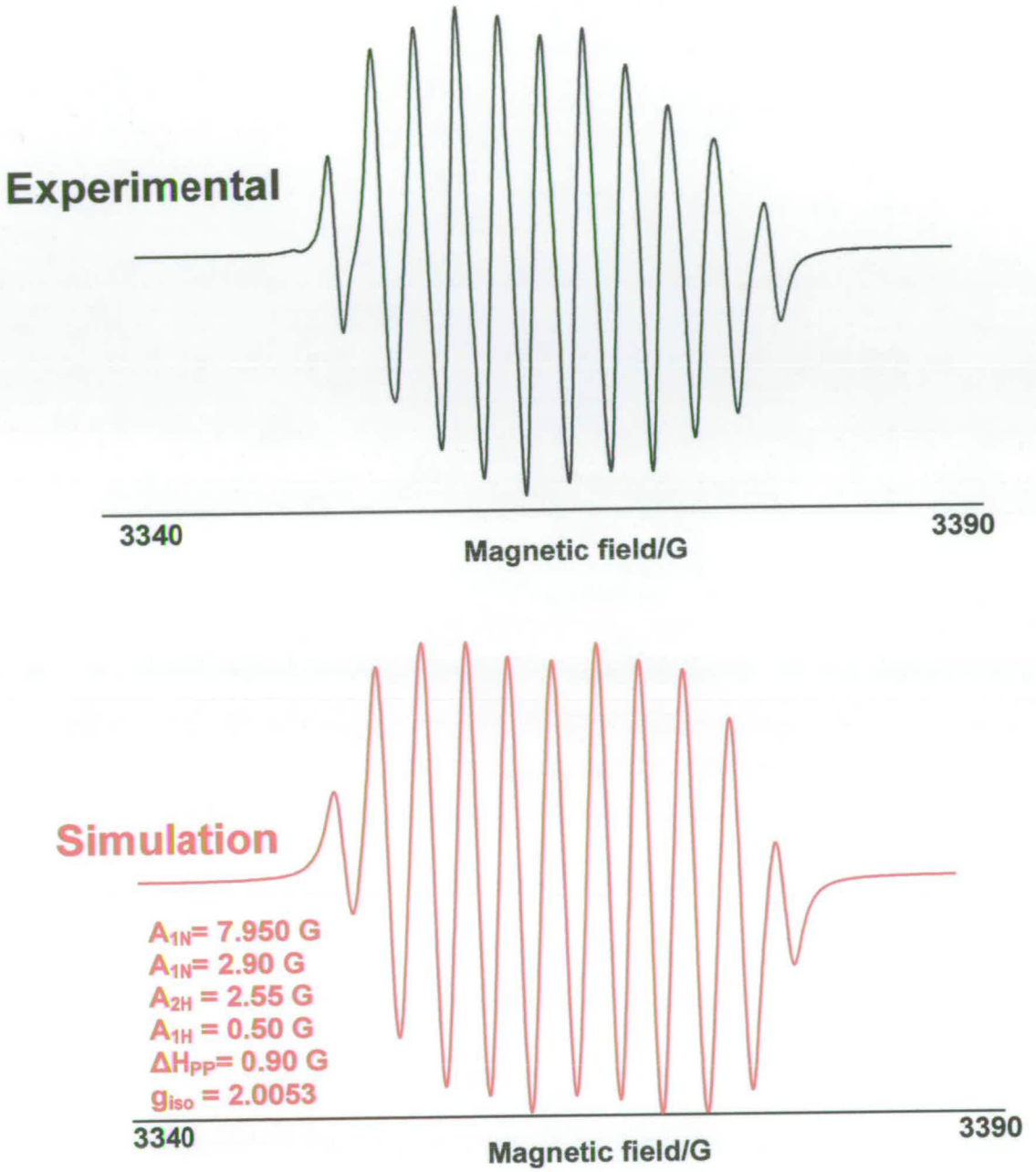

Figure 4.25 Experimental and simulated X–band EPR spectra of $[4–NO_2–4'–Cl–bpy]^{1-}$ generated *in situ* in 0.3 [TBA][BF_4]/ DCM, E_{gen} = –1.40 V, vs. Ag/AgCl, at 253 K.

4.3.5. 2–Cl–4–NO_2–py.

4.3.5.1. Electrochemistry of 2–Cl–4–NO_2–py.

Jack has previously compared the electrochemical and spectroelectrochemical studies of 4,4′–$(NO_2)_2$–bpy with 4–NO_2–py and Murray has compared 5,5′–$(NO_2)_2$–bpy to 3–NO_2–py.[38,87] In a similar manner, 2–Cl–4–NO_2–py was synthesized in order to compare its spectroelectrochemical properties to those of 4,4′–$(NO_2)_2$–6,6′–Cl_2–bpy. 2–Cl–4–NO_2–py undergoes one fully reversible reduction at –0.61 V, followed by an irreversible reduction at –1.66 V in 0.1 M [TBA][BF_4]/ DMF, see Figure 4.6.

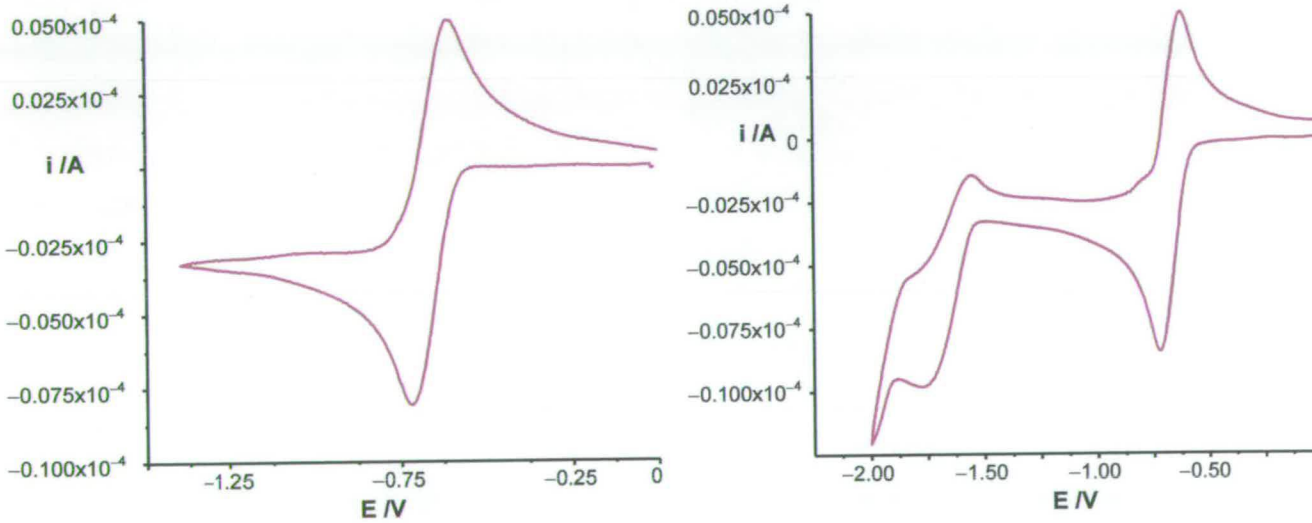

Figure 4.26 Cyclic voltammograms of 2-Cl-4-NO_2-py in 0.1 M [TBA][BF_4]/ DMF, vs. Ag/AgCl, at 293 K, scan rate 0.1 Vs^{-1}.

4.3.5.2. UV/Vis/nir spectroelectrochemistry of 2–Cl–4–NO_2–py.

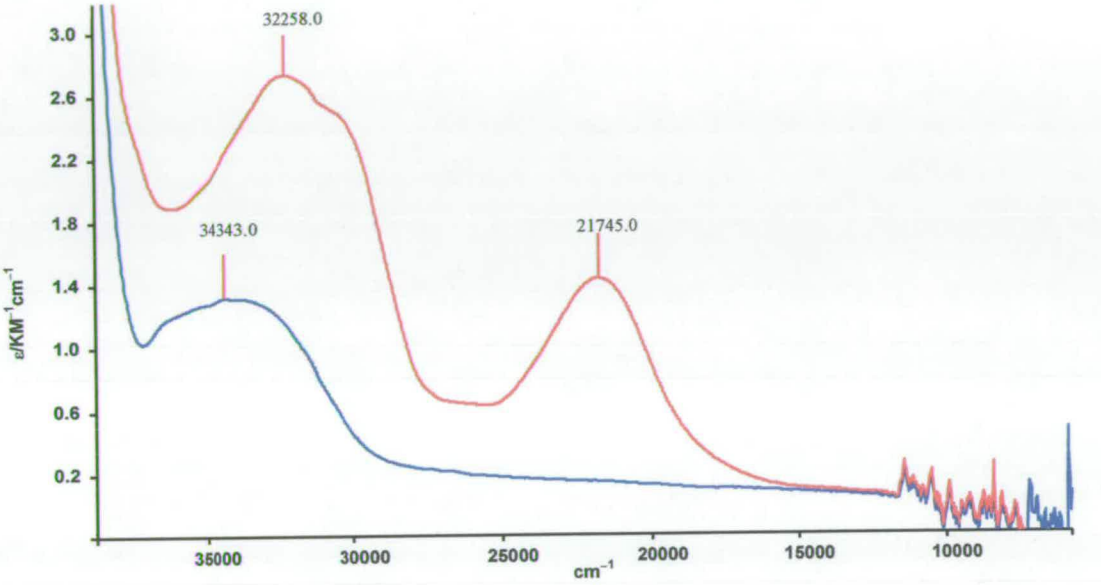

Figure 4.27 UV/Vis/nir absorption spectra of 2–Cl–4–NO_2–py (blue) and $[2–Cl–4–NO_2–py]^{1-}$ (red) in 0.1M [TBA][BF_4]/DMF.

The UV/Vis/nir spectra of 2–Cl–4–NO_2–py and $[2–Cl–4–NO_2–py]^{1-}$ shown in Figure 4.27 resembled those of 4–NO_2–bpy and $[4–NO_2–bpy]^{1-}$, respectively.[38] This is evidence for the localisation of the unpaired electron on one py ring system.

The neutral species, 2–Cl–4–NO_2–py gave one band at high energy 34,343 cm^{-1} ($\varepsilon = 13\,215\ M^{-1}cm^{-1}$), see Figure 4.27. When the potential was set at –1.00 V, a new band grew in at 21,745 cm^{-1} ($\varepsilon = 14\,329\ M^{-1}cm^{-1}$) and a further intense band at 32,258 cm^{-1} ($\varepsilon = 27\,329\ M^{-1}cm^{-1}$). The spectra suggested that all the transitions were

intramolecule charge transfer transitions. The $\pi \rightarrow \pi^*$ transition of py occurs at 40,000 cm^{-1}.[89] Hence the bands presented here could be assigned as $\pi \rightarrow \pi^*$ transitions delocalised over the whole molecule. The nitro group heavily influences the UV/Vis/nir spectra.

4.3.5.3. EPR Spectroelectrochemistry of $[2\text{–Cl–4–NO}_2\text{–py}]^{1-}$.

In situ electrochemical reduction of 2–Cl–4–NO_2–py in 0.1 M [TBA][BF_4]/DMF yielded the EPR active mono–reduced species, the spectrum of which has 9 main lines, see Figure 4.28. Using CAChe software, see section 2.7, molecular orbital calculations indicated that the LUMO was delocalised over the whole 2–Cl–4–NO_2–py compound.

The experimental X–band EPR spectrum of $[2\text{–Cl–4–NO}_2\text{–py}]^{1-}$ can be simulated by coupling of the unpaired electron to two ^{14}N nuclei (6.50 G and 2.7 G) and two equivalent hydrogen nuclei (3.2 G). This situation can be compared with that of $[4\text{–NO}_2\text{–py}]^{1-}$ which has been studied previously by Jack.[38] The X–band EPR spectrum of $[4\text{–NO}_2\text{–py}]^{1-}$ showed an 11 line signal and was successfully simulated by coupling of the unpaired electron to two ^{14}N nuclei (8.43 G and 2.43 G) a pair of ^{1}H nuclei (3.04 G), and a further pair of equivalent H nuclei (0.45 G).[38] DFT calculations indicate that the larger proton couplings in $[4\text{–NO}_2\text{–py}]^{1-}$ are to the positions *ortho* to the NO_2 substituent. It was suggested that the *ortho* protons were responsible for the hyperfine coupling observed in the X–band EPR spectrum of $[2\text{–Cl–4–NO}_2\text{–py}]^{1-}$. Although substitution of one hydrogen by a chloro atom should result in no pairs of equivalent hydrogen atoms in

[2–Cl–4–NO_2–py], the electrochemistry, UV/Vis spectroelectrochemistry and indeed the EPR spectroelectrochemistry all indicate that the 2–Cl–4–NO_2–py derivative is only slightly different electronically from the 4–NO_2–py molecule. That is the nitro group dominates the electronic behaviour of these substituted pyridines. The two protons *ortho* to the NO_2 group in 2–Cl–4–NO_2–py will not be exactly equivalent but the resolution of the EPR spectrum did not permit any differentiation.

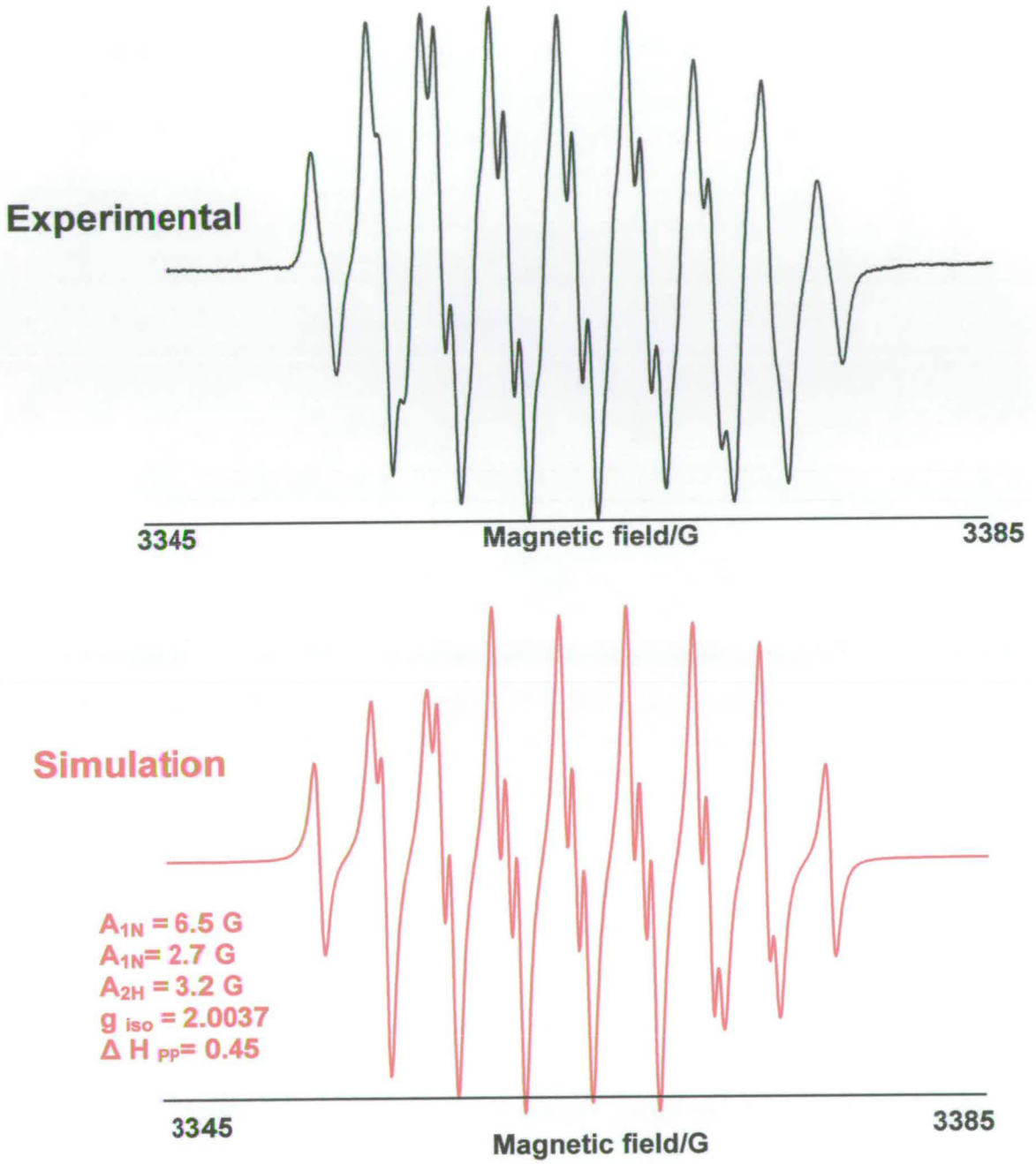

Figure 4.28 Experimental and simulated X–band EPR spectra of $[2–Cl–4–NO_2–py]^{1-}$ generated *in situ* in 0.1 M [TBA][BF_4]/ DMF, E_{gen} = –1.00 V, vs. Ag/AgCl, at 233 K.

4.4. Comparison of the NO_2 substituted 2,2'–bpy and py compounds.

4.4.1. Electrochemistry of the NO_2 substituted 2,2'–bpy and py compounds.

Compound	$E_{½,1}$ /V	$E_{½,2}$ /V	$E_{½,3}$ /V
4,4′-$(NO_2)_2$-bpy	-0.67	-0.79	-
4-NO_2-bpy	-0.79	-	-
4-NO_2-4′-Cl-bpy	-0.68	-	-
4,4′-$(NO_2)_2$-6,6′-Cl_2-bpy	-0.48	-0.59	-1.51[a]
4-NO_2-2-Cl-py	-0.61	-1.66[a]	-
4-NO_2-py	-0.74	-	-

Table 4.5 $E_{½}$ values for nitro substituted 2,2′-bpy and py compounds, vs. Ag/AgCl in 0.1 M [TBA][BF_4]/DMF, at 293 K.

(a) irreversible reduction.

On comparison of the first half wave potential of the compounds, listed in Table 4.5 a clear trend is observed. The reduction potentials of 4,4′–$(NO_2)_2$–6,6′–Cl_2–bpy are shifted to more positive values due to the additive effect of the chloride on the *ortho* position compared to protons in 4,4′–$(NO_2)_2$–bpy. Thus, 4,4′–$(NO_2)_2$–6,6′–Cl_2–bpy was much easier to reduce than the other nitro–substituted 2,2′–bpy molecules. Again, the $E_{½}$ values of 4–NO_2–4′–Cl–bpy and 4–NO_2–2–Cl–py are shifted to more positive

potentials compared to 4–NO_2–bpy and 4–NO_2–py, respectively. This indicates that the nature of the substituent has a strong effect on the electronic character of the molecule.

4.4.2. UV/Vis/nir spectroelectrochemistry of the NO_2 substituted 2,2'–bpy and py compounds.

Table 4.6 shows the peak position (cm^{-1}) and the molar extinction coefficients, $\varepsilon/(M^{-1}cm^{-1})$, for $[4,4'–(NO_2)_2–bpy]^{0/2-}$, $[4,4'–(NO_2)_2–6,6'–Cl_2–bpy]^{0/2-}$, $[4–NO_2–4'–Cl–bpy]^{0/1-}$ and $[2–Cl–4–NO_2–py]^{0/1-}$.

Species	4,4'-$(NO_2)_2$-bpy /cm^{-1} ($\varepsilon/M^{-1}cm^{-1}$)	4,4'-$(NO_2)_2$-6,6'-Cl_2-bpy /cm^{-1} ($\varepsilon/M^{-1}cm^{-1}$)	4-NO_2-4'-Cl-bpy / cm^{-1} ($\varepsilon/M^{-1}cm^{-1}$)	2-Cl-4-NO_2-py / cm^{-1} ($\varepsilon/M^{-1}cm^{-1}$)
Neutral molecule	34,370 (7,470) 32,100 (7,511)	30,388 (19,123)	35,500 (10,400) 34,400 (85,000) 31,000(3,000)	34,300 (13,200)
Monoanion			35,100 (15,400) 33,900 (14,000) 20,400 (39,000) 15,000 (7,000)	32,300 (27,300) 30,400 (24,700) 21,750 (14,300)
Dianion	33,900 (17,950) 32,560 (17,820) 20,615 (10,160)	32,347 (27,175) 30,488 (27,446) 20,406 (18,836) 15,038 (65,968)		

Table 4.6 Peak position and the molar extinction coefficients, ε, for nitro substituted 2,2'-bpy and 2-Cl-4-NO_2-py, in 0.1 M [TBA][BF_4]/DMF, at 233 K.

From the data presented in Table 4.6, there are obvious similarities between analogous spectra. In 4,4′–$(NO_2)_2$–6,6′–Cl_2–bpy the peaks were shifted to slightly lower energy compared to the others which correlates with the electrochemistry data. The hypothesis that the unpaired electron in $[4,4'–(NO_2)_2–bpy]^{2–}$, $[4,4'–(NO_2)_2–6,6'–Cl_2–bpy]^{2–}$ and $[4–NO_2–4'–Cl–bpy]^{1–}$ is occupying a molecular orbital which spans only one half of the system, that is, based on the NO_2, py ring is strengthened on consideration of monoreduced 2–Cl–4–NO_2–py which bears notable similarities in both EPR and UV/Vis/nir spectra.

4.4.3. EPR of the NO_2 substituted 2,2'–bpy compunds.

$[2\text{-Cl-4-NO}_2\text{-py}]^{1-}$	$[4\text{-NO}_2\text{-4'-Cl-bpy}]^{1-}$	$[4,4'\text{-(NO}_2)_2\text{-6,6'-Cl}_2\text{-bpy}]^{2-}$	$[4,4'\text{-(NO}_2)_2\text{-bpy}]^{2-}$
$A_{1N} = 6.50$ G	$A_{1N} = 7.200$G	$A_{1N} = 6.650$ G	$A_{1N} = 6.770$G
$A_{1N} = 2.70$ G	$A_{1N} = 2.980$G	$A_{1N} = 2.552$ G	$A_{1N} = 2.700$ G
$A_{2H} = 3.20$ G	$A_{2H} = 2.750$G	$A_{1H} = 3.325$ G	$A_{1H} = 3.25$ G
$g_{iso} = 2.0037$	$A_{1H} = 0.400$ G	$A_{1H} = 2.552$ G	$A_{1H} = 2.99$ G
$\Delta H_{pp} = 0.45$ G	giso=2.0045	giso=2.0039	$A_{1H} = 0.20$ G
	$\Delta H_{pp} = 0.69$G	$\Delta H_{pp} = 0.40$ G	$g_{iso} = 2.00545$
			$\Delta H_{pp} = 0.55$ G

Table 4.7 Coupling constants obtained from simulation of the X-band EPR spectra for the reduced species of nitro substituted 2,2′-bpy and 2-Cl-4-NO_2-py in 0.1 M [TBA][BF_4]/DMF.

From the data presented in Table 4.7, it can be seen that the EPR spectra show similar features. All molecules exhibited a large coupling to one N nucleus which Murray has

assigned to the NO_2 group in $[4,4'\text{-}(NO_2)_2\text{-bpy}]^{2-}$.[87] The smaller N coupling is to the py N nucleus to which the NO_2 group is attached. Furthermore, all reduced species exhibit hyperfine coupling to protons of approximately the same magnitude as the smaller coupling to an N nuclei. Thus, all pro–ligands investigated in this chapter have similar electronic characters dominated by the NO_2 group.

4.5. Pt Complexes of 4,4′–$(NO_2)_2$–bpy and 4–NO_2–4′–Cl–bpy.

The complexes $[Pt(4,4'\text{–}(NO_2)_2\text{–bpy})Cl_2]$ and $[Pt(4\text{–}NO_2\text{–}4'\text{–Cl–bpy})Cl_2]$ were prepared by the following general procedure, see section 2.4. A suspension of the appropriate pro–ligand (1.1 equivalents) was heated under reflux, with stirring, in an aqueous solution of $K_2[PtCl_4]$ (1 equivalent). The precipitate was collected by filtration, washed with water, dried under vacuum and recrystallised from *N,N′*–dimethylformamide (DMF) solution. CHN and mass spectroscopy indicate a successful synthesis of these complexes.

4.5.1. Electrochemistry of $[Pt(4,4'\text{–}(NO_2)_2\text{–bpy})Cl_2]$ and $[Pt(4\text{–}NO_2\text{–}4'\text{–Cl–bpy})Cl_2]$.

The cyclic voltammetric investigations of $[Pt(4\text{–}NO_2\text{–}4'\text{–Cl–bpy})Cl_2]$ in 0.1 M $[TBA][BF_4]$/DMF, at 293 K, revealed two reversible, one–electron reduction processes at –0.31 V and –0.81 V. The cyclic voltammetric investigation of $[Pt(4,4'\text{–}(NO_2)_2\text{–bpy})Cl_2]$ in 0.1 M $[TBA][BF_4]$/DMF at 293 K, showed two reversible one–electron reductions at –0.27 and –0.46 V, see Figure 4.29. Both complexes were studied in wide range of

solvents. Table 4.8 and 4.9 show the half–wave potential of [Pt(4–NO_2–4′–Cl–bpy)Cl_2] and [Pt(4,4′–(NO_2)$_2$–bpy)Cl_2] in different solvents, respectively.

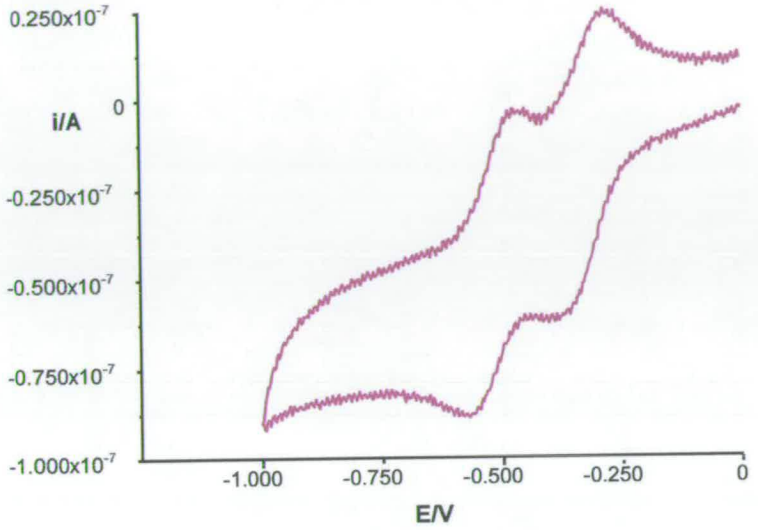

Figure 4.29 The first two reversible reductions of [Pt(4,4'-(NO_2)$_2$- bpy)Cl_2] in 0.1 M [TBA][BF_4]/DMF, vs. Ag/AgCl, scan rate 0.1 Vs^{-1}, at 293 K.

Solvent	Acceptor Number[100]	$E_{½,1}$	$E_{½,2}$	$\Delta E_{½}$/V
DMSO	19.3	-0.28	-0.79	0.51
MeCN	18.9	-0.30	-0.81	0.51
DMF	16.0	-0.31	-0.81	0.50
THF	8.0	-0.30	-0.82	0.52

Table 4.8 $E_{½}$ values of [Pt(4–NO_2–4′–Cl–bpy)Cl_2] *vs.* Ag/AgCl in various solvents at 298 K (electrolyte = [TBA][BF_4]).

Solvent	Acceptor Number[100]	$E_{½,1}$	$E_{½,2}$	$\Delta E_{½}$/V
MeCN	18.9	-0.23	-0.42	0.19
DMF	16.0	-0.27	-0.47	0.20
DCM	20.4	-0.29	-0.48	0.19

Table 4.9 $E_{½}$ values of [Pt(4,4′-$(NO_2)_2$-bpy)Cl_2] vs. Ag/AgCl in various solvents at 298 K (electrolyte = [TBA][BF_4]).

From the data presented in Tables 4.8 and 4.9, it is clear that the solvent has no significant effect on the electrochemical behaviour of [Pt(4–NO_2–4′–Cl–bpy)Cl_2] and [Pt(4,4′–$(NO_2)_2$–bpy)Cl_2]. It is worth noting that binding the free ligands to Pt(II) leads to a positive shift in the reduction potential values, this is because of the stabilization of the compounds as a result of formation of the complexes. However, no solvent dependence was observed for [Pt(4–NO_2–4′–Cl–bpy)Cl_2] and [Pt(4,4′–$(NO_2)_2$–bpy)Cl_2] as the stabilisation of the reduced species of the complexes by solvation was not significant.

4.5.2. UV/Vis/nir Spectroelectrochemistry of [Pt(4,4′–$(NO_2)_2$–bpy)Cl_2] and [Pt(4–NO_2–4′–Cl–bpy)Cl_2].

The UV/Vis/nir spectra of [Pt(4,4′–$(NO_2)_2$–bpy)Cl_2] and [Pt(4–NO_2–4′–Cl–bpy)Cl_2] in 0.1 M [TBA][BF_4]/DMF were similar, see Figure 4.30 and 4.31. The bands may be assigned to similar electronic transitions. Comparison of the free and bound ligand indicates that the higher energy bands can be assigned as $\pi \rightarrow \pi^*$ intraligand bands and

the lower energy band at *ca.* 24,000 cm^{-1} is a MLCT, as this band was not observable in the UV/Vis/nir spectrum of the pro–ligand, see Table 4.6.

$[Pt(4–NO_2–4'–Cl–bpy)Cl_2]$ showed a high energy band at 36,000cm^{-1} (ε = 13,700 $M^{-1}cm^{-1}$), see Figure 4.31. Holding the potential at –0.68 V, to generate the mono–reduced species resulted in the growth of an intense band at 22,600 cm^{-1} (ε = 4,000 $M^{-1}cm^{-1}$), and a broad band grew in the nir region at *ca.* 9–12 kcm^{-1}. Attempts to generate the di–reduced species were unsuccessful and even at low temperature the direduced species was not stable.

Figure 4.31 shows the absorption spectrum of $[Pt(4,4'–(NO_2)_2–bpy)Cl_2]$ before reduction (blue line). The higher energy band at 32,480 cm^{-1} (before reduction) was assigned as an internal charge transfer $\pi \rightarrow \pi^*$. The band at 23,210 cm^{-1} was assigned as a MLCT and can be compared with the spectrum of the free ligand which does not show this peak. On reduction to $[Pt(4,4'–(NO_2)_2–bpy)Cl_2]^{2–}$, peaks in the visible region of the spectra increased in intensity. This correlates with the previous study done by Jack.[38] All bands are assigned as intraligand electronic transitions from and to the partially occupied LUMO and LUMO–1 orbitals of the parent complex. From the similarity of the spectra of both $[Pt(4,4'–(NO_2)_2–bpy)Cl_2]$ and $[Pt(4–NO_2–4'–Cl–bpy)Cl_2]$, the bands observed for $[Pt(4–NO_2–4'–Cl–bpy)Cl_2]$ can be assigned as a mixture of MLCT (band at 24,800 cm^{-1}) and $\pi \rightarrow \pi^*$ intaligand transitions (bands at higher energy). Comparing the complexes under study with related compounds (free ligands) makes it easier to assign

the absorptions. UV/Vis/nir spectra of $[Pt(4,4'–(NO_2)_2–bpy)Cl_2]^{2-}$ and $[Pt(4–NO_2–4'–Cl–bpy)Cl_2]^{1-}$ have similar features to that of coordinated bpy^{1-} and therefore, the unpaired electron will delocalised over both ring systems rather than confined to a $4–NO_2–py$ moiety as it is in the free ligands. Binding of the ligand to the Pt(II) centre enforces the substituted bpy ligand to be planar. The spectrum of the reduced free ligand and bound ligand exhibit differences, particularly in the nir region, around 10,000 cm^{-1}.

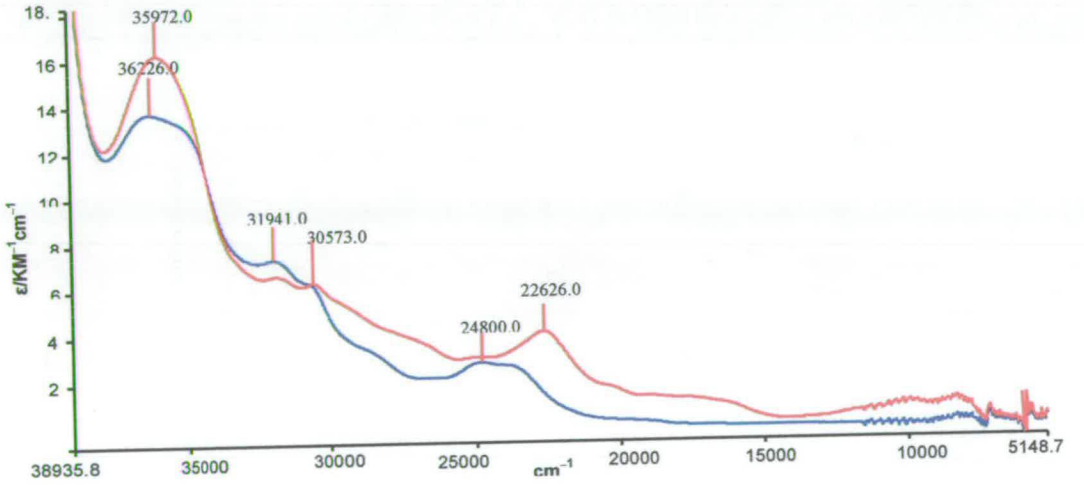

Figure 4.30 UV/Vis/nir absorption spectra of $[Pt(4–NO_2–4'–Cl–bpy)Cl_2]$ (blue) and $[Pt(4–NO_2–4'–Cl–bpy)Cl_2]^{1-}$ (red) in 0.1 M [TBA][BF_4]/DMF at 223 K, E_{gen} = –0.68 V.

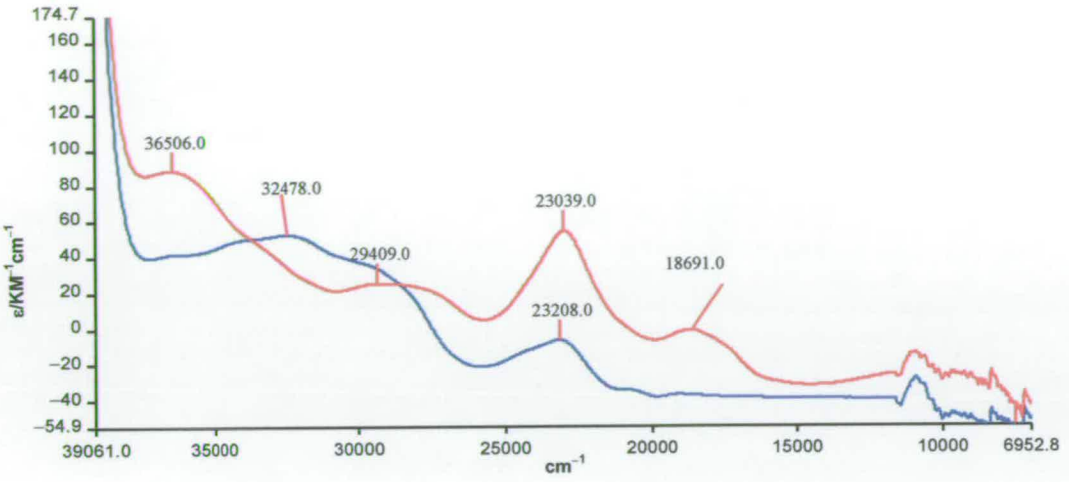

Figure 4.31 UV/Vis/nir absorption spectra of $[Pt(4,4'–(NO_2)_2–bpy)Cl_2]$ (blue) and $[Pt(4,4'–(NO_2)_2–bpy)Cl_2]^{2–}$ (red) in 0.1M [TBA][BF_4]/DMF at 233 K, E_{gen} = –0.86 V.

4.5.3. EPR spectra of $[Pt(4,4'–(NO_2)_2–bpy)Cl_2]^{1–/2–}$ and $[Pt(4–NO_2–4'–Cl–bpy)Cl_2]^{1–}$.

The mono–anions of $[Pt(4,4'–(NO_2)_2–bpy)Cl_2]^{1–}$ and $[Pt(4–NO_2–4'–Cl–bpy)Cl_2]^{1–}$ can be generated *in situ* to give EPR active solutions. The solution X–band EPR spectrum of $[Pt(4,4'–(NO_2)_2–bpy)Cl_2]^{1–}$ in 0.1 M [TBA][BF_4]/DMF at 233 K showed coupling of the unpaired electron to ^{195}Pt with any hyperfine coupling to the ligand nuclei unresolved, see Figure 4.32. An ^{195}Pt hyperfine coupling constant of A_{iso} = 55 G centred at g_{iso} = 2.004 was observed in 0.1 M [TBA][BF_4]/DMF solution at 233 K, see Figure 4.32. On reduction to the di–reduced species of $[Pt(4,4'–(NO_2)_2–bpy)Cl_2]^{2–}$ an EPR spectrum was observed at room temperature and at 173 K, see Figure 4.33. This indicates that the two added electrons are unpaired, *i.e.* a spin–triplet state species was generated. The best simulation of $[Pt(4,4'–(NO_2)_2–bpy)Cl_2]^{2–}$ spectrum was obtained by assuming coupling

of the unpaired electron to ^{195}Pt (29.5 G); note the coupling is approximately half that of the mono–reduced species, a pair of equivalent ^{14}N nuclei (4.40 G) and a pair of ^{1}H nuclei (2.80 G) with a Lorentzian line width of 0.75 G, see Figure 4.33. This is in good agreement with previous EPR simulations of the complex by McInnes and Jack.[31,38] In line with work done by Murray[87], the largest nitrogen coupling can be assigned as the pyridine ring nitrogen. Here, as in the earlier work by McInnes and Jack, no attempt was made to assign the position of the ^{1}H nuclei.[24] The large difference in linewidth of the solution spectra of mono–reduced (20.0 G) and di–reduced (0.75 G) $[Pt(4,4'–(NO_2)_2–bpy)Cl_2]$ may be attributed to an "electron hopping" mechanism. In the mono–anion the reduction electron can be thermally excited to a further low lying orbital (the LUMO–1 of the neutral molecule). This hopping mechanism cannot occur in the di–anion as both low–lying orbitals (LUMO and LUMO–1) are now partially occupied. This hopping between orbitals can contribute to line broadening in the observed EPR spectrum.

$[Pt(4–NO_2–4'–Cl–bpy)Cl_2]^{1-}$ yielded an EPR signal in 0.1 M [TBA][BF_4]/DMF, see Figure 4.34. Unlike the mono reduced species of $[Pt(4,4'–(NO_2)_2–bpy)Cl_2]^{1-}$, the solution EPR spectrum of $[Pt(4–NO_2–4'–Cl–bpy)Cl_2]^{1-}$ showed hyperfine coupling to the ^{195}Pt nucleus and interactions with ligand nuclei were also observed. The X–band EPR spectrum of the monoanion $[Pt(4–NO_2–4'–Cl–bpy)Cl_2]^{1-}$ which was generated at room temperature can be simulated by a coupling to ^{195}Pt (14.50 G), two nitrogen (1.50 G and 1.20 G) and two hydrogen (1.00 G and 1.95 G) nuclei, see Figure 4.34. In both systems on complexation of the molecules the two pyridine rings were forced to be planar

and were no longer orthogonal, thus, the LUMO will be ligand based and the LUMO may be delocalised over the whole substituted bipyridine ligand.

On cooling to 173 K the frozen glass X–band EPR spectrum of $[Pt(4,4'–(NO_2)_2–bpy)Cl_2]^{2-}$ is a broad line showing some coupling of the unpaired electrons to ^{195}Pt, see Figure 4.35. However, any hyperfine interactions were not well resolved. No features appear in the spectrum which were typical of a spin–triplet system, *i.e.* there is no observable electron–electron coupling fine structure.

The hyperfine interactions were not well resolved and the spectrum should be run on a Q–band spectrometer to split the signal so that the ^{195}Pt coupling can be resolved, see Figure 4.35.

In contrast $[Pt(4–NO_2–4'–Cl–bpy)Cl_2]^{1-}$, on cooling to 153 K, revealed a rhombic X–band EPR spectrum, see Figure 4.36. Rhombic g and ^{195}Pt hyperfine tensors were observed with $g_1 = 2.02765$, $g_2 = 2.00665$, $g_3 = 1.98265$, $A_1 = -30$ G, and $A_2 = -44$ G. The average of $g_1 + g_2 + g_3$ is in a good agreement with g_{iso}. The hyperfine splitting of the high field g_3 component (A_3) was estimated to be –31G from the magnitudes of A_{iso}, A_1 and A_2 using Equation 4.1.

$$A_3 = 3A_{iso} - A_1 - A_2 \qquad \textbf{Equation 4.1.}$$

Table 4.10 gives details of the EPR parameters of $[Pt(4–NO_2–4'–Cl–bpy)Cl_2]^{1-}$ as a frozen glass.

g_{iso}[a]	g_1[b]	g_2	g_3	A_{iso} (Pt)[c] W_1/G	A_1[c] /G W_1/G	A_2[c] /G W_2/G	A_3[c, d] /G W_3/G
2.0042	2.02765	2.00665	1.98265	-14.50	-30 9	-44 10	-21 50

Table 4.10 EPR parameters of $[Pt(4\text{-}NO_2\text{-}4'\text{-}Cl\text{-}bpy)Cl_2]^{1-}$ at 153 K in 0.1 M $[TBA][BF_4]$/DMF.

Using Equations 1.1 – 1.3 in Chapter 1 the contribution of Pt $5d_{yz}$ and $6p_z$ orbitals to the SOMO can be calculated as 2.6 % and 0.33 %, respectively. The total contribution of the Pt based orbitals to the SOMO of $[Pt(4–NO_2–4'–Cl–bpy)Cl_2]^{1-}$ is *ca.* 3 % , confirming that the electron enters an orbital that is predominantly ligand based. The related complex $[Pt(4–NO_2–bpy)Cl_2]^{1-}$ has a total Pt contribution to the SOMO of *ca.* 8 %. Thus, the semi–occupied MO in $[Pt(4–NO_2–bpy)Cl_2]^{1-}$ has a greater contribution from the Pt nucleus than $[Pt(4–NO_2–4'–Cl–bpy)Cl_2]^{1-}$. This was expected as the chloro group is more electron–withdrawing compared to the hydrogen, which will pull electron density away from the metal, thus the contribution of the Pt based orbital to the SOMO in $[Pt(4–NO_2–4'–Cl–bpy)Cl_2]^{1-}$ is less than it is in $[Pt(4–NO_2–bpy)Cl_2]^{1-}$.

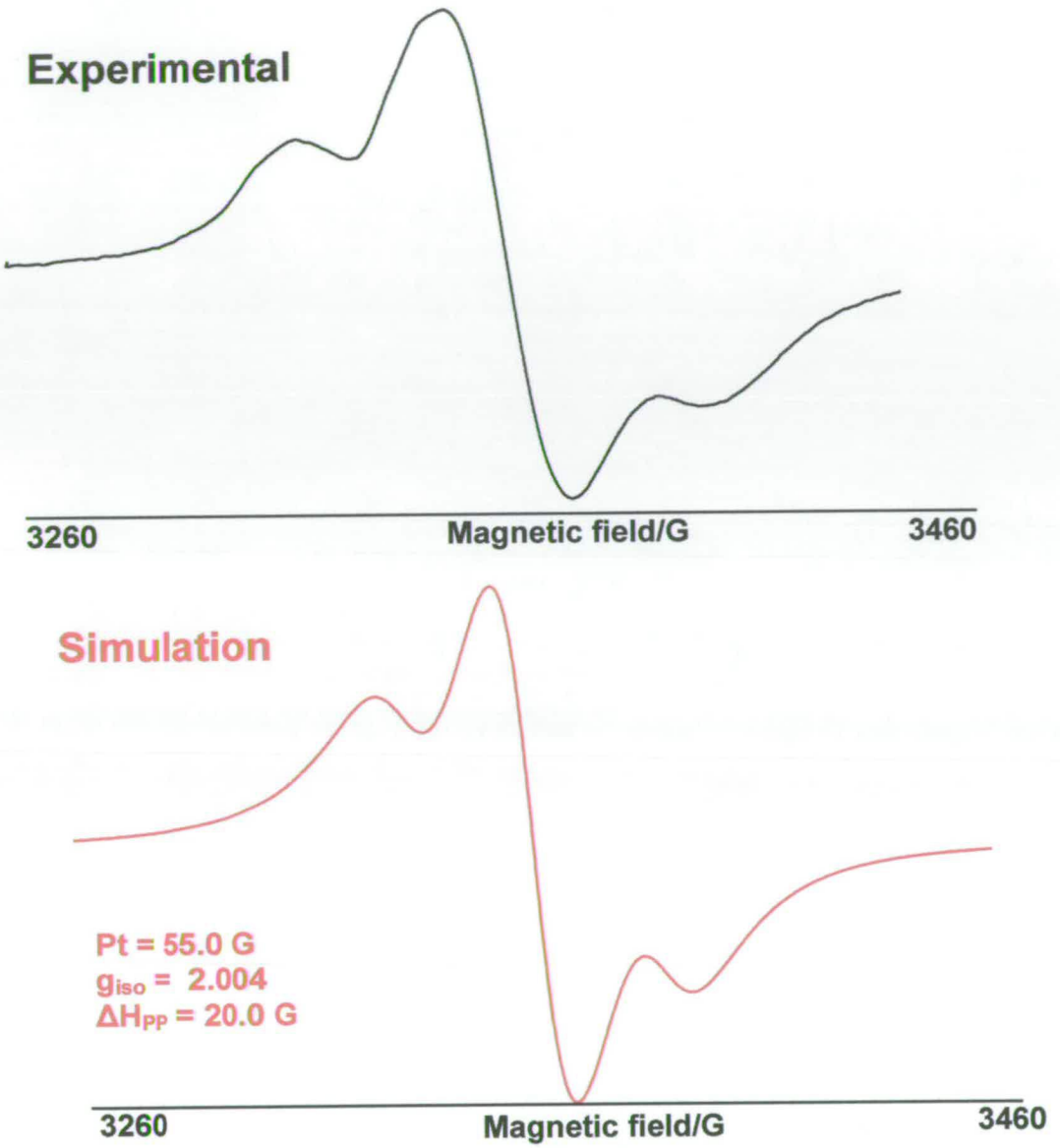

Figure 4.32 Experimental and simulated X-band EPR spectra at 233 K of $[Pt(4,4'\text{-}(NO_2)_2\text{-bpy})Cl_2]^{1-}$ generated in situ in 0.1 M [TBA][BF_4]/DMF, E_{gen} = -0.88 V, vs. Ag/AgCl.

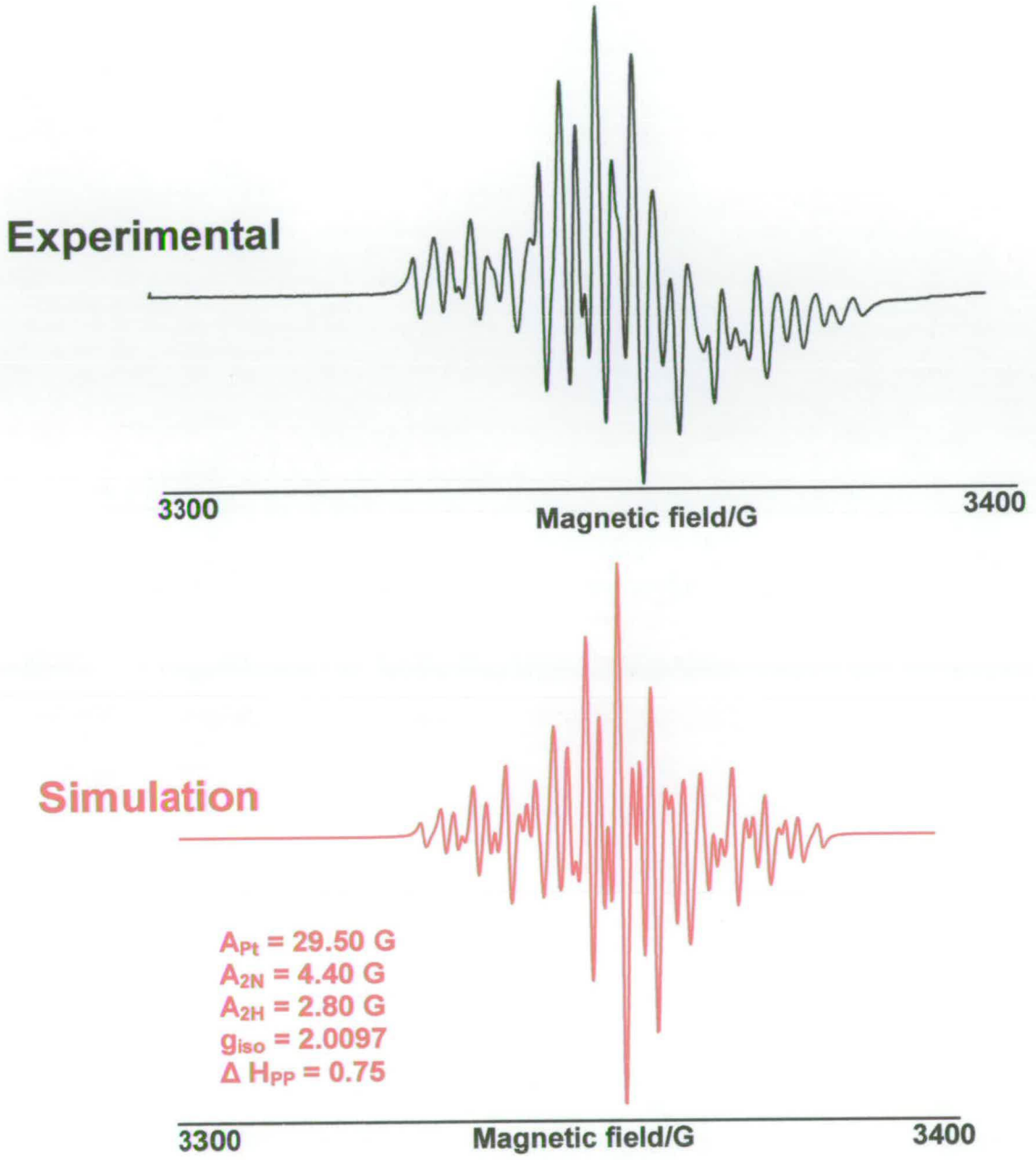

Figure 4.33 Experimental and simulated X-band EPR spectra at 253 K of $[Pt(4,4'–(NO_2)_2–bpy)Cl_2]^{2-}$ generated *in situ* in 0.1 M [TBA][BF_4]/DMF, E_{gen} = –0.88 V, vs. Ag/AgCl.

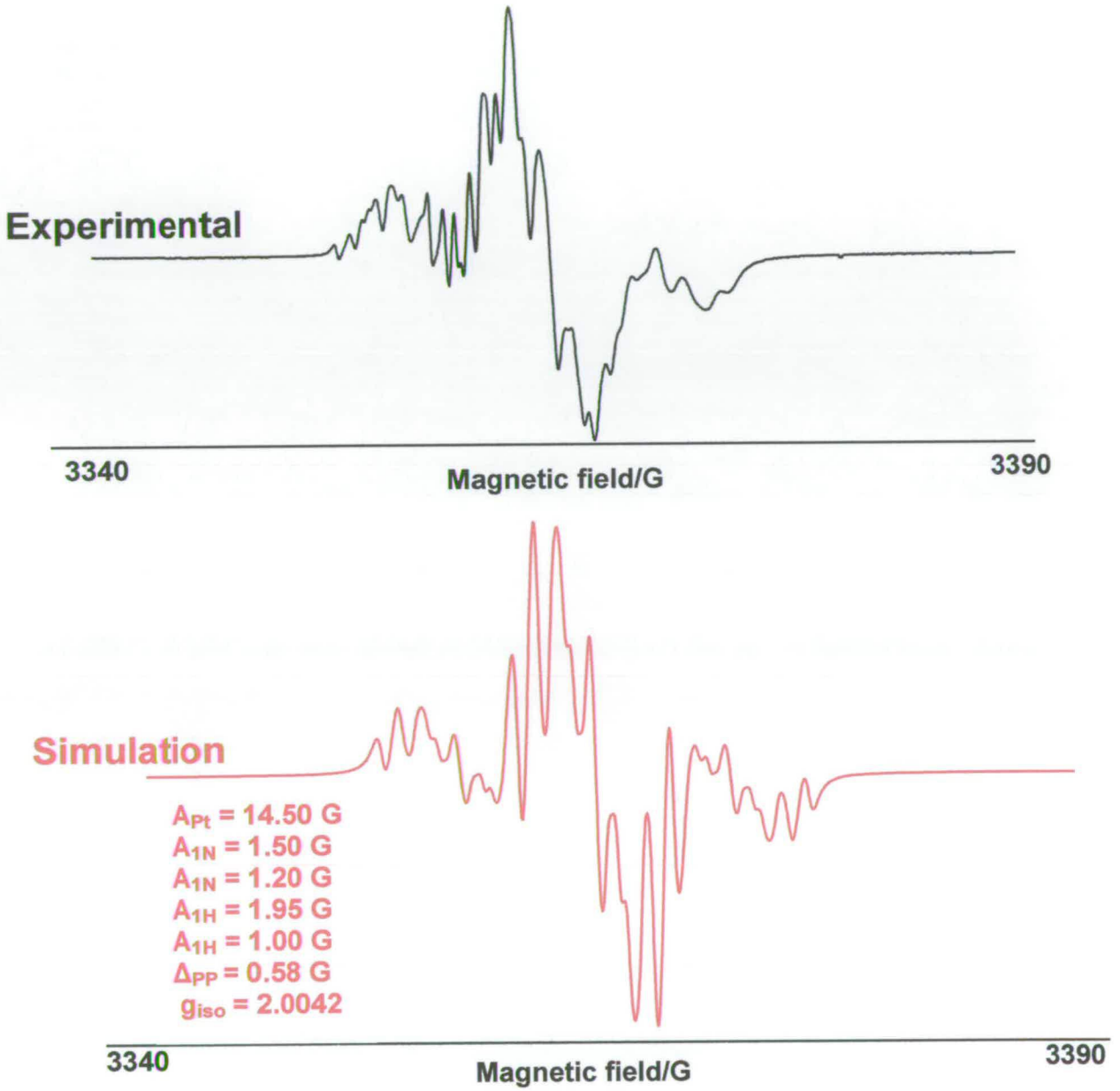

Figure 4.34 Experimental and simulated X-band EPR spectra at 293 K of $[Pt(4–NO_2–4'–Cl–bpy)Cl_2]^{1–}$ generated *in situ* in 0.1 M [TBA][BF_4]/DMF, E_{gen} = –0.88 V, vs. Ag/AgCl.

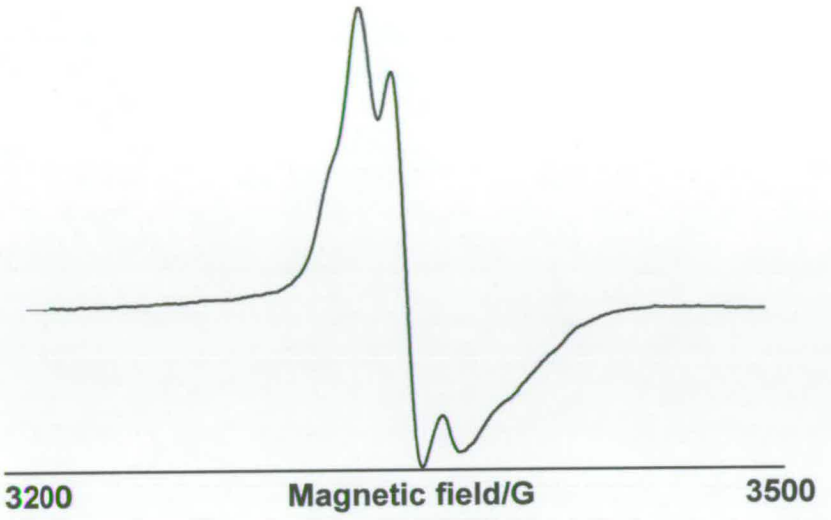

Figure 4.35 Experimental X-band EPR spectrum of $[Pt(4,4'\text{-}(NO_2)_2\text{-}bpy)Cl_2]^{2-}$ generated *in situ* in 0.1 M [TBA][BF_4]/DMF, vs. Ag/AgCl, at 173 K.

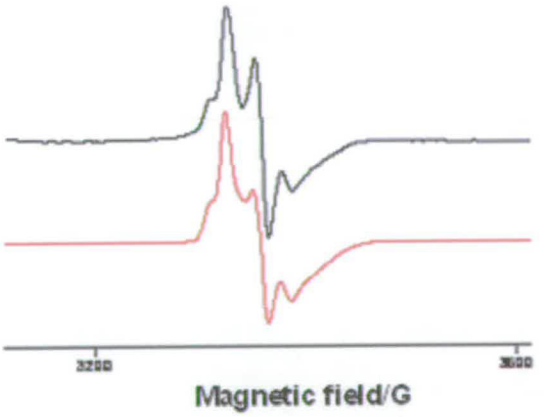

Figure 4.36 Experimental (black) and simulated (red) X-band EPR spectra of $[Pt(4\text{-}NO_2\text{-}4'\text{-}Cl\text{-}bpy)Cl_2]^{1-}$ in 0.1 M [TBA][BF_4]/DMF, at 153 K.

4.6. Conclusions.

Both 4,4′–$(NO_2)_2$–6,6′–Cl_2–bpy and 4,4′–$(NO_2)_2$–bpy undergo two reversible one–electron reductions at –0.48 V and –0.59 V and –0.67 V and –0.79 V, respectively, whereas 4–NO_2–4′–Cl–bpy and 4–NO_2–2–Cl–py undergo one reversible reduction process at –0.68 V and –0.61 V (both followed by an irreversible reduction), respectively.

UV/Vis/nir and EPR spectroelectrochemical studies on the nitro–substituted pro–ligands showed that the two py moieties of the molecule have little communication which means that the electron is localised on the substituted py part of the pro–ligand.

Solvents studies of all nitro substituted 2,2'–bpy and py compounds revealed that there is a solvent dependence. A linear correlation was found between the $E_{½}$ value and the acceptor number of the solvent. The $E_{½}$ value is shifted to more positive values in high acceptor number solvents which will stabilise the negative charge of the reduced molecule.[88] This effect is due to the acidic properties of the solvents surrounding the site where the negative charge is located and thus stabilsies the charged species. UV/Vis/nir and EPR spectroelectrochemical results also show a solvent dependence. However, no quantitative correlation with the solvent parameter could be found.

A triplet spectrum was observed for the EPR spectrum of a frozen solution of the di–reduced species of 4,4′–$(NO_2)_2$–bpy, $[4,4'–(NO_2)_2–bpy]^{2–}$.

$[Pt(4–NO_2–4'–Cl–bpy)Cl_2]$ and $[Pt(4,4'–(NO_2)_2–bpy)Cl_2]$ undergo two reversible one–electron reductions at –0.31 V, –0.81 V and –0.27 V and –0.47 V respectively. No solvent dependence was observed for $[Pt(4–NO_2–4'–Cl–bpy)Cl_2]^{1-}$ and $[Pt(4,4'–(NO_2)_2–bpy)Cl_2]^{2-}$.

UV/Vis/nir and EPR spectroelectrochemical studies of $[Pt(4–NO_2–4'–Cl–bpy)Cl_2]$ and $[Pt(4,4'–(NO_2)_2–bpy)Cl_2]$ indicate that unpaired electrons are ligand based.

5. 5,5′–Disubstituted Bipyridines and Their Complexes With Platinum(II).

5.1. Introduction.

Tuning the photophysical and electrochemical properties of a pro–ligand and any complexes derived from this pro–ligand can be achieved by changing the position or nature of the substituents or by changing the substituents themselves. Past investigations into bpy ligands have focused on di–substituted *tris*-bpy complexes of Ru(II). Such complexes have uses in display devices,[89] as water–oxidation catalysts[90] and as luminescent sensors for organic molecules,[91] metal cations[92] and lanthanides.[93] The chemical and spectral properties of ruthenium bpy complexes have been widely studied, due to their interesting electrochemical properties. They have strong visible absorptions arising from their characteristic MLCT transitions which produce long lived excited triplet states. These excited states have redox chemistries which differ from those of the ground state.[94, 95]

Most work on di–substituted 2,2′–bipyridines has been carried out on the 4,4′ position. This may be due to the difficulty in synthesising the pro-ligands substituted in the 5 and 5′ positions as these positions on 2,2′–bpy are unreactive to electrophilic attack. Nitration at these sites has been reported as unsuccessful.[96,37] Also, it is believed that the 4,4′ positions on di–substituted bpy are electronically the most important sites of substitution. However, Baxter and co–workers concluded that the nitrile substituents in the

5,5′–dicarbonitrile–2,2′–bpy complex exert a greater electron–withdrawing effect upon the metal than in the isomeric 4,4′–dicarbonitrile–2,2′–bpy complex.[39] Furthermore, as has been mentioned in Chapter 1, DFT calculations carried out on 2,2′–bipyridine show that the electron density at the 5,5′ position is significantly greater that at the 4,4′ position. Hence we would expect substitution at the 5,5′ position to have a greater effect on the electronic character of the species than substitution at the 4,4′ position.[98]

5.2. Aims of this Chapter.

The aims of this chapter is to describe the synthesis and electronic characterization of 5,5–$(X)_2$–bpy (where X = (Ph, Br or Cl) and in addition to investigate the properties of their respective Pt complexes. The compounds 5,5′–$(CO_2Et)_2$–bpy and 5,5′–$(CO_2Me)_2$–bpy which have previously been reported [38] were reinvestigated to examine the effect of the solvent on their electronic properties.

5.3. Results and discussion.

5,5′–Br_2–bpy was synthesised as was described previously in section 2.3.1.1, by a coupling of 2,5′–dibromopyridine, yielding 80% of the product. Good CHN, nuclei NMR and mass spectroscopy results were obtained. 5,5′–Ph_2–bpy was synthesised using 5,5′–Br_2–bpy as a starting material, and also gave good CHN, ^{1}H NMR and mass spectroscopy results. 5,5′–Cl_2–bpy was synthesised successfully by the homocoupling reaction of 2–bromo–5–chloropyridine catalyzed by palladium.[48] The succesful synthesis was indicated by CHN, nuclei NMR and mass spectroscopy, see sections 2.3.1., 2.3.1.2., and 2.3.2.

5.3.1. Electrochemistry of 5,5′(X)$_2$–bpy, where X = (Br, Ph, Cl, CO_2Et or CO_2Me).

Cyclic voltammetric studies of the pro–ligands 5,5′(X)$_2$–bpy, where X = (Br, Ph, Cl, CO_2Et or CO_2Me) in 0.1 M [TBA][BF_4]/DMF at 293 K undergo reductive processes, as shown by cyclic voltammetry, see Table 5.1 and Figure 5.1–5.4. The reduction of 5,5′–Br_2–bpy was completely chemically irreversible showing no anodic peak at all temperatures and scan rates studied. Due to the irreversible nature of 5,5′–Br_2–bpy, no further studies were carried out on this molecules. 5,5′–(CO_2Et)$_2$–bpy and 5,5′–(CO_2Me)$_2$–bpy have been studied previously by Jack.[38] These compounds have been reinvestigated in the context of this thesis to examine the effect of changing the solvent on the electrochemical and spectrochemical behaviour of these compounds. Both 5,5′–(CO_2Et)$_2$–bpy and 5,5′–(CO_2Me)$_2$–bpy revealed two fully reversible reductions in 0.1 M [TBA][BF_4]/DMF between −1.25 V and −1.65 V, for each compound. In total two electrons were involved in both these processes and thus each reduction is a one–electron step, see Figure 5.3 and 5.4. 5,5′–Cl_2–bpy has previously been discussed in Chapter 3 of this thesis and therefore will not be discussed in more detail here. Electrochemistry of 5,5′–Ph_2–bpy in 0.1 M [TBA][BF_4]/DMF showed one reversible reduction at −1.75 V, at 293 K.

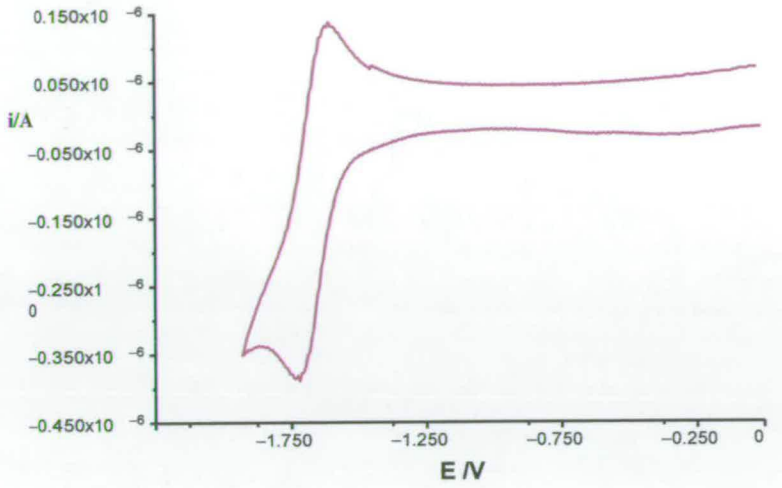

Figure 5.1 Cyclic voltammogram of 5,5′-Ph_2-bpy in 0.1 M [TBA][BF_4]/DMF, vs. Ag/AgCl, scan rate = 0.1 V s^{-1} at 293 K.

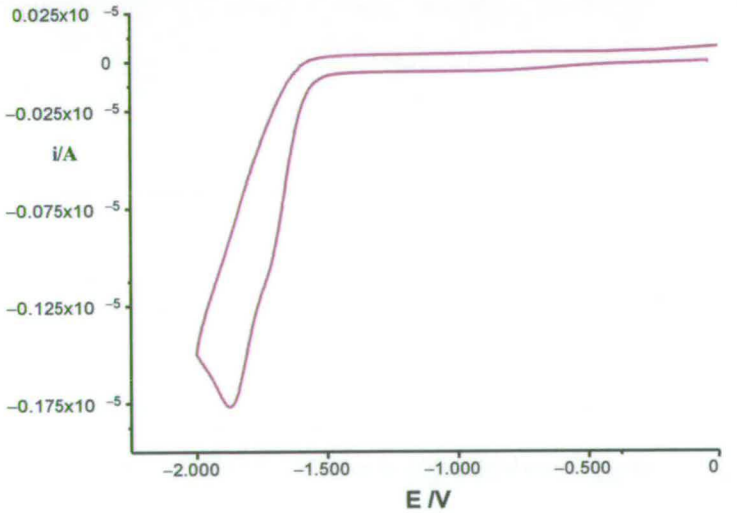

Figure 5.2 Cyclic voltammogram of 5,5′-Br_2-bpy in 0.1 M [TBA][BF_4]/DMF, vs. Ag/AgCl, scan rate = 0.1 V s^{-1} at 293 K.

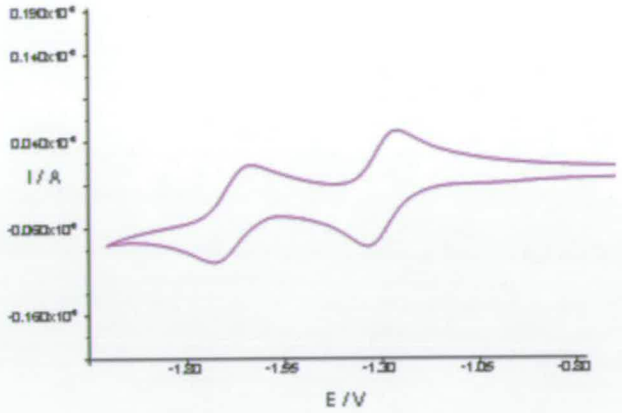

Figure 5.3 Cyclic voltammogram of 5,5′-$(CO_2Et)_2$-bpy in 0.1 M [TBA][BF_4]/DMF, vs. Ag/AgCl, scan rate = 0.1 V s^{-1} at 293 K.

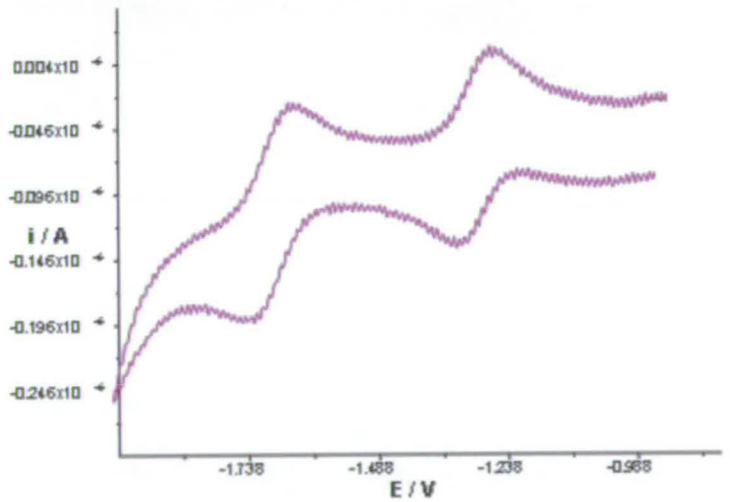

Figure 5.4 Cyclic voltammogram of 5,5′-$(CO_2Me)_2$-bpy in 0.1 M [TBA][BF_4]/DMF, vs. Ag/AgCl, scan rate = 0.1 V s^{-1} at 293 K.

Compound	$E_{½,1}$ /V	$E_{½,2}$ /V
bpy	-2.05	-
5,5′-Ph_2-bpy	-1.75	-
5,5′-Cl_2-bpy	-1.74	-
5,5′-Br_2-bpy	-1.72	-
5,5′-$(CO_2Et)_2$-bpy	-1.25	-1.64
5,5′-$(CO_2Me)_2$-bpy	-1.26	-1.65

Table 5.1 $E_{½}$ values for bpy and 5,5′-$(X)_2$-bpy (where X = Ph, Cl, Br, CO_2Et or CO_2Me) in 0.1 M [TBA][BF_4]/DMF, vs. Ag/AgCl, at 293 K.

The second reduction for 5,5′–$(CO_2Me)_2$–bpy and 5,5′–$(CO_2Et)_2$–bpy were observed at a potential 390 mV more negative than the first. McInnes[31] notes a separation of 490 mV between the first and second reduction potentials of 4,4′–$(CO_2Me)_2$–bpy, which he attributed to the spin pairing of the second electron with the first.[31] Likewise, in this work on 5,5′–$(CO_2Me)_2$–bpy and 5,5′–$(CO_2Et)_2$–bpy, the potential separations can be explained in the same way. In Jack's work carried out on these pro–ligands, the assignment was supported by EPR studies, as the mono–reduced species is paramagnetic but the di–reduced species is shown to be diamagnetic.[38] Therefore, the second electron must be entering the same π^* orbital as the first reduction electron. The electrochemical response of both 5,5′–$(CO_2Me)_2$–bpy and 5,5′–$(CO_2Et)_2$–bpy showed no solvent dependence at all temperatures investigated.

All of the 5,5′–disubstituted bpy compounds studied in this chapter have a more positive first reduction than the 2,2′–bpy itself. This is not surprising since all the substituents are electron withdrawing compared to H. A graph of the Hammett parameter of the substituent (a measure of the substituent strength) *vs* electrode potential shows a good linear correlation (Figure 5.5, point 6 obtained from Jack[38]).

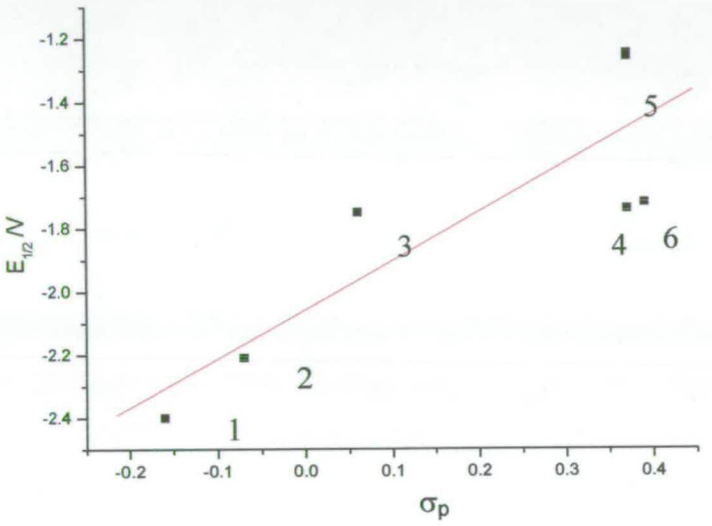

Figure 5.5 Plot of $E_{½}$ of first reduction of 5,5′–$(X)_2$–bpy *vs.* Hammett parameter σ_m of the substituent X, (where X = 1) NH_2, 2) Me, 3) Br, 4) Ph, 5) CO_2Et or CO_2Me, 6) Cl. (Me, NH_2)

5.3.1.1. UV/Vis/nir Spectroelectrochemistry of 5,5′$(X)_2$–bpy, where X = (Br, Ph, CO_2Et or CO_2Me).

The electrochemical response of 5,5′–$(CO_2Et)_2$–bpy was invariant with solvent. However, it was decided to study the UV/Vis spectroelectrochemical response of 5,5′–$(CO_2Et)_2$–bpy in different solvents since UV/Vis spectroscopy is more sensitive

than cyclic voltammetry. The spectroelectrochemical studies of 5,5′–$(CO_2Et)_2$–bpy were carried out in DMF, CH_3CN and CH_2Cl_2 at 233 K, see Figure 5.6–5.8.

The spectrum of the neutral molecule, (blue spectrum in Figure 5.6–5.8) was dominated by a broad band in the UV region at approximately 33, 000 cm^{-1} and was assigned to a $\pi \rightarrow \pi^*$ transition. This peak is at lower energy than the corresponding $\pi \rightarrow \pi^*$ transition for un–substituted bpy (35,300 cm^{-1}) due to the electron withdrawing character of the ester group. In CH_3CN and CH_2Cl_2 a higher energy $\pi \rightarrow \pi^*$ transition was observed at around 39,000 cm^{-1}. The spectrum of the mono–reduced species $[5,5'–(CO_2Et)_2–bpy]^{1-}$, (red spectrum in Figure 5.6–5.8) has three bands around 13,000, 23,000 and 33,000 cm–1 in agreement with the UV/Vis/nir spectra of other mono–reduced bpy pro–ligands. Thus, the bands in the reduced anion were assigned to electronic transitions from the SOMO to higher energy LUMOs. The fine structure observed on the nir and Vis bands is due to vibronic coupling of the aromatic molecule. Comparison of the UV/Vis/nir spectrum of $[5,5'–(CO_2Et)_2–bpy]^{1-}$ in different solvents showed only very minor shifts in band positions which is in agreement with the solvent independent electrochemical behaviours, see Table 5.2. The di–reduced species $[5,5'–(CO_2Et)_2–bpy]^{2-}$ showed a very intense band around 19,000 cm^{-1} in DMF and CH_3CN with a further band around 23,000 cm^{-1}. The spectrum of bpy^{2-} has two visible absorption bands as measured by König and Kremer.[86] Therefore, the bands in the spectrum of $[5,5'–(CO_2Et)_2–bpy]^{2-}$ may be assigned to transitions from the doubly occupied LUMO to higher energy unoccupied π^* anti–bonding orbitals. The spectrum of the direduced compound in DCM has bands in

similar positions to those in CH_3CN and DMF but were much less well resolved, because the di–reduced species was much less soluble in DCM compared to the mono–reduced species and the di–reduced species in MeCN or DMF. Table 5.2 shows the peak positions for 5,5′–$(CO_2Et)_2$–bpy and its reduced species in different solvents.

Species	ν (0.1 M [TBA][BF_4]/DMF) /cm^{-1} (ε/$M^{-1}cm^{-1}$)	ν (0.1 M [TBA][BF_4]/MeCN) /cm^{-1} (ε/$M^{-1}cm^{-1}$)	ν (0.3 M [TBA][BF_4]/DCM) /cm^{-1} (ε/$M^{-1}cm^{-1}$)
5,5′-$(CO_2Et)_2$-bpy	32,800 (29 330)	33,130 (32 300)	32,900 (32 050)
		39,100 (17 300)	38,900 (16 200)
		40,000 (15 960)	39,850 (14 860)
[5,5′-$(CO_2Et)_2$-bpy]$^{1-}$	12,150 (10 340)	12,300 (14 250)	12,200 (11 700)
	13,000 (17 220)	13,160 (25 020)	13,090 (20 600)
	13,940 (11 540)	14,500 (17 350)	14,400 (14 160)
	14,400 (11 580)	22,330 (64 200)	22,200 (49 470)
	22,220 (45 420)	23,030 (33 910)	24,000 (22 280)
	22,920 (23 460)	24,140 (27 670)	33,120 (10 100)
	24,000 (19 500)	33,450 (7 700)	39,650 (8920)
	33,220 (11 510)	39,380 (8890)	

Table 5.2 The peak positions for 5,5′-$(CO_2Et)_2$-bpy and [5,5′-$(CO_2Et)_2$-bpy]$^{1-}$ in different solvents.

The UV/Vis/nir spectrum of 5,5′–Ph_2–bpy showed an intense energy band at *ca.* 31 kcm^{-1}, see Figure 5.9 and 5.10 which was assigned as an bpy $\pi \rightarrow \pi^*$ transition. This peak was at lower energy than the corresponding $\pi \rightarrow \pi^*$ transitions for unsubstituted bpy (35,300 cm^{-1}, ε = 12,900 M^{-1} cm^{-1}), as electron withdrawing groups on the 5,5′–positions stabilize the LUMO with respect to bpy. The reduction potential of

5,5′–Ph_2–bpy was observed at less negative potential than the first reduction of bpy in agreement with this. The applied potential across the working electrode/solution interface in the OTTLE cell was set to –2 V to generate the mono–reduced species. On reduction of the species, the band at 30,900 cm^{-1} collapsed to ε = 6, 7000 $M^{-1}cm^{-1}$ and another two bands grew in, see Figure 5.10. Upon reduction of 5,5′–Ph_2–bpy to $[5,5'–Ph_2–bpy]^{1-}$, the spectrum revealed three bands: one centred around *ca.* 11,000 cm^{-1}, a visible band around *ca.* 21,000 $cm^{-1}$and a UV band at *ca.* 31,000 cm^{-1}. The positions of these bands are similar to the positions of the bands shown in the spectrum of the mono–reduced species of bpy and 5,5′–$(CO_2Et)_2$–bpy. Therefore, it can be inferred that the electronic character of the frontier orbitals of bpy and 5,5′–Ph_2–bpy are similar *i.e.* that the LUMO on the molecule is primarily based on the bpy part of the molecule. The nir band at *ca.* 11–12 kcm^{-1} can be assigned as SOMO to LUMO–1 transitions.[99]

Table 5.3 shows the peak positions and corresponding molar extinction coefficients, ε, of the spectrum of 5,5′–Ph_2–$bpy^{0/1-}$ in 0.1 M [TBA][BF_4]/DMF at 233 K. The energies of the bands in the spectrum of $[5,5'–Ph_2–bpy]^{1-}$ are in between analogous bands in the spectra of bpy^{1-} and $[5,5'–(CO_2Et)_2–bpy]^{1-}$ which is entirely as expected since the electronic properties of Ph are in between those of H and CO_2Et.

Species	ν /cm^{-1} (ε/M^{-1}cm^{-1})
5,5′-Ph_2-bpy	30,900 (32,500)
[5,5′-Ph_2-bpy]$^{1-}$	10,700 (22,700)
	12,000 (15,400)
	20,200 (32,300)
	22,000 (26,300)
	31,400 (6,740)

Table 5.3 The peak positions for 5,5′-Ph_2-bpy and [5,5′-Ph_2-bpy]$^{1-}$ in 0.1 M [TBA][BF_4]/DMF at 233 K.

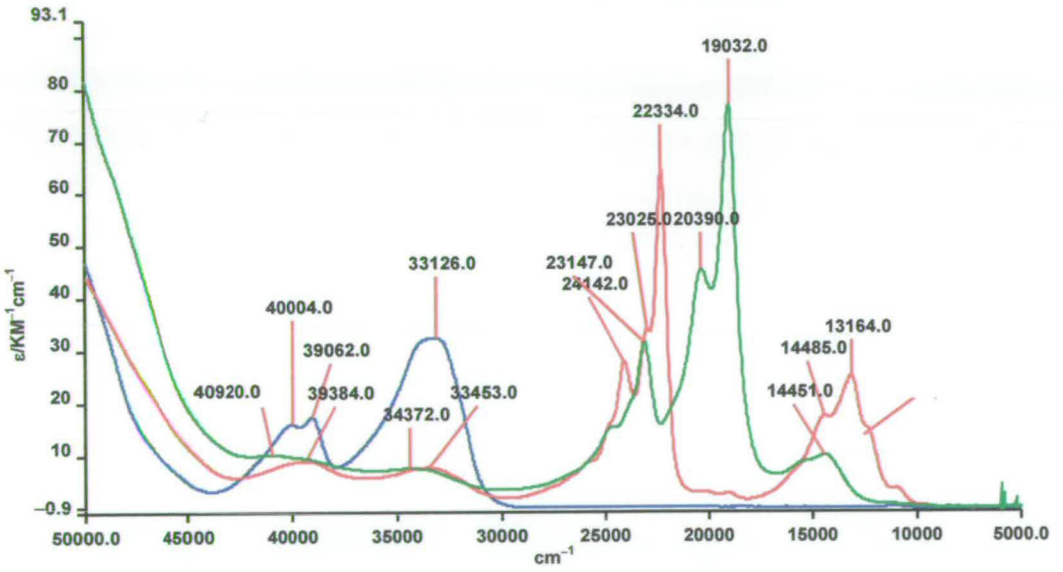

Figure 5.6 UV/Vis/nir spectra of 5,5′–$(CO_2Et)_2$–bpy (blue), [5,5′–$(CO_2Et)_2$–bpy]$^{1-}$(red) and [5,5′–$(CO_2Et)_2$–bpy]$^{2-}$(green) in 0.1 M [TBA][BF_4]/DMF at 233 K.

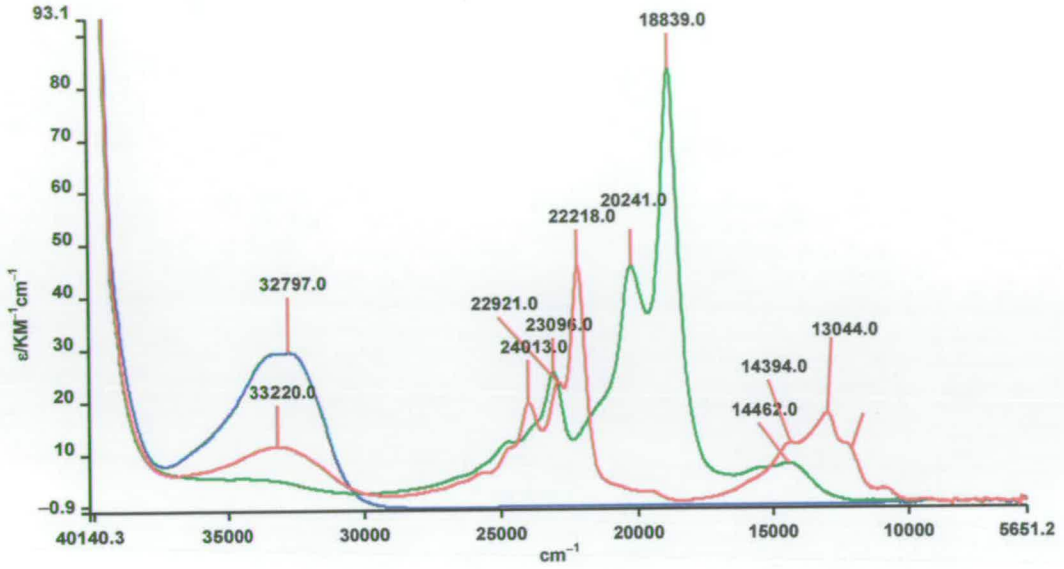

Figure 5.7 UV/Vis/nir spectra of 5,5′–$(CO_2Et)_2$–bpy (blue), $[5,5'–(CO_2Et)_2–bpy]^{1-}$ (red) and $[5,5'–(CO_2Et)_2–bpy]^{2-}$ (green) in 0.1 M [TBA][BF_4]/MeCN at 233K.

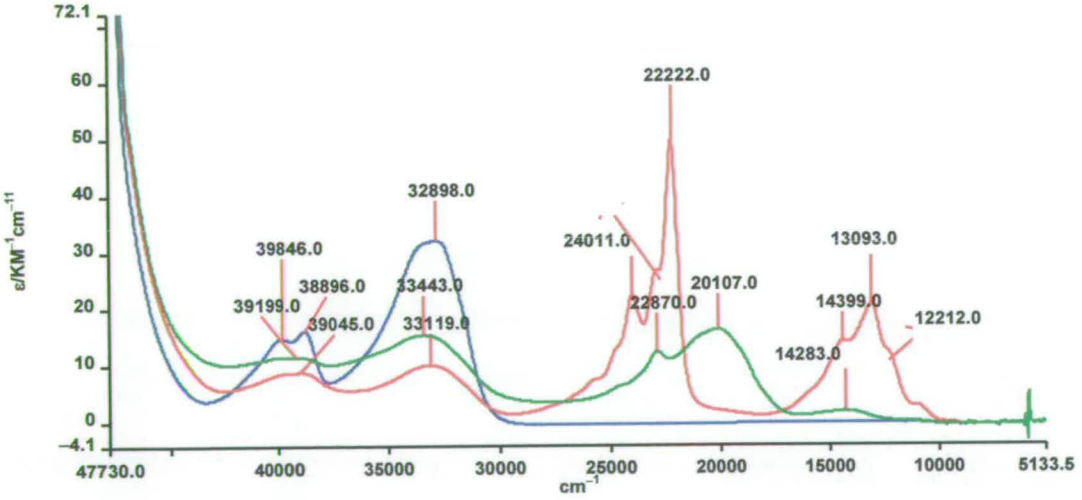

Figure 5.8 UV/Vis/nir spectra of 5,5′–$(CO_2Et)_2$–bpy (blue), $[5,5'–(CO_2Et)_2–bpy]^{1-}$ (red) and $[5,5'–(CO_2Et)_2–bpy]^{2-}$ (green) in 0.3 M [TBA][BF_4]/DCM at 233 K.

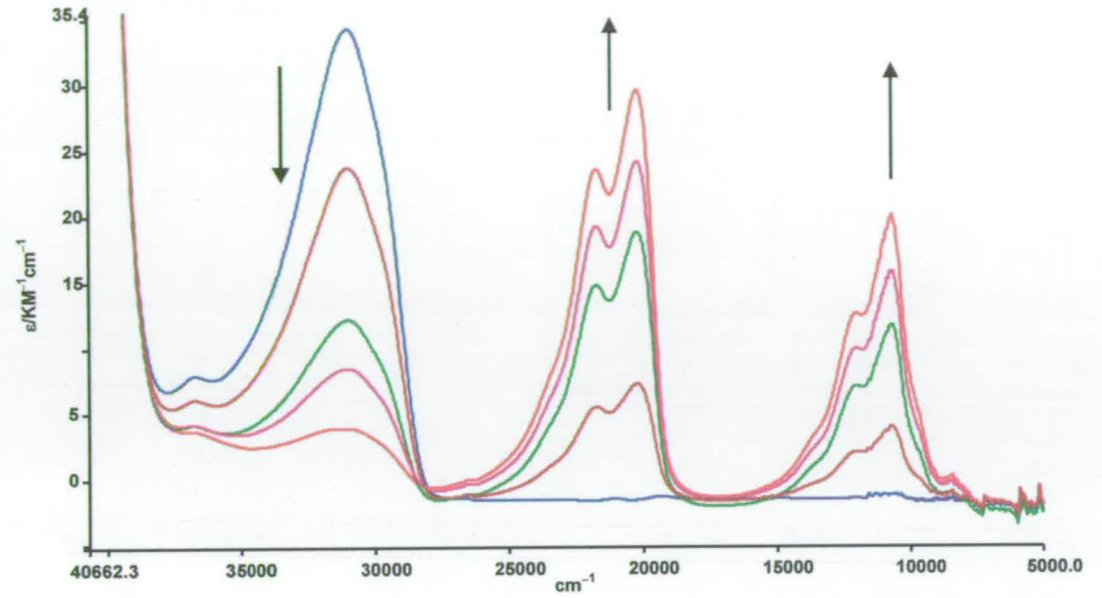

Figure 5.9 UV/Vis/nir spectra of 5,5′–Ph_2–bpy (blue) and $[5,5'–Ph_2–bpy]^{1-}$ (red) in 0.1 M $[TBA][BF_4]$/DMF, showing partially reduced curves, at 233 K.

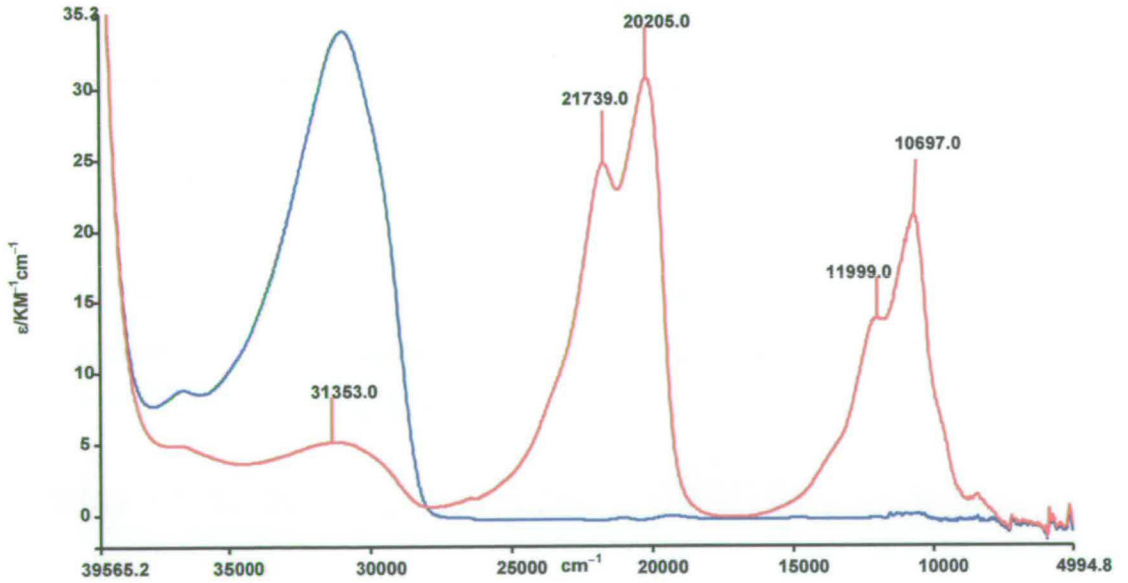

Figure 5.10 UV/Vis/nir spectra of 5,5′–Ph_2–bpy (blue) and $[5,5'–Ph_2–bpy]^{1-}$ (red) in 0.1 M $[TBA][BF_4]$/DMF at 233 K.

5.3.1.2. EPR of $[5,5'–Ph_2–bpy]^{1–}$.

UV/Vis/nir spectrochemical study on $[5,5'–Ph_2–bpy]^{1–}$ indicated that the molecular orbital occupied by the unpaired electron was delocalaised over the bpy molecule. The X-band EPR spectroelectrochemical investigation on other 5,5′–disubstituted bpy pro–ligands (NO_2, CO_2Et or CO_2Me) was in agreement that the electron density in the LUMO of 5,5′–disubstituted bpy pro–ligands was spread over both py rings. It was therefore anticipated that successful interpretation of the EPR spectrum of $[5,5'–Ph_2–bpy]^{1–}$ would follow similar arguments. CAChe calculations, see section 2.7, indicate that the LUMO of 5,5′–Ph_2–bpy is primarily based on the two py rings (85 %) with largest contributions from the 2,2′ and 5,5′ carbon atoms which are EPR silent followed by the N nuclei and the 4,4′ carbons as it is shown in Figure 5.11.

Figure 5.11 LUMO of 5,5′-Ph_2-bpy using Molecular Orbital calculations (CAChe)

The experimental X–band EPR spectrum and its simulation as shown in Figure 5.12. The best fit simulation was achieved by coupling the unpaired electron to two equivalent nitrogen nuclei (2.9 G) and two equivalent protons (7.0 G). Thus, the semi–occupied MO

in $[5,5'–Ph_2–bpy]^{1-}$ is delocalised over the two py rings. The coupling constant to the equivalent N nuclei in $[5,5'–(CO_2Me)_2–bpy]^{1-}$ is 1.05 G.[38] Since CO_2Me is a significantly better electron withdrawing group compared to Ph, the increase in a^N on going from $[5,5'–(CO_2Me)_2–bpy]^{1-}$to $[5,5'–Ph_2–bpy]^{1-}$ is as expected (2.900 G compared to 1.05 G). The large coupling to two equivalent protons in $[5,5'–Ph_2–bpy]^{1-}$ is assumed to be the protons in the 4,4′–position since electrochemically this is known to be an important position.

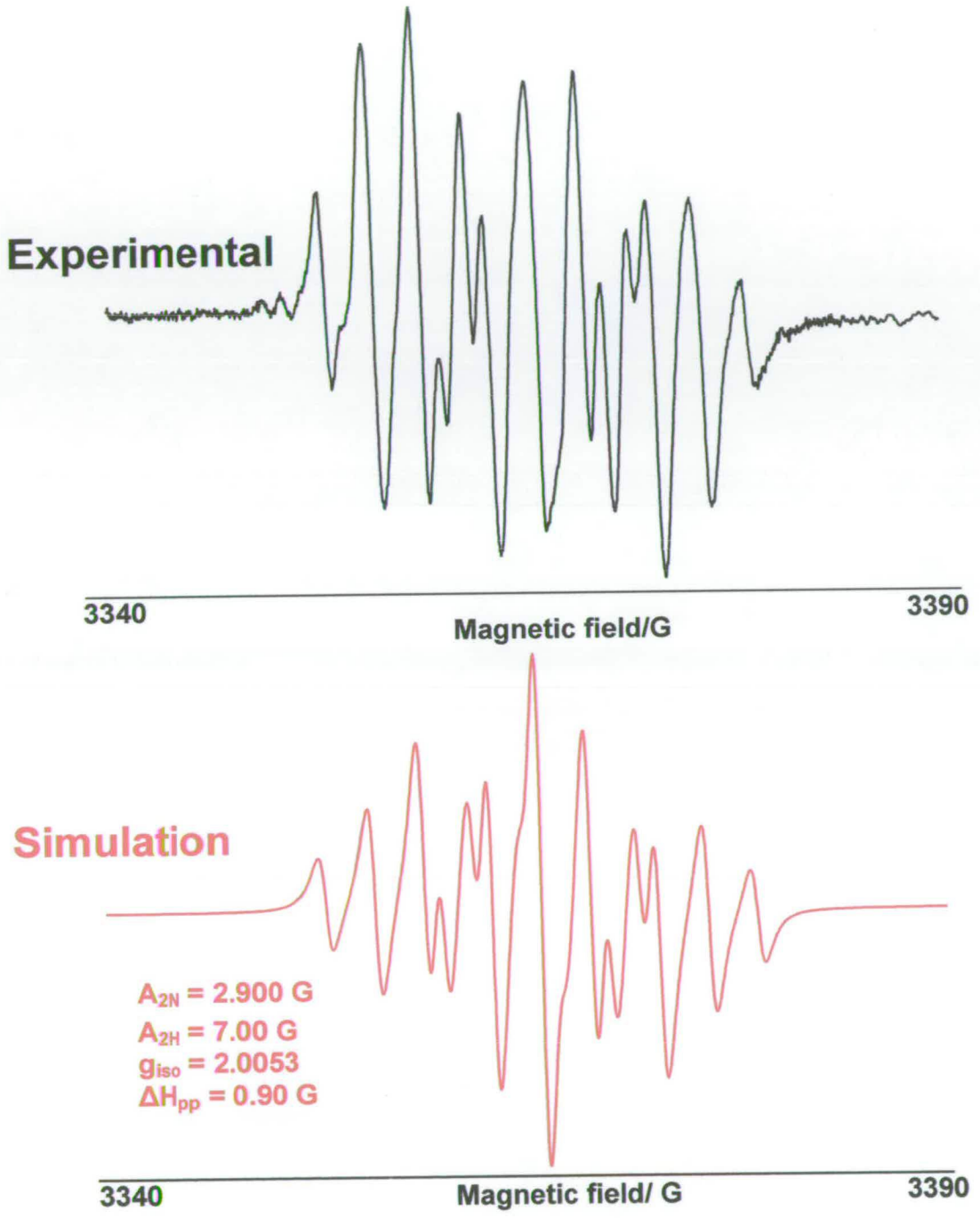

Figure 5.12 Experimental and simulated X-band EPR spectra of $[5,5'\text{-}Ph_2\text{-}bpy]^{1-}$ in 0.1 M $[TBA][BF_4]$/DMF, vs. Ag/AgCl, at 233 K.

5.4. [Pt(5,5′–(X)$_2$–bpy)Cl$_2$], (Where X = CO_2Et, CO_2Me, Br or Ph).

[Pt(5,5′–(X)$_2$–bpy)Cl$_2$] (X = Br, Cl or Ph) were prepared by the following general procedure, see section 2.4. A suspension of the appropriate ligand was heated in H_2O under reflux with $K_2[PtCl_4]$ and recrystallised from hot *N,N′*–dimethylformamide. The syntheses were all successful as was indicated by CHN and mass spectroscopy results.

5.4.1. Electrochemistry of [Pt(5,5'–(X)$_2$–bpy)Cl$_2$], (where X is CO_2Et, CO_2Me, Br or Ph).

Cyclic voltammetry of [Pt(5,5′–(X)$_2$–bpy)Cl$_2$] in 0.1M [TBA][BF_4]/DMF (where X is CO_2Et, CO_2Me or Ph) showed two reversible reductions at –0.54 V and –1.03 V , –0.52 V and –1.01 V, and –0.93 V and –1.51 V, respectively. In contrast [Pt(5,5′–Br_2–bpy)Cl_2] and [Pt(5,5′–Cl_2–bpy)Cl_2] showed one reversible reduction at –0.80 V and –0.83 V, respectively in 0.1 M [TBA][BF_4]/DMF, see Figure 5.13 –5.16.

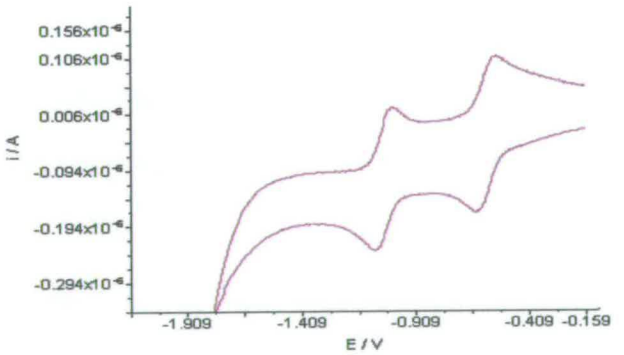

Figure 5.13 Cyclic voltammogram of [Pt(5,5′-(CO_2Et)$_2$-bpy)Cl_2] in 0.1 M [TBA][BF_4]/DMF , vs. Ag/AgCl, at 293 K, scan rate 0.1 Vs^{-1}.

In all cases binding of the ligand to the Pt(II) metal centre results in a shift of the reduction potentials to less negative potentials compared to those of the free ligand. This is primarily caused by the positive charge on the metal centre. The difference in potential between the two reduction peaks, approximately 500 mV, is indicative of spin pairing, that is, both reduction electrons enter the same ligand–based orbital. The diamagnetic nature of the direduced species confirmed by EPR is in agreement with this proposal.

The redox behaviour of [Pt(5,5′–$(CO_2Et)_2$–bpy)Cl_2] has been studied in a variety of solvents and at different temperatures. No solvent effect was observed for the electrochemical behaviour of [Pt(5,5′–$(CO_2Et)_2$–bpy)Cl_2].

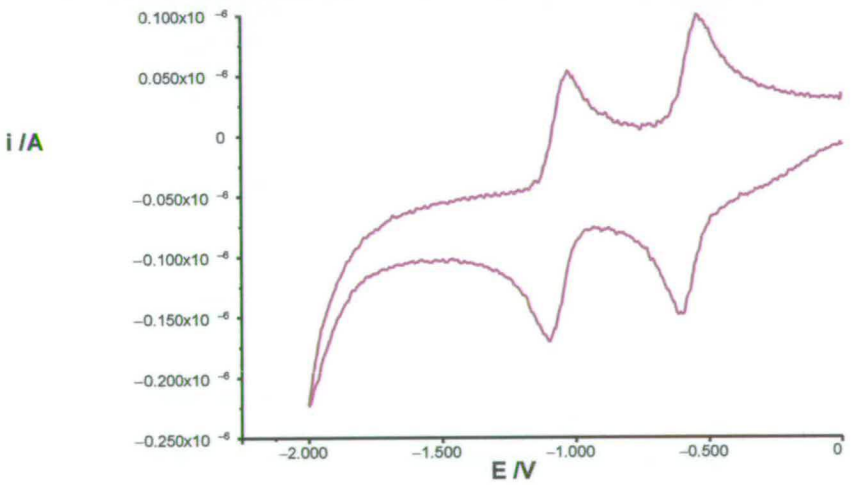

Figure 5.14 Cyclic voltammogram of [Pt(5,5′-$(CO_2Me)_2$-bpy)Cl_2] in 0.1 M [TBA][BF_4]/DMF , vs. Ag/AgCl, at 293 K, scan rate 0.1 Vs^{-1}.

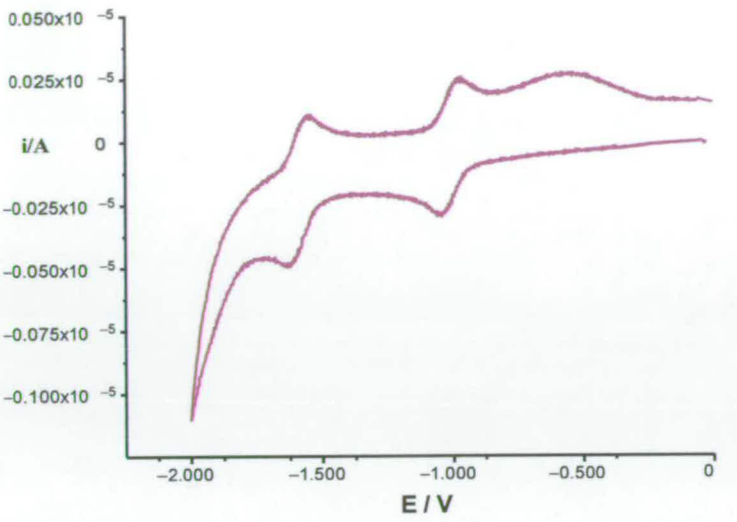

Figure 5.15 Cyclic voltammogram of [Pt(5,5′-Ph_2-bpy)Cl_2] in 0.1 M [TBA][BF_4]/DMF, vs. Ag/AgCl, at 293 K, scan rate 0.1 Vs^{-1}.

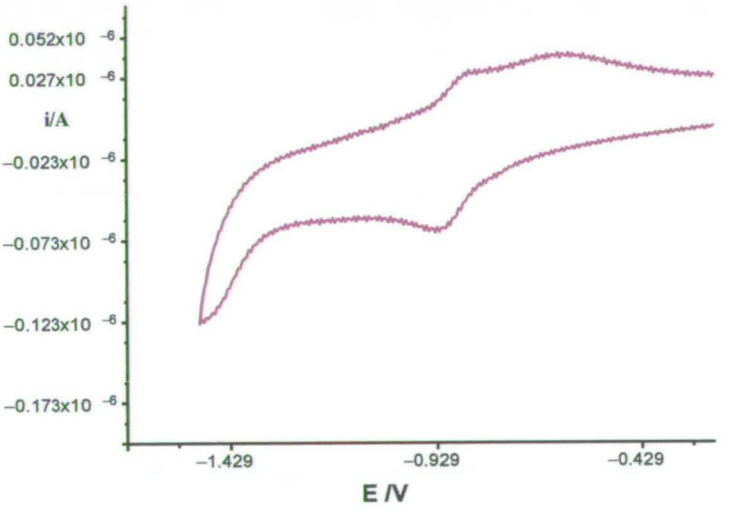

Figure 5.16 Cyclic voltammogram of [Pt(5,5′-Br_2-bpy)Cl_2] in 0.1 M [TBA][BF_4]/DMF, vs. Ag/AgCl, at 293 K, scan rate 0.1 Vs^{-1}.

5.4.2. Spectroelectrochemistry.

5.4.2.1. UV/Vis/nir Spectroelectrochemistry of [Pt(5,5'–$(X)_2$–bpy)Cl_2] (Where X = CO_2Et, CO_2Me,Br or Ph).

The UV/Vis/nir spectroelectrochemical responses of [Pt(5,5′–$(CO_2Et)_2$–bpy)Cl_2] and [Pt(5,5′–$(CO_2Me)_2$–bpy)Cl_2] in 0.1 M [TBA][BF_4]/DMF are very similar, see Figure 5.17 and 5.18, respectively. The spectrum of [Pt(5,5′–$(CO_2Et)_2$–bpy])$Cl_2]^0$ in 0.1 M [TBA][BF_4]/DMF is shown in Figure 5.17. The bands at 29,400 cm^{-1} (6890 $M^{-1}cm^{-1}$), 30,480 cm^{-1} (60350 $M^{-1}cm^{-1}$) and 33,800 cm^{-1} (11400 $M^{-1}cm^{-1}$) were assigned as $\pi \rightarrow \pi^*$ (bpy) intraligand transitions whilst the band at 23,800cm^{-1} was a charge transfer band involving the Pt(II) centre. On reduction to [Pt(5,5′–$(CO_2Et)_2$–bpy)$Cl_2]^{1-}$ bands at 36,232 cm^{-1} (7000 $M^{-1}cm^{-1}$), 32,060 cm^{-1} (6354 $M^{-1}cm^{-1}$), 24,875 cm^{-1} (11628 $M^{-1}cm^{-1}$) and 15,914 cm^{-1}(5352 $M^{-1}cm^{-1}$) grew in. Assignment of the absorption bands to specific electronic transitions is made easier by comparing the spectra of the mono and di–reduced Pt complex with those of the mono and di–reduced free ligand. The bands in the reduced free ligand may be assigned to intraligand charge transfer transitions within the reduced ligand. In the reduced Pt(II) complexes similar bands are observed and hence were also assigned to interligand charge transfers within the reduced 5,5′–(CO_2R)–bpy (R= Me or Et) pro–ligands. The intraligand bands are all blue shifted (moved to higher energy) in the reduced spectra of the Pt complexes compared to the free ligand. In addition, the close resemblance of the spectra of reduced free and bound ligand suggests

that the orientation of the reduced free ligand is similar to that in its bound state, that is a planar arrangement. On reduction to $[Pt(5,5'–(X)_2–bpy)Cl_2]^{2-}$ (where X= CO_2Me or CO_2Et) similar spectra were observed with an intense doublet growing in at 20,745 cm^{-1} (40073 $M^{-1}cm^{-1}$) and 22,270 cm^{-1} (19025 $M^{-1}cm^{-1}$) and 20,790 cm^{-1} (61690 $M^{-1}cm^{-1}$) and 22,307 cm^{-1} (29499 $M^{-1}cm^{-1}$) for $[Pt(5,5'–(CO_2Et)_2–bpy)Cl_2]^{2-}$ and $[Pt(5,5'–(CO_2Me)_2–bpy)Cl_2]^{2-}$, respectively.

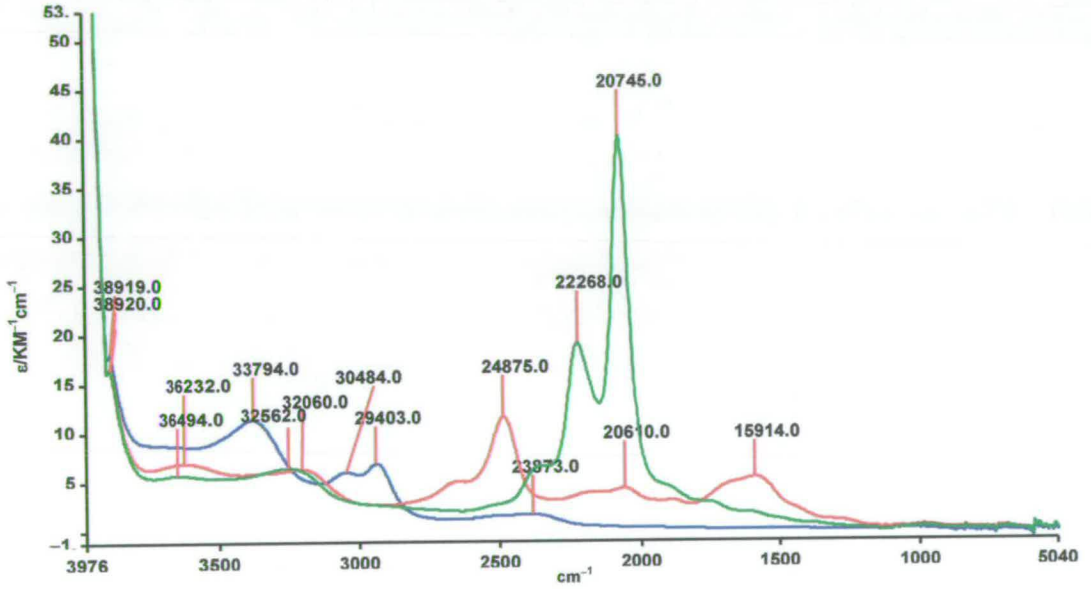

Figure 5.17 UV/Vis/nir spectra of $[Pt(5,5'–(CO_2Et)_2–bpy)Cl_2]$ (blue), $[Pt(5,5'–(CO_2Et)_2–bpy)Cl_2]^{1-}$ (red) and $[Pt(5,5'–(CO_2Et)_2–bpy)Cl_2]^{2-}$ (green) in 0.1 M $[TBA][BF_4]$/DMF at 233 K.

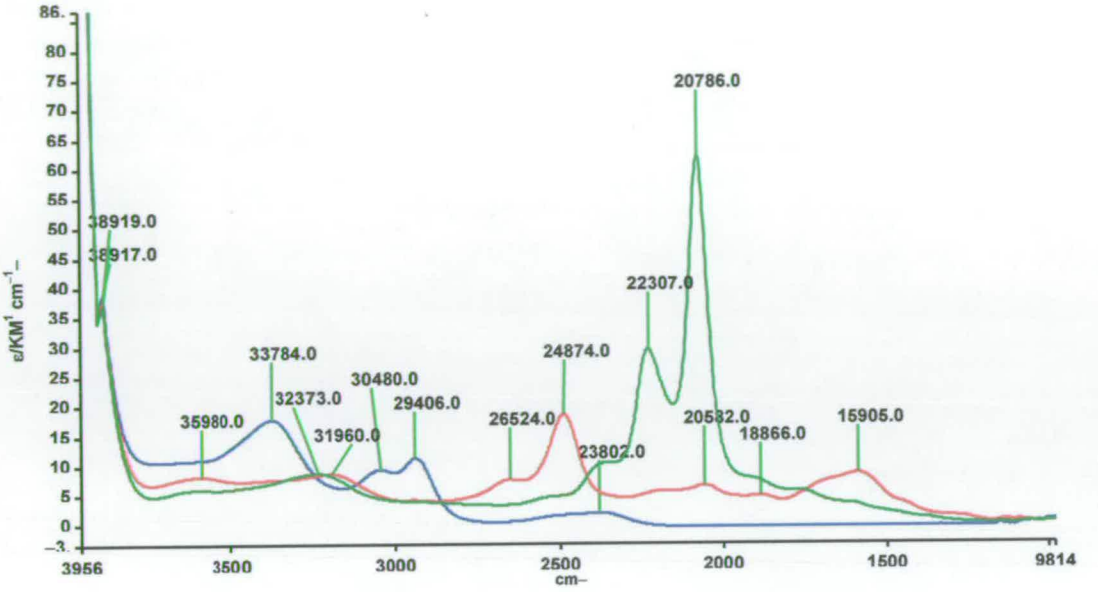

Figure 5.18 UV/Vis/nir spectra of $[Pt(5,5'–(CO_2Me)_2–bpy)Cl_2]$ (blue), $[Pt(5,5'–(CO_2Me)_2–bpy)Cl_2]^{1-}$ (red) and $[Pt(5,5'–(CO_2Me)_2–bpy)Cl_2]^{2-}$ (green) in 0.1 M [TBA][BF_4]/DMF at 233K.

During the conversion between $[Pt(5,5'–(X)_2–bpy)Cl_2]^{1-}$ and $[Pt(5,5'–(X)_2–bpy)Cl_2]^{2-}$ (X = CO_2Et or CO_2Me) the bands around 16 and 25 kcm^{-1} collapsed while the bands between 20–22 kcm^{-1} grew. Jack[38] reported that the intense peaks are assigned as intraligand transitions from the occupied LUMO to empty π^* orbitals, thus, there is a similarity between the electronic character of the frontier orbitals in all four cases. This implies that the redox–active orbital on $[Pt(5,5'–(X)_2–bpy)Cl_2]^{1-}$ (where X= CO_2Me or CO_2Et) is based primarily on the bpy part of the molecule just as it is in the free ligand, according to the similarity between the UV/Vis/nir spectral results of the $[5,5'–(CO_2Me)_2–bpy]^{1-}$, $[5,5'–(CO_2Et)_2–bpy]^{1-}$ and their corresponding mono–reduced Pt complexes.

In all cases the electrode potential was switched back to 0 V after study at negative potentials. This ensured that there was no following chemical reactions and the species are stable at 233 K since each spectrum returned to its original.

The UV/Vis/nir spectra of $[Pt(5,5'-(CO_2Et)_2-bpy)Cl_2]$ and $[Pt(5,5'-(CO_2Me)_2-bpy)Cl_2]$ in 0.1 M $[TBA][BF_4]$/DMF were very similar, see Figures 5.17 and 5.18. That is not surprising since the methyl group is replaced by an ethyl group. Again a similar spectrum is observed for $[Pt(5,5'-Ph_2-bpy)Cl_2]$ in 0.1 M $[TBA][BF_4]$/DMF, see Figure 5.19. The spectrum of the neutral species showed two bands at high energy 32,800 cm^{-1} (ε = 23,070 $M^{-1}cm^{-1}$) and 27,300 cm^{-1} (ε = 27,200 $M^{-1}cm^{-1}$). These were assigned to $\pi \rightarrow \pi^*$ transitions. Holding the potential at −1.41 V to generate the mono–reduced species results in the collapsed of the high energy bands of the parent species and the growth of three new bands at 24,900 cm^{-1} (ε = 14,800 $M^{-1}cm^{-1}$), 20,000 cm^{-1} (ε = 27,200 $M^{-1}cm^{-1}$) and 14,900 cm^{-1} (ε = 10,200 $M^{-1}cm^{-1}$). Comparison of the spectrum of $[Pt(5,5'-Ph_2-bpy)Cl_2]^{1-}$ and $(5,5'-Ph_2-bpy)^{1-}$ showed similarities with the intraligand reduced bpy–based bands, once again moved to higher energy. There is an additional band at 20,000 cm^{-1} and its electronic origin is uncertain. However, the spectrum obtained is similar to that of bpy^{1-}, therefore, the transitions are assigned as for mono–reduced bpy.

In an attempt to generate the di–reduced species of $[Pt(5,5'–Ph_2–bpy)Cl_2]^{2-}$ the potential was held at –1.86 V and all the bands in the mono–reduce spectrum collapsed apart from a peak at 29,700 cm^{-1} (ε = 15,300 $M^{-1}cm^{-1}$) and an intense band grew in at 16,200 cm^{-1} (ε = 46,990 $M^{-1}cm^{-1}$). Once again the spectra of $(bpy)^{2-}$ and $[5,5'–Ph_2–bpy]^{2-}$ show very similar features. The intense peak can be assigned as an intraligand transition from the fully occupied LUMO to an empty π^*orbital. This assignment was confirmed by the similarity between the spectra of $[Pt(5,5'–Ph_2–bpy)Cl_2]^{2-}$ and $[Pt(5,5'–(X)_2–bpy)Cl_2]^{2-}$, (X = CO_2Et or CO_2Me). Thus the reduced species may be formulated as $[Pt(II)(5,5'–Ph_2–bpy^{1-})\ Cl_2]^{1-}$ and $[Pt(II)(5,5'–Ph_2–bpy^{2-})Cl_2]^{2-}$.

For $[Pt(5,5'–Br_2–bpy)Cl_2]$ several peaks were observed in UV/Vis/nir spectrum. The spectrum showed UV transitions at 36,600 cm^{-1}(ε = 7,900 $M^{-1}cm^{-1}$), 34,300 cm^{-1} (ε = 8,500 $M^{-1}cm^{-1}$), 30,000 cm^{-1} and 28,900 cm^{-1} (ε = 5,500 and 7,200 $M^{-1}cm^{-1}$), respectively. These have been assigned as $\pi \rightarrow \pi^*$ (bpy) intraligand transitions. A peak at 25,400 cm^{-1} (ε = 2,600 $M^{-1}cm^{-1}$) was assigned as a MLCT ($d \rightarrow \pi^*$) transitions in line with related complexes such as $[Pt(5,5'–Cl_2–bpy)Cl_2]$, see section 3.3.2.2. The mono–reduced species was generated by holding the potential at –1.50 V and the spectrum showed absorptions at 21,900 cm^{-1}, 27,900 cm^{-1} and 29,600 cm^{-1} (ε = 6,600, 7,600 and 8,000 $M^{-1}cm^{-1}$), respectively. In addition there was a broad low energy band absorption which accounts for the red reduced trace lying higher than the neutral blue spectrum in Figure 5.20. Unfortunately, the mono–reduced free ligand was not stable and therefore direct comparison of the reduced free ligand and Pt(II) bound ligand is not

possible. However, it is anticipated that the electron will enter a molecular orbital spanning both py rings. Thus the absorption bands in $[Pt(5,5'–Br_2–bpy)Cl_2]^{1-}$ are observed in general agreement with ligated bpy ligands, that is, a broad nir band, a visible band around 21,000 cm^{-1} and a UV band at around 28,00 cm^{-1}. On reduction of $[Pt(5,5'–Br_2–bpy)Cl_2]$ to $[Pt(5,5'–Br_2–bpy)Cl_2]^{1-}$ the unpaired electron enters the LUMO and leads to a decrease in the energy of this orbital. In line with this, the HOMO to SOMO transition drops in energy compared to the neutral species to give a transition at 29,600 cm^{-1} transition. The other bands on the mono–reduced species can be assigned as intraligand transition from the occupied LUMO to empty π^*orbitals. Hence, the same conclusion can be made for the electron reduction, that is, it must localised on the whole bpy moiety. Therefore the reduced species can be formulated as $[Pt(II)(5,5'–Br_2–bpy)^{1-}Cl_2]^{1-}$. Again the potential was returned to 0 V to confirm the reversibility of the process and the spectrum went back to its original.

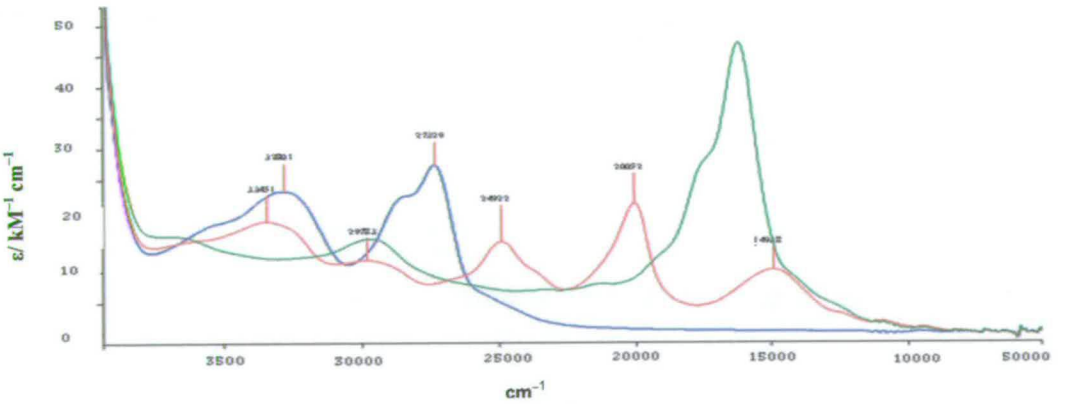

Figure 5.19 UV/Vis/nir spectra of $[Pt(5,5'–Ph_2–bpy)Cl_2]^0$ (blue), $[Pt(5,5'–Ph_2–bpy)Cl_2]^{1-}$ (red) and $[Pt(5,5'–Ph_2–bpy)Cl_2]^{2-}$ (green) in 0.1 M [TBA][BF_4]/DMF at 233 K.

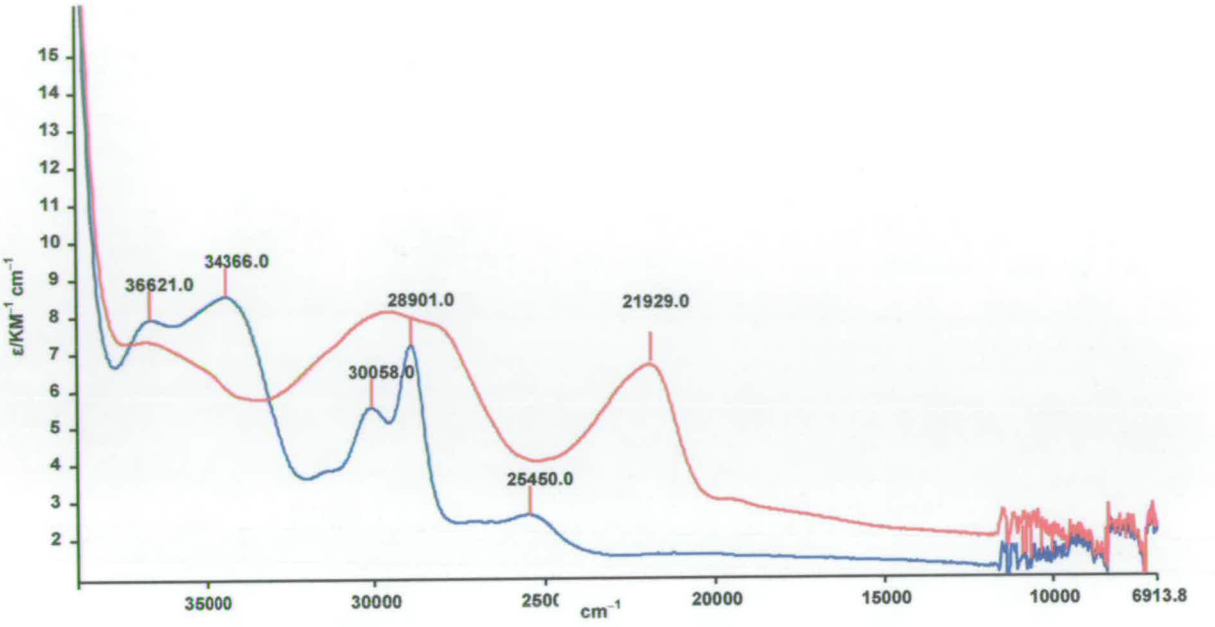

Figure 5.20 UV/Vis/nir spectra of $[Pt(5,5'–Br_2–bpy)Cl_2]^0$ (blue) and $[Pt(5,5'–Br_2–bpy)Cl_2]^{1-}$ (red) in 0.1 M [TBA][BF_4]/DMF at 233 K.

5.4.2.2. EPR of $[Pt(5,5'–Br_2–bpy)Cl_2]^{1-}$ and $[Pt(5,5'–Cl_2–bpy)Cl_2]^{1-}$.

Reduction of the $[Pt(5,5'–(X)_2–bpy)Cl_2]$ (X = Cl or Br) complexes to their mono–reduced state gave EPR active solutions. The solution EPR spectra of $[Pt(5,5'–Br_2–bpy)Cl_2]^{1-}$ and $[Pt(5,5'–Cl_2–bpy)Cl_2]^{1-}$ were similar, see Table 5.4 and Figure 5.21–5.22, showing coupling of the reduction electron to the ^{195}Pt nucleus, (natural abundance 34 %, I =½). The EPR signal was a broad central line with ^{195}Pt satellites, see Figure 5.21. $[Pt(5,5'–Br_2–bpy)Cl_2]$ has been chemically reduced to $[Pt(5,5'–Br_2–bpy)Cl_2]^{1-}$ using Na[BH_4] in DMF at 293 K. Any superhyperfine coupling

of the unpaired electron to ligand nuclei was unresolved. However, the contribution of the Pt nuclei to the SOMO was very small. This has been discussed in more detail in Chapter 4 of this thesis. The small contributions of the ^{195}Pt nuclei to the SOMO confirm that the redox active orbital is ligand based. The reduced species was therefore best formulated as $[Pt(II)(5,5'–Br_2–bpy)^{1-}Cl_2]^{1-}$.

Complex	^{195}Pt /G	ΔH_{pp} /G	g_{iso}
$[Pt(5,5'\text{-}Br_2\text{-}bpy)Cl_2]^{1-}$	57.0	9.50	1.98
$[Pt(5,5'\text{-}Cl_2\text{-}bpy)Cl_2]^{1-}$	63.0	26.00	1.99

Table 5.4 The coupling constant of the unpaired electron for $[Pt(5,5'\text{-}Br_2\text{-}bpy)Cl_2]^{1-}$ and $[Pt(5,5'\text{-}Cl_2\text{-}bpy)Cl_2]^{1-}$ generated in DMF at 293 K and 253 K respectively.

Frozen X–band EPR spectra could not be recorded for both of the complexes due to the insolubility of $[Pt(5,5'–Br_2–bpy)Cl_2]^{1-}$ and $[Pt(5,5'–Cl_2–bpy)Cl_2]^{1-}$. $[Pt(5,5'–(CO_2Et)_2–bpy)Cl_2]^{1-}$ and $[Pt(5,5'–(CO_2Me)_2–bpy)Cl_2]^{1-}$ were not studied any further as these have been studied previously by Jack.[38]

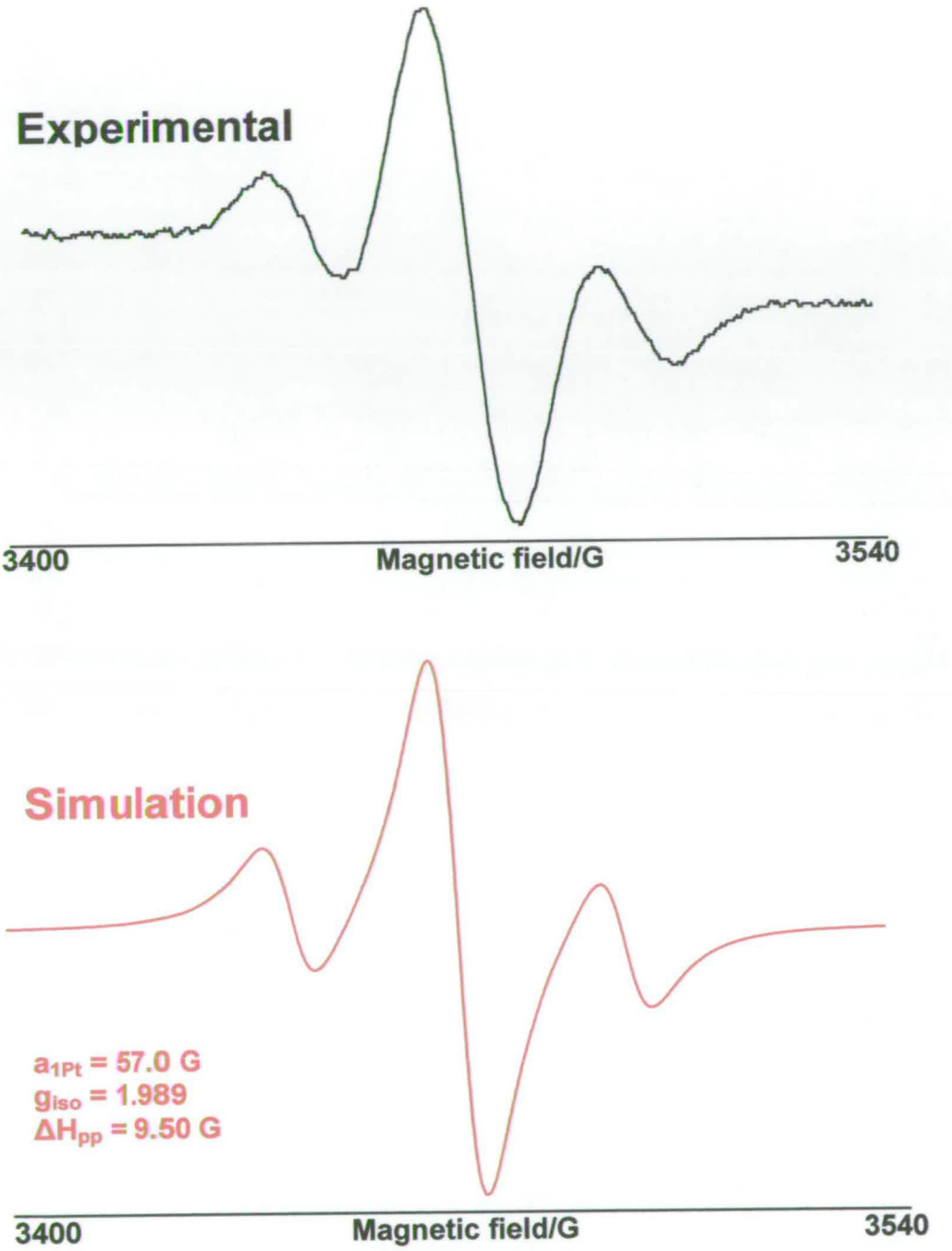

Figure 5.21 Experimental and simulated X-band EPR spectra of $[Pt(5,5'\text{-}Br_2\text{-}bpy)Cl_2]^1$- Chemically reduced (by $Na[BH_4]$ in DMF) at 293 K.

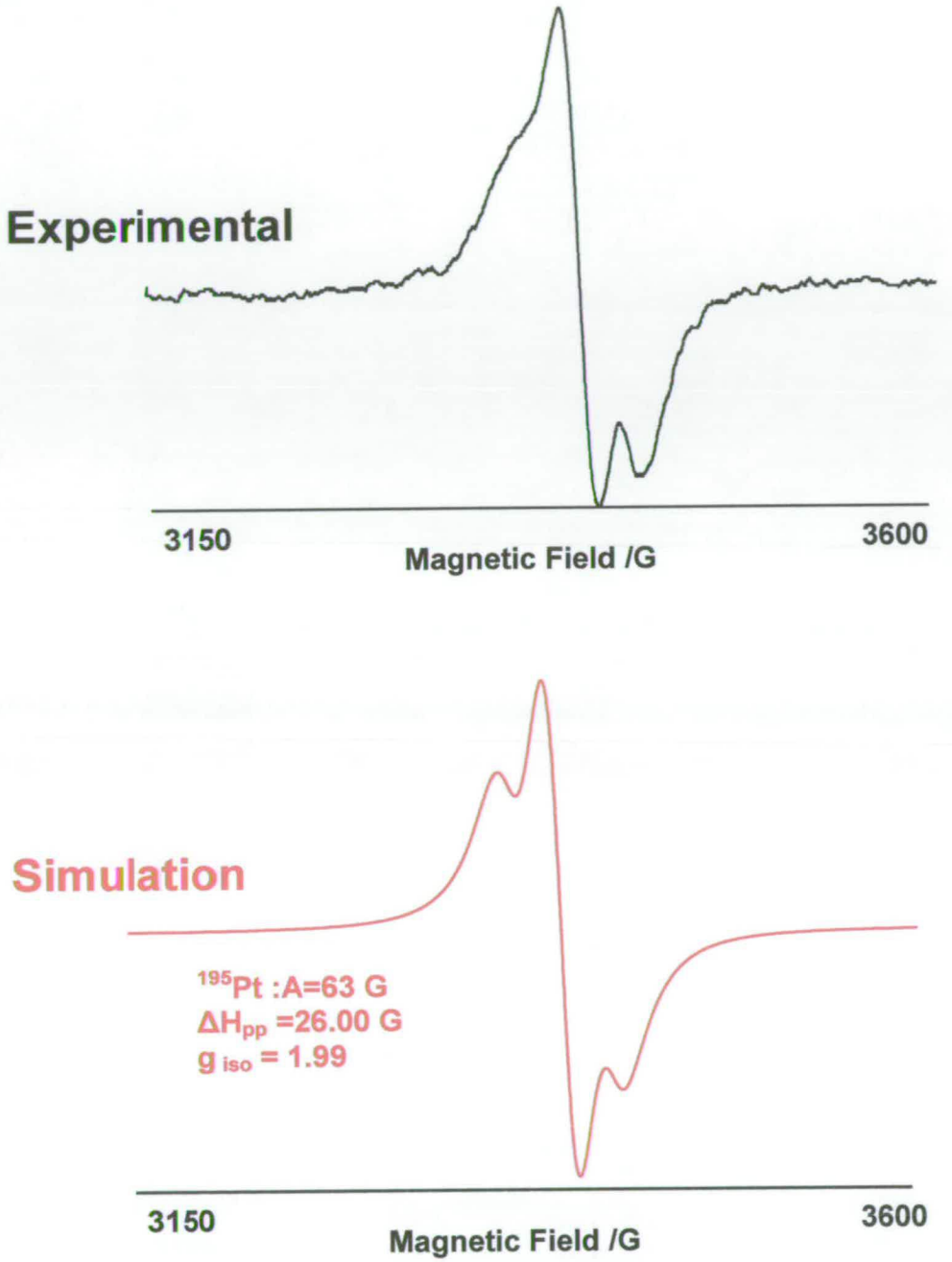

Figure 5.22 Experimental and simulated X–band EPR spectra of $[Pt(5,5'–Cl_2–bpy)Cl_2]^{1-}$ generated *in situ* in 0.1 M [TBA][BF_4]/DMF and E_{gen} = -1.65 V, vs. Ag/AgCl, at 253 K.

5.5. Conclusions.

The electronic structure of the reduced anions $[5,5'–(CO_2Et)_2–bpy]^{1-}$ and $[5,5'–(CO_2Me)_2–bpy]^{1-}$ showed no solvent effect. The structure on the $[5,5'–(CO_2R)_2–bpy]^{1-}$ and $[5,5'–(CO_2R)_2–bpy]^{2-}$ bands is presumed to arise from vibronic coupling. The free ligands and their Pt(II) complexes showed a localisation of the reduction electron on the bpy and thus the LUMO can be said to be ligand based. In addition, no solvent effect was observed for both the free ligands and their corresponding Pt(II) complexes.

The redox chemistry of $5,5'–Ph_2–bpy$ can be explained by the electron delocalised over the whole two py rings with a large contribution from the 2,2′ and 5,5′ carbon atoms.

The redox active orbital is ligand based for $[Pt(5,5'–Br_2–bpy)Cl_2]$ in line with related complexes such as $[Pt(5,5'–Cl_2–bpy)Cl_2]$. Spectroelectrochemical studies of $[Pt(5,5'–Cl_2–bpy)Cl_2]$ and $[Pt(5,5'–Br_2–bpy)Cl_2]$ indicated that the unpaired electron is ligand based, hence, the reduction product can be written as $[Pt(5,5'–(X)_2–bpy)^{1-}Cl_2]^{1-}$, where X is Br, Cl.

6. Conclusions and Future Work

6.1. Conclusions.

The pro-ligands 5,5′–Cl_2–bpy and 4–Cl–bpy in 0.1M [TBA][BF_4]/DMF revealed one irreversible reduction at −1.74 V and −1.84 V respectively. The reversibility of the one–electron reduction process of 6,6′–Cl_2–bpy at −1.63 V is readily influenced by temperature and scan rate. Spectroelectrochemical studies of 6,6′–Cl_2–bpy indicate that the reduction electron is delocalised over the two pyridine rings with a contribution from the chloro–substituent.

5,5′–X_2–bpy molecules (where X = CO_2Et, CO_2Me, Ph, Cl or Br) and their Pt(II) complexes [Pt(5,5′–X_2–bpy)Cl_2] showed a localisation of the reduction electron on the bpy and thus the LUMO of [Pt(5,5′–X_2–bpy)Cl_2] can be said to be ligand based. In addition, no solvent effect was observed for both 5,5′–$(CO_2Et)_2$–bpy and 5,5′–$(CO_2Me)_2$–bpy and their Pt(II) complexes. The EPR spectrum of $[5,5'–Ph_2–bpy]^{1-}$ indicates that the LUMO is based over the whole ligand.

Spectroelectrochemical studies of $[Pt(5,5'–Cl_2–bpy)Cl_2]^{1-}$ and $[Pt(5,5'–Br_2–bpy)Cl_2]^{1-}$ were in agreement with the assignment of the reduction electron being ligand based, hence, the reduction product can be written as $[Pt(5,5'–(X)_2–bpy^{1-})Cl_2]^{1-}$ (X is Br or Cl).

UV/Vis/nir and EPR spectroelectrochemistry studies on the 4,4′–dinitro–substituted molecules showed that the two py moieties of the molecule have little communication. Thus, the unpaired electron was localised on the substituted py moiety part of the ligand.

A linear correlation was found between the $E_{1/2}$ value of the nitro substituted 2,2′–bipyridine pro–ligands and the acceptor number of the solvent.

A triplet EPR signal was observed on the EPR spectrum of a frozen solution of the di–reduced species of 4,4′–$(NO_2)_2$–bpy.

UV/Vis/nir and EPR Spectroelectrochemical studies of [Pt(4–NO_2–4′–Cl–bpy)Cl_2] and [Pt(4,4′–$(NO_2)_2$–bpy)Cl_2] indicated that the reduction is ligand based.

Changing the nature and position of a substituent on the 2,2′–bipyridine system can have a dramatic effect on electronic structure and the acceptor number of solvents has to be considered.

6.2. Future work.

Further 5,5′–X_2–bpy pro–ligands where X = electron withdrawing group such as CF_3 or CN should be synthesised and studied. The triplet species $[4,4'–(NO_2)_2–bpy]^{2-}$ should be investigated further *e.g.* in different solvents. Other potential triplet systems such as $[6,6'–Cl_2–4,4'–(NO_2)_2–bpy]^{2-}$ and $[6,6'–(NO_2)_2–bpy]^{2-}$ should also be synthesised and studied in an attempt to fully understand their electronic character.

Other unsymmetrical substituted 2,2′–bpy pro–ligands should be synthesised and studied.

Further experiments should be undertaken in different solvents with different concentrations of electrolyte.

7. Appendix – Crystal Structure Data

Chemical formula	$C_{10}H_6Cl_2N_2$
T_{min}	0.74
M_r	225.08
T_{max}	0.69
Cell setting	
Space Group	Triclinic, P-1
Range of h,k,l	5→h→-5
a,b,c (A°)	3.818(3),6.017(6),10.387(10) 7→k→-8
α,β,γ (°)	103.50(8),91.57(7),91.23(7) 13 →l→-14
V(A^3)	231.8(4)
R_{int}	0.045
Z	1
Refinement on F^2	
D_X(Mgm^{-3})	1.612
No. of reflections	3786
No. of reflections for	727
H-atom treatment	Noref
No. of parameters	64
Cell parameters	
Weighting scheme	Sheldrick Weights
Temperature (K)	150
$\Delta\rho_{max}$, $\Delta\rho_{min}$ (e A^{-3})	0.74, -0.45
Crystal form, colour	Colourless plate
Crystal size (mm)	0.54 x 0.15 x 0.06
Diffractometer	Bruker Smart
Absorption correction	Semi-empirical
θ range (°)	3.48-30.09

Table 7.1 Crystal, Data collection and refinement data for X-ray structure of 5,5′-Cl_2-bpy.

Chemical formula	$C_{10}H_6Cl_2N_2$
T_{min}	0.61
M_r	225.08
T_{max}	0.94
Cell setting	
Space	Triclinic, P-1
Range of h,k,I	5→h→-5
a,b,c (A°)	3.779(3),5.665(5),10.891(10) 7→k→-7
α,β,γ	(°)84.35(6),82.48(7),87.29(7) 12 →I→-15
V(A^3)	229.89(4)
R_{int}	0.054
Z	1
Refinement on	F^2
D_X(Mgm^{-3})	1.626
No. of reflections	2209
For cell parameters	
H-atom treatment	Noref
θ range (°)	1.89-30.47
No. of parameters	64
Weighting scheme	Sheldrick Weights
Temperature (K)	150
$\Delta\rho_{max}$, $\Delta\rho_{min}$ (e A^{-3})	0.48, -0.46
Crystal form	Needle
colour	Colourless
Etinction method	SHELXL
Crystal size (mm)	1.40 x 0.17 x 0.09
Diffractometer	Burker Smart
Absorption correction	Semi-empirical

Table 7.2 Crystal, Data collection and refinement data for X-ray structure of 6,6′-Cl_2-bpy

8. References

1 E.Klingsberg in *Pyridine and its derivatives.*, Interscience Publishers, New York, 1960 Vol 14, pt 1.

2 G.R.Newkome, A.K.Patri,E.Holder and U.S.Schubert; *Eur.J.Org.Chem.* 2004, 235.

3 A.A.Schilit in *Analytical Applications of 1,10–Phenanthroline And Related Compounds*, Pergamon Press, London, 1969.

4 W. R. McWhinnie and J. D. Miller, *Adv.Inorg. Chem, Radiochem.*, 1969, **12** , 135.

5 M. C. Ventura, E. Kassab, G. Buntinx and O. Poizat, *J.Phys.Chem*; 2000, **2**, 4682.

6 K. Nakamoto, *J. Phys. Chem*, 1969, **64**, 1420.

7 E. Fielding and R. J. W. LeFevre, *J. Chem. Soc*, 1951, 1811; C. W.N. Cumper, R. F. A. Ginman, and A. I. Vogel, *ibid.*, 1962, 1186; P. H. Cureton, C. G. Le Fever, and R.J. W. LeFevere, *ibid.*, 1963, 1736.

8 C.Campa,J.Camps,J.Font and P.de March, *J.Org.Chem*, 1987, **4**, 52.

9 K.Szabo, S.K–Mate and N.Marek, *J.TheoChem*,1995, **333**, 275.

10 L.L.Merritt and E.D.Schroeder; *Acta Cryst.*, 1956 ,9(**10**), 801.

11 F. Vögtle in *Supramolecular Chemistry* , John Wiley and Sons, Chichester, 1993, 189.

12 E.C.Constable, *Adv.Inorg.Chem*, 1989, **1**, 34.

13 M.N.Golovin, M.M.Rahman, J.E.Belmonte and W.P.Giering, *Organometallics*, 1985, **4**, 1981.

14 B.E.Bursten and M.R.Green, *Prog. Inorg. Chem.*, 1988, **36**, 393.

15 Xiaoming Liu , Ph.D.Thesis , University of Edinburgh , 1988.

16 R.Tsuchida and Y.Shimura; *Bull.Chem. Soc. Japan*; 1956, **29**, 311.

17 Cotton and Wilkinson in *Advanced Inorganic Chemistry* 2nd edition, John Wiley and Sons, New York, 1966, Chapter 3.

18 H.Bette, *Ann.Phys.*, 1929, **3**, 135.

19 J. H. Van Vleck, *Phys.Rev.*, 1932, **41**, 208.

20 J. H .Van Vleck in *The Theory of Electric and Magnetic Susceptibilities*, Oxford. University Press, Oxford, 1932, Chapter 2.

21 J. H. Van Vleck, *J.Chem.Phys.*, 1935, **3**, 803.

22 J. H. Van Vleck, *J.Chem.Phys.*, 1935, **3**, 807.

23 L. E. Orgel in *An Introduction to Transition–Metal Chemistry: Ligand–Field Theory*, Methuen, London, 1960, 127.

24 C. J. Ballhausen in *Introduction to Ligand Field Theory*, McGraw–Hill, New York, 1962, 192.

25 J. March in *Advanced Organic Chemistry, 3rd Edition*, John Wiley and Sons, New York, 1985, chapter 7.

26 G. L.Geoffroy, H. Isci, J. Litrenti and W. R. Mason; *Inorg.Chem.*, 1977, 16,1950.

27 W. R. Mason and H. B. Gray, *J.Am.Chem.Soc*; 1960, **90**, 5721.

28 Y. Ohsawa, K. W. Hanck and M. K. Dearmond, *J.Electronal.Chem*,1984, **175**, 229.

29 G. T. Morgan and F. H. Burstall; *J.Chem.Soc.*, 1934, 965.

30 E. Bielli, P. M. Gidney, R. D. Gillard and B. T. Heaton; *J.Chem.Soc, Dalton*, 1974, 2133.

31 E. J. L. McInnes; P.h.D Thesis, University of Edinburgh, 1995.

32 D. Collison, F.E. Mabbs, E.J.L.McInnes, K.J.Taylor, A.J.Welch and L.J.Yellowlees; *J.Chem.Soc., Dalton Trans.*, 1996, 329.

33 L. Kumar, K. H. Puthraya and T. S. Srivastava, *Inorg.Chem. Acta*, 1984, **86**, 173.

34 A.H.Maki, N.Edelstein, A.Davidson and R.H.Holm, *J.Am.Chem.Soc.*, 1964, **86**, 4580.

35 P.H. Rieger, J.Magon. Reson., 1997, **124** , 140.

36 E.J.L McInnes, R.D. Farley, C.C. Rowlands, A.J.Welch, L.Rovatti and L.J.Yellowlees., *J.Chem.Soc., Dalton Trans.*, 1999, **23**, 4203.

37 E.J.L McInnes, R.D. Farley, S.A. Macgregor, K.J. Taylor, L.J.Yellowlees and C.C.Rowlands; *J.Chem.Soc., Faraday Trans.*, 1998, **94**, 2985.

38 Lorna Jack , P.h.D Thesis, University of Edinburgh , 2003.

39 P.N.W. Baxter and J.A. Conner, *J.Org. Chem.*, 1988, **355**, 193.

40 C.Hansch, A.Leo and R.W. Taft, *Chem.Rev.*, 1991, **91**, 165.

41 A.C. Fisher in *Electrode Dynamics*, Oxford University Press, Oxford 1996.

42 W. M. Schwarz and I.J. Shain, *J. Phys.Chem.*,1965, **69**, 30.

43 F.E. Mabbs,*Chem.Soc.Rev*, 1993, 313.

44 E. Geary, Ph.D. Thesis, University of Edinburgh, 2005.

45 J. I. Bruce, J.C. Chambron, P. Kolle and J.P. Sauvage, *J.Chem. Soc., Perkin Trans.* 2002, **1**, 1226.

46 W. Frank, M. Wasgindt, T. Pautzsch and E. Klemm, *J. Macromolecular. Chem & Phys*, 2001, **7**, 980.

47 L. C. Craig, *J. Am. Chem. Soc.*, 1934, **56**, 231.

48 J. Hassan, V. Penalva, L. Lavenot , C. Gozzi and M. Lemaire, *Tetrahedron*, 1998, **54**, 13793.

49 J. Canales, J. Ramirez, G. Estiu and J. Costamagan, *Polyhedron*, 2000, **19**, 2373.

50 D. Wenkert and R. B. Woodward., *J. Org. Chem.* 1983, **48**, 283.

51 M. Hamana, *J. Pharm. Soc. Japan*, 1955, **75**, 123.

52 E. C. Constable and K. R. Seddon, *Tetrahedron*, 1983, **39**, 291.

53 M. J. Cook, A. P. Lewis and A. J. Thomson, *J. Chem. Soc. Perkin Trans*, 1984. **2**, 1293.

54 G. Maerker and F.H. Case; *J. Am. Chem. Soc.*, 1958, **80**, 2745.

55 SAnderson, E.C. Constable, K.R. Seddon, J.E. Turp, J.E. Baggot and M.J. Pilling; *J. Chem. Soc., Dalton Trans.*, 1985, **11**, 2247.

56 M. A. Weiner and A. Basu , *Inorg. Chem.*,1980, **19**, 2797.

57 M. Pilkington, S.J. Hauser, C. Hoffman and H.B Burgi, *Acta Cryst.*, 1997, C**53**, 1719.

58 A. Basu, M. Weiner; T.C. Strekas and H.D. Gafney; *Inorg. Chem.*, 1982, **21**, 1085.

59 A. Basu, H.D. Gafney and T.C. Strekas; *Inorg. Chem.*, 1982, **21**, 2231.

60 N. Sutin, M. J. Weaver and E. L. Yee, *Inorg. Chem.* 1980, **19**, 1096.

61 S. Sahami and M. J. Weaver, *J. Electroanal. Chem. Interfacial Electrochem.*, 1981, **122**, 155.

62 G. Maerkner and F.H. Case, *J.Am.Chem.Soc* , 1958, **80**, 2745.

63 S. Shahami and M. J. Weaver, *J. Solution Chem.*, 1981, **10**, 199.

64 M. J. Weaver, *J. Phys. Chem.*, 1979, **83**, 1748.

65 M. J. Weaver, *J. Phys. Chem.*, 1980, **84**, 568.

66 M. J. Weaver and E. L. Yee, *Inorg. Chem.* 1980, **19**, 1936.

67 K. M. Kadish, K. D. Schaeper, C. L. Merill, B. R. Welch and L. J. Wilson, *Inorg. Chem.*, 1980, **19**, 2816.

68 K. M. Kadish and D. Schaeper, *J. Chem. Soc. Chem Comm.*, 1980, **24**, 1273.

69 M. P. Youngblood and D. W. Margerum, *Inorg. Chem.*, 1980, **19**, 3036.

70 J. M. Anast, A. Hamburg and D. W. Margerum, *Inorg. Chem.*, 1983, **22**, 2139.

71 V. T. Taniguchi, N. Salisuta–Scott, F. C. Anson and H. B. Gray, *Pure Appl. Chem.*, 1980, **52**, 2275.

72 N. Sailasuta, F. C. Anson and H. B. Gray, *J. Am. Chem. Soc.* 1979, **101**, 455.

73 T. Taniguchi, B. G. Malmstrom, F. C. Anson and H. B. Gray, *Proc. Natl. Acad. Sci. U.S.A.*, 1982, **79**, 3387.

74 L. S. Reid, V. T. Taniguchi H. B. Gray and A. G. Mauk, *J. Am. Chem. Soc.* 1982, **104**, 7516 .

75 W. Bottcher, G. M. Brown and N. Sutin, *Inorg. Chem.*, 1979, **18**, 1447.

76 E. F. Waurrousek and J. V. McArdle, *J. Inorg. Biochem.*, 1982, **17**, 169.

77 H. Ogino and K. Ogino, *Inorg. Chem.*, 1983, **22**, 2208.

78 J. T. Hupp, P. A. Lay, H. Y. Lui, W. H. F. Petri, A. M. Sargeson and M. J. Weaver, *J. Electroanal. Chem. Interfacial Electrochem.*, 1984, **163**, 371.

79 J. T. Hupp and M. J. Weaver, *J. Electrochem. Soc.* 1984, **131**(3), 619.

80 J. T. Hupp and M. J. Weaver, *Inorg. Chem.*, 1984, **23**, 256.

81 J. T. Hupp and M. J. Weaver, *J. Phys. Chem.*, 1984, **88**, 1860.

82 J. S. Jaworski, *J. Electoanal. Chem*, 1987, **219**, 209.

83 M. Borsari, M. Cannio, D. Dallari, C. Fontanesi, G. Gavioli, S. Peressini and C. Tavagnacco, *Aust. J. Chem.*, 2003, **56**, 1233.

84 T.J. Kinnunen, M. Haukka, M. Nousiainen, A. Patrikka and T.A. Pakanen; *J. Chem. Soc., Dalton Trans.*, 2001, **18**, 2649.

85 E. König and S. Kremer; *Chem. Phys. Lett.*, 1970, **5**, 87.

86 F.H. Burstall, *J.Chem. Soc.*, 1938, 1662; R.F. Knott and J. G. Breckenridge, *Canadian J. Chem.*, 1954, **32.** 512; E. Cizlak, U.S.P. 2,992,224 (Chem. Abs., 1962, **56** , 461) ; V. B. Leontev, O. S. Ostroshchenko, Y. S. Mangutrova, and A. S. Sadykov, *J.Gen. Chem.(U.S.S.R)*, 1965, **35**, 298.

87 P. R. Murray, PhD thesis, The University of Edinburgh, 2005.

88 K. J. Taylor, PhD thesis, The University of Edinburgh , 1990.

89 F. Pichot, J.H. Beck and C. M. Elliott; *J. Phys. Chem.* A, 1999, **103**, 6263.

90 P. Rotzinger, S. Munavalli, P. Comte, J.K. Hurst, M. Gratzel, F–J. Pern and A.J. Frank; *J. Am. Chem. Soc.*, 1987, **109**, 6619.

91 H.F.M. Nelissen, A.F.J. Schut, F. Venema, M.C. Feiters and R.J.M. Nolte; *J.Chem. Soc., Chem. Commun.*, 2000, **7**, 577.

92 P.D. Beer, O. Kocian, R.J. Mortimer and C. Ridgway; *J. Chem. Soc. Dalton Trans.*, 1993,**17**, 2629.

93 V.W–W. Yam and A.S–F. Kai; *Inorg. Chim. Acta.*, 2000, **300-302**, 82.

94 T.J. Meyer: *Acc. Chem. Res.*, 1978, **11**, 94.

95 D.G. Whitten; *Acc. Chem. Res.*, 1980, **13**, 83.

96 C.P. Whittle; *J. Heterocyclic Chem.*, 1977, **14**, 191.

97 K. Kurita and R.L. Williams; *J.Polym. Sci., Polm. Chem. Ed.*, 1973, **11**, 3125.

98 V.T. Coombe, G.A. Heath, A.J. Mackenzie and L.J. Yellowlees; *J. Chem. Soc., Chem. Commun.*, 1984, **23**, 3423.

99 E. Bielli, P. M. Gidney, R. D. Gillard, B. T. Heaton, *J. Chem. Soc., Dalton Trans.*, 1974, **20**,2133

100 V. Gutmann in *The Donor–Acceptor Approach to molecular interaction.*, Plenum Press, New York, 1978, 79.

101 W. M. Fox, J. M. Gross and M. C. R. Symons *J. Chem. Soc.(A),* 1966, 448.

9. Courses and Conferences Attended

Inorganic Seminar and Colloquia.

3rd Workshop on the theory and practice of EPR Spectroscopy, University of Manchester 2004.

Launch of ScotCHEM, September 2005.

USIC, University of Clasgow, 2005.